INVESTIGATION OF THE NEAR SURFACE MECHANICAL PROPERTIES OF Au-Ti THIN FILMS

By

GOLNAZ BASSIRI JAHROMI

Bachelor of Science in Mechanical Engineering
Oklahoma State University
Tulsa, OK
2005

Submitted to the Faculty of the
Graduate College of the
Oklahoma State University
in partial fulfillment of
the requirements for
the Degree of
MASTER OF SCIENCE
July, 2008

INVESTIGATION OF THE NEAR SURFACE MECHANICAL PROPERTIES OF Au-Ti THIN FILMS

Thesis Approved:

Don A. Lucca

Thesis Adviser

C. Eric Price

Ranga Komanduri

A. Gordon Emslie

Dean of the Graduate College

ACKNOWLEDGMENTS

IN THE NAME OF GOD, THE COMPASSIONATE, THE MERCIFUL

I would like to thank my adviser Dr. D. Lucca for his guidance and support to whom I owe my academic growth. I also would like to thank my committee members, Dr. E. Price, who constantly supported and encouraged me and provided intellectual guidance which helped me to improve the present work, and Dr. R. Komanduri for his inputs and comments.

I would greatly thank our collaborators at Massachusetts Institute of Technology and Los Alamos National Lab. I am grateful of Dr. M. Nastasi's contributions whom this work would not be done without. Special thanks to Mr. K. Baldwin and Dr. I. Usov at Los Alamos National Lab for all their help. Extended thanks to Dr. A. Slocum at MIT and his students, especially Dr. A. Weber for providing the pure Au films. I appreciate Dr. D. Grischkowsky for his permission to utilize the Four Point Probe. Many thanks to Dr. A. Apblett for his contributions in XRD measurements. I would like to thank members of Ultra Precision Surfaces Group: Dr. M. Klopfstein, Dr. R. Ghisleni, Mr. V. Doan, Mr. B. Dvorak, Mr. T. Harriman, and Mr. J. Potts for all their help. I would also like to thank Dr. K. Sallam for his encouragement for pursuing graduate school.

Many appreciations to all my family and friends, far and near, for their encouragement and support. I would like to give my most gratitude to my mother and father, Rana and Mohammad and my brother Sohrab for their neverending encouragement, inspiration, support and love throughout my whole life. Last but far from least, my sincere indefinite thank you's to my best friend Michael who cheered my life with his patience, motivation and affection.

This material is based upon work supported by the National Science Foundation under Grant No. 0521989. Any opinions, findings, and conclusions or recommendations expressed in this material are those of the author and do not necessarily reflect the views of the National Science Foundation.

This work was performed, in part, at the Center for Integrated Nanotechnologies, a U.S. Department of Energy, Office of Basic Energy Sciences user facility at Los Alamos National Laboratory (Contract DE-AC52-06NA25396) and Sandia National Laboratories (Contract DE-AC04-94AL85000).

TABLE OF CONTENTS

LIST OF TABLES

LIST OF FIGURES

NOMENCLATURE

A ..... Projected Area

A_a ..... Apparent Contact Area

AFM ..... Atomic Force Microscopy

at. ..... Atomic (percentage)

BCC ..... Body Center Cubic

BCT ..... Body Centered Tetragonal

d ..... Spacing

E ..... Elastic Modulus

E-Beam ..... Electron Beam

EDS or EDX ..... Energy Dispersive Spectroscopy by X-Ray

EM ..... Electro Mechanical

E_r ..... Reduced Elastic Modulus

f ..... Volume Fraction

FCC ..... Face Center Cubic

FPP ..... Four Point Probe

G ..... Bulk Modulus

GP ..... Guiner and Preston (zone)

H ..... Hardness

H_V ..... Vicker's Hardness

H_N ..... Nanoindentation Hardness

h_c ..... Contact Depth

HCP ..... Hexagonal Close Packed

HRTEM ..... High Resolution Transmission Electron Microscopy

I ..... Current

IC ..... Integrated Circuits

IFM ..... Interfacial Force Microscope

k ..... Geometry Correction factor

LANL ..... Los Alamos National Lab

MEMS ..... Micro Electro Mechanical Systems

MIT ..... Massachusetts Institute of Technology

Mo ..... Molybdenum

OSU ..... Oklahoma State University

PIXE ..... Particle Induced X-Ray Emission

P ..... Load

R_a ..... Mean Roughness

RBS ..... Rutherford Backscattering Spectrometry

RF ..... Radio Frequency

RMS ..... Root Mean Square (Roughness)

ROM ..... Rule of Mixture

SAM ..... Self Assembled Monolayers

S ..... Stiffness

s ..... Seconds (time)

SEM ..... Scanning Electron Microscopy

SPM ..... Scanning Probe Microscopy

STM ..... Scanning Tunneling Microscopy

t ..... Thickness

TEM ..... Transmission Electron Microscopy

XPS ..... X-Ray Photoelectron Spectroscopy

XRD ..... X-Ray Diffraction

V ..... Voltage

Z ..... Atomic Number

Z_i ..... Current Z Value

$\Delta\sigma$ ..... Change in Yield Stress

ϵ ..... Strain Field

ρ ..... Resistivity

ρ_s ..... Sheet Resistance

ν ..... Poisson's Ratio

λ ..... Wavelength

Chapter 1

Introduction

Micro electro mechanical systems (MEMS) are micro-sized integrated devices with mechanical and electrical components such as actuators, interconnects, relays, and contacts. MEMS are employed widely as intelligent integrated circuits (IC) in various applications by virtue of their unique characteristics in high frequency components, radio frequency (RF) switches, actuators, optical detectors and others [1].

Although micro-sized systems have many advantages, the small size results in a large surface area to volume ratio, which increases the effect of the surface forces on the performance of the systems [2]. Some of the surface forces negatively effect the applications of MEMS and generate a failure in performance by surface welding, stiction, change in contact resistance, wear, delamination, etc. [2, 3].

To ensure the continued integrity of the desired properties of for example, separable electrical contacts, thin films are commonly used to increase reliability with respect to current conduction, low friction, and wear resistance [4]. Since they involve movable parts, control and determination of the mechanical properties are also important factors for long term stability, performance, and reliability of the thin films [5].

Motivated by the goal to develop high power MEMS electrical contacts, Au thin films were studied, in terms of their mechanical and electrical properties in parallel with the development of a MEMS-based contact tester device, to ensure applicable performance. The primary focus of the present work is the investigation of the mechanical and electrical properties of modified Au thin films for potential use in high power MEMS electrical contacts capable of operating at a current up to 1 A.

1.1 Objective

The fundamental aim in the present study was to investigate the basic mechanical properties of Au and modified Au thin films. The experimental approach undertaken was designed to understand how the surface and subsurface structure affects the material's properties. The systematic study was aimed at investigating the mechanical properties of the modified Au films by homogeneous and coherent formation of thin near surface alloy by co-evaporation with small Ti content.

1.2 Contributions

The present work is part of a collaboration between Massachusetts Institute of Technology (MIT), Los Alamos National Laboratory (LANL), and Oklahoma State University (OSU). In the baseline studies of polycrystalline Au films, fabrication of the films as well as design and fabrication of the MEMS contact tester were performed at MIT. Synthesis of the modified Au films were performed at LANL and characterization of mechanical and electrical properties of the thin films were performed at OSU.

Investigation of the mechanical, electrical, and tribological properties of the thin films is the contribution of the present work. Nanoindentation was used for determination of the hardness and elastic modulus. It was also utilized as the controlled force instrument for tribological measurements of the microscratching and wear experiments. Resistivity was obtained by Four Point Probe measurements. Atomic force microscopy (AFM) provided surface topography of the film and was used for the surface roughness measurements. Heat treatment of the modified Au-Ti films was also conducted at OSU to investigate the change in mechanical properties. The Raman scattering studies to further characterize the heat treated Au-Ti films were performed by a member of the Ultra Precision Surfaces Group. Particle Induced X-ray Emission (PIXE) measurements were performed at LANL to determine the chemical composition of the films. Characterization of the films using X-ray Diffraction (XRD) was performed at the OSU Chemistry Department to determine the materials' crystal structural and the grain size.

Chapter 2

Background

The interrelationship between resistivity and hardness, two important properties for MEMS contact relays, is a guideline in the design and assessment of contact resistance, adhesion, wear, and the deformation of surfaces. Therefore, understanding the mechanical as well as electrical properties is essential for the design and fabrication of MEMS contacts. Furthermore, not only do surface topography and roughness have significant roles on the performance of the contacts, the elasticity of the films over a large range of temperature, from ambient to high (up to about 500°C), is also critical.

This chapter introduces the primary use of Au thin films, the emerging problems of Au films, and presents a review on the characterization of modified films to improve the Au properties. Inasmuch as mechanical and electrical performance in the contacts have significant influence on the selection of materials, a brief summary on the techniques used for characterization of the mechanical properties, surface topography, and resistivity are also provided.

2.1 Au Thin Films

MEMS devices are typically fabricated by Si which may be coated on some surfaces by Au due to its unique characteristics. Although, Ag and Cu are the highest conductors, both oxidize at room temperature which increases the resistivity of the films. Distinct attributes of Au, such as high conductivity, ductility, and inertness, low resistivity, contact resistance, and susceptibility to oxidation favor Au against other metals [2]. On the other hand, due to the low hardness of Au, it is prone to adhesion failure in cycling conditions which reduces reliability [6]. Tribological problems, such as fretting wear usually occur in the interaction of contacts during repetitive cycling. Minimizing

adhesion consumes less force to initiate and break the contacts which not only reduces the power cost but also provides faster and lighter contacts [3]. However, larger forces are often required in contacts to break through contamination to provide low resistance.

Au thin films are generally harder than bulk pure Au (bulk Au hardness is about 0.6 GPa, versus that for a thin film of 1 - 2 GPa [7]). The change in properties of bulk compared to thin films could be affected by: different microstructures, the substrate effect [8], the nanoindentation size effect, strain gradient plasticity phenomena [9–12], dislocation strengthening [10, 13], and others. Thin films are commonly stronger than bulk materials due to finer grain size, higher cooling rates ($\approx 10^{10}$°C/s [14]), and built-in structural defects during deposition [10, 15]. The grain boundaries hinder dislocation movements and subsequently, the dislocations pile-up at the grain boundaries which increases the yield stress. The increase in yield stress of thin films, which is inversely proportional to the square root of the grain size, is known as the Hall-Petch effect [16].

Several investigations confirmed material property changes in Au thin films by varying the deposition technique and temperature, thickness of the deposited film and underlayer films [17, 18]. For example, electron beam (e-beam) evaporated films offered the lowest surface roughness compared to sputtered or electroplated films [17].

Modification of Au to increase the tribological performance while minimizing the contact resistance was investigated in recent years to maximize the efficiency of the MEMS electrical contacts. A few of these modifications were by surface alloying of Au [19–21], self-assembled monolayers (SAM) [3], composite nanomaterials [22, 23], dispersion of nanoparticles [24] and deposition of a thin near surface layer film as a coating [25].

2.1.1 Modification by Mo

Mo has been used due to its noted tribological performance as a, friction-reducing agent and anti-scuffing protector [26], film co-deposited with Ag [22] and Al [23], thin film coating [27], and a microlaminated film (multiple alternating layers of Mo on top of Al_2O_3) with Al_2O_3 [28]. An increase in tribological performance has been reported in the majority of the aforementioned studies.

Although no literature was found on tribological performance resulting from the interaction between Au and Mo, several studies have shown evidence of the interface interaction of the two immiscible metals [19–21]. Biener et. al. [19] investigated alloying of these two metals by electron beam evaporation of Mo up to 1 or 2 atomic layers thick (2.5 or 5 Å). Modifying a Au(111) herring-bone reconstruction (chevron like) by Mo, was a subject of several related studies [19–21]. Unlike

the chemical inertness of Au to Mo, it has been proposed that the elbow sites (in Au) are the most reactive sites for the exchange of atoms, if the exchange is with a metal of higher surface free energy (Mo) [19, 21]. In deposition of Mo at 450 K, the Mo clusters changed the herringbone pattern to a triangular pattern. Biener et. al. reported that the change in pattern represents the dissolution of Mo in Au, unlike the appearance of holes in the Au step.

Electron beam evaporated Mo thin films (0.4 - 1.5 μm) revealed a higher hardness versus steered arc deposited Mo films despite the columnar grain formation in both methods of deposition [27]. Hardness and elastic modulus of polycrystalline Mo thin films were found to be between 6 - 12 GPa and 250 - 325 GPa, respectively [27, 28]. The average grain size in Mo thin films has been reported to be between 20 - 40 nm [27, 28].

One approach to obtain superior mechanical properties is to co-deposit a metal with other alloying elements. Co-evaporation of Mo with Al was investigated to increase the strength and stability of Al [23]. A unique composition of crystalline Al-32 at. % Mo provided an exceptional increase in hardness versus pure Al and in resistivity versus pure crystalline Mo or Al. Nanocomposite formation of Al-Mo showed the increase in the hardness by forming a unique microstructure of dispersed Mo nanocrystals in an amorphous Al-rich matrix. Co-deposition of immiscible Mo and Ag was also explored to investigate enhanced tribological properties by reducing wear deformation and friction in the nanocrystalline Ag-Mo thin film coatings [22].

2.1.2 Modification by Alloy Hardening

Alloying has been proven to be a successful technique to improve the mechanical properties of pure metals. Accordingly, the modification of Au thin films by alloying of the thin near surface layer was considered and investigated in the present study. Surface alloying could introduce different surface tribology, hardening, bonding, and corrosion by modifying the characteristics of the surface elements.

Inasmuch as some alloys do not completely dissolve into the other, similar to Ni and Cu isomorphous alloys, the majority of metals have solubility limits which vary with temperature. The secondary element diffuses as a substitutional solid solution in a dominant matrix element.

Development of the solid solution in alloying elements forms by maintaining the full solubility of the two metals from a liquid phase to a solid state without any changes in the structure of atoms. The complete solubility of the two metals is developed by arrangement of one metal crystal lattice into the other. This could be obtained from a “substitutional” or an “interstitial” solid

solution. An interstitial solid solution often occurs when the atoms of the solute (the element with the smaller amount in the solution) are small enough to be placed within the spaces in the solvent (the element with the greater amount in the solution) lattices. In substitutional solid solution, the solvent's atoms are replaced by the solute's atoms within the crystal lattice. Several factors, such as atomic size, crystal structure, electronegativity and valency, determine the solution status of atoms in terms of "ordered" or "disordered". In a disordered substitutional solid solution of two metals far from each other in the periodic table with considerable differences in atomic size and a divergent electronegativity, an intermetallic compound could form. An intermetallic compound's crystal structure and properties often differ remarkably from the intermediate solid solutions [29,30].

Solid solution hardening is a strengthening mechanism in which a pure metal hardens by alloying with a substitutional or interstitial solid solution. Impurities in the solute atoms, which favorably segregate around dislocations, could alter the lattice strain of the solvent, impose the interaction between the impurities and dislocations, and finally restrict the movement of the dislocations. The outcome of this interaction is an increase in hardness and strength [30].

An alternative hardening procedure is precipitation hardening which is achieved by phase transformation from uniform dispersion of extremely small particles of a second phase to the original matrix phase upon heat treatment. Precipitate hardening or age hardening enhances the hardness or strength with time. Heat treating during the hardening of the precipitate is an important parameter which is carried out in two steps. The first is "solution heat treatment", which involves heating until the atoms are dissolved to form a single phase solid solution followed by quenching. The second step, "precipitation heat treatment", involves heat treating the super saturated solid solution to an intermediate temperature for an appropriate period of time (aging) to diffuse and form uniformly dispersed particles of a composite [30].

Coherency between the lattice of the matrix and precipitates in the precipitate hardening system differentiates it from the dispersion hardening system. Guinier [31] and Preston [32] detected a local clustering of an alloy after quenching from the solid solution state. The clustered region (GP zone) may produce a strain which could increase the hardness of the GP alloy compared to the solid solution [16]. By increasing the aging time, the hardness increases further by ordering of the larger clusters and additional strain in the matrix. With continued aging, an equilibrium phase forms, which is no longer coherent causing the hardness to decline [16]. In an alloy aged beyond peak hardness, the significant increase in strain hardening rate suggests the dislocations move around particles and bypass them. Orowan proposed the hardening mechanism between two overaged non-coherent precipitates, separated by a distance λ, by leaving a dislocation loop around

particles (Figure 2.1). He also demonstrated that the required force for dislocations to bypass the two precipitates is inversely related to λ [33].

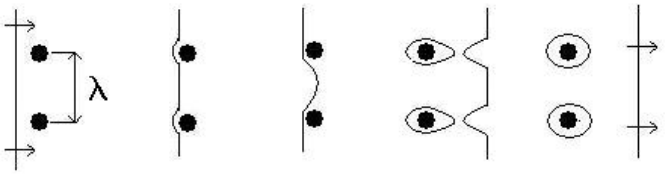

Figure 2.1: Orowan's Hardening Mechanism

Alloy Hardening of Au and Ti

Ti alloys have been used extensively as wear resistant materials which inspired its selection as the second element to improve the properties of the Au films used in the present study. Chemical vapor deposited TiC and TiN coatings were reported to have hardnesses of about 31 GPa and 26 GPa, respectively, with high abrasive wear resistance and lubricity properties [34]. A study by Wirz et. al. [35] showed that crystallized co-evaporated Cr-Ti films (heat treated at 800°C for an hour) possessed a comparable or superior tribological performance to that reported for TiN coatings. However, dependence of Cr concentration was not observed in the tribological performance of the Cr-Ti films. In another study, a tribological investigation of Ti, TiO and TiN thin films (200 nm) showed an equal coefficient of friction (0.2 - 0.4) for all the films. However, unlike the Ti films, the wear rates in TiN and TiO films were found to strongly depend on the chamber's air pressure in which the experiments were performed [36].

In spite of the extensive use of Ti as an adhesion layer, prior investigations on the effect of Ti for the wear resistance properties of Au thin films were not found in the literature. However, in a recent investigation, Ti was found to enhance the strength (by about 118 %) and hardness (by about 318 %) in Au990 jewelry alloys [37]. Previous studies in the dental field also showed an increase in the mechanical properties of Au by addition of up to 10 at. % Ti [38]. While the investigation was intended to develop an optimum dental alloy of cast Au-Ti, it showed the hardening effect of the Au_4Ti intermetallic compound in Au-Ti solid solution. The Au-Ti alloys have been a strong candidate in biomedicine, specifically in dentistry, due to the passivation compatibility of the Ti-oxide layer, and high corrosion resistance of Au and Ti [38].

The Au-Ti as a choice for metal alloys as an electric contact coating in MEMS switches was excluded in one study due to the formation of intermetallic compounds and the physical transformation

(e.g., Au-51 at. % Ti) with increasing temperature (above 590°C) [39]. Nevertheless, determination of the appropriate composition of this alloy and the evolution of the intermetallic compound could increase the mechanical properties of pure Au and deliver the desired properties.

The shape memory effect of binary Au-Ti alloys reported by Wu et. al. [40] could also benefit the coupling contact performance of Au-Ti films. The thermoelastic martensitic transformation of Au-Ti at high temperature (about 900 K) strongly suggested the Au-Ti alloy for use as a shape memory alloy [41].

The Au-Ti alloys have been extensively studied including: phase diagrams [42–44], thermodynamics [45], crystal structure [46,47], microstructure [42], magnetic properties [48], ohmic properties [49], corrosion behavior [50], interdiffusion of Au and Ti [51–54] and martensitic transformation [40, 44]. According to the Au-Ti binary system (Figure 2.2), the Au rich solid solution at about 500°C has a solubility of about 1 at. % Ti and below that temperature the intermetallic Au_4Ti hardens the solid solution phase. The evolution of the Au_4Ti intermetallic compound at about 20 at. % Ti (between 18 - 20 at. %) was reported by Pietrokowsky in 1962 by characterizing the lattice parameters of alloys between 0 - 35 at. % Ti [42]. The crystal structure of Au_4Ti, similar to Ni_4Mo, is body centered tetragonal (BCT). The crystal structure of pure Au is face center cubic (FCC) and Ti exhibits two forms of crystal lattices as temperature varies. An α-Ti structure is hexagonal close packed (HCP) at room temperature and a β-Ti structure is body centered cubic (BCC) at temperatures above 883°C [45, 55].

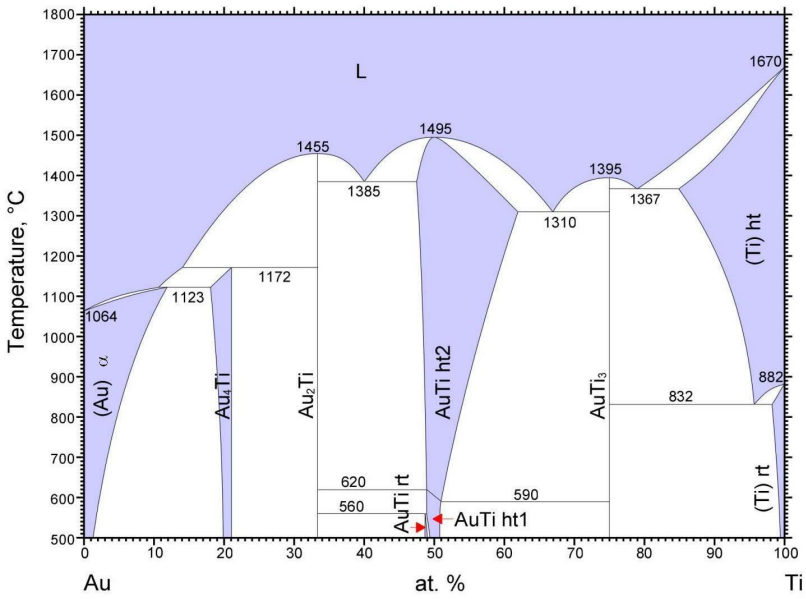

Figure 2.2: Au-Ti binary phase diagram [56]

While prior investigations on the the mechanical properties, as well as electrical properties, of the near surface of co-evaporated Au and Ti films were not found in the literature, Poate et. al. [51] investigated the interdiffusion of sequentially e-beam evaporated Au-Ti bilayer thin films. In their investigation, heat treating of the bilayer Au-Ti films in air was reported to enhance the interdiffusion of Au and Ti compared to heat treating in a vacuum.

Solid solution strengthening of Au-3 at. % Ti (0.96 wt. %) was investigated by Yang et. al. [37]. The atomic weight ratio between Au and Ti and relative difference in the atomic radius between Au and Ti are two parameters affecting the solid solution strengthening. The multiplication of the two factors determines the solid solution strengthening effect which weakens as the product decreases. Yang et. al. noted the weak effect of solid solution strengthening in Au-Ti alloys, nevertheless, he reported that grain refinement of Ti strongly affected the strengthening of Au [37].

Graham showed the increase in yield stress of Au by the addition of 4 at. % Ti and demonstrated precipitate hardening behavior of Au-Ti [57]. Later, Kim et. al. and Yang et. al. validated age hardening by solution treatment of Au-Ti at 950°C for 15 min followed by quenching in an ice brine and isothermally aging at 450 - 550°C for various times [37, 58]. As the heat treatment period increased, the hardness was enhanced, approached a maximum, and then declined. The increase in temperature to 550°C shortened the time period to reach the maximum hardness [37, 58, 59].

Van Heerdan et. al. observed a transformation in microstructure of Ti-Au alloys by varying the heat treatment [60]. The homogeneous and coherent formation of Au-7.5 at. % and 13 at. % Ti alloys were produced by rapid solidification. After 1 hr and 24 hrs holding periods at 500°C, Transmission Electron Microscopy (TEM) results of the Au-7.5 at. % Ti showed a fine, coherent precipitate distribution of Au_4Ti. However, breakdown in coherency and coarsening in Au-13 at. % Ti was seen after 24 hrs at 500°C [60].

An increase in hardness due to strain hardening or work hardening of Au-Ti alloys was also reported previously in the literature [37, 59]. A high strain hardening rate of Au-Ti alloys was reported due to the hindering of dislocations in the fine slip bands [57]. Graham reported that accumulation of tangled dislocations from interaction with precipitates resulted in fine slip bands. To plastically deform an Au-Ti alloy by cutting a fine slip band, a high stress was found to be required [57].

An increase in the elastic modulus of Au by the addition of Ti was observed in several studies [38]. The elastic modulus of as-cast Au-20 at. % Ti was reported to be about 106 GPa by Fischer and Kikuchi et. al. [38, 61]. An additional increase in elastic modulus was observed by heat treating the specimens [62].

2.2 Mechanical Properties

The pursuit of dependable performance in electrical contacts can be optimized by improving the mechanical properties, such as hardness and elastic modulus. Hardness is not a fundamental mechanical property of a material and it varies as the procedure to obtain the value changes. However, it is a measurement that is strongly dependent on the material's properties. While several methods can be used to obtain the mechanical properties of bulk materials, nanoindentation is one of the tools used to determine the hardness and elastic modulus of thin near surface layers.

2.2.1 Nanoindentation

Nanoindentation is primarily used as a technique to determine the mechanical properties of materials in small volumes. Nanoindentation determines two important properties: the hardness and modulus of elasticity of materials, by recording the depth of penetration of an indenter by a known applied load into the surface of the test specimen [63]. A typical load versus depth curve is shown in Figure 2.3. The complete loading and unloading curve, can be analyzed to determine the properties of the specimen [64]. The stiffness of the specimen, which is the slope of the unloading curve, can be

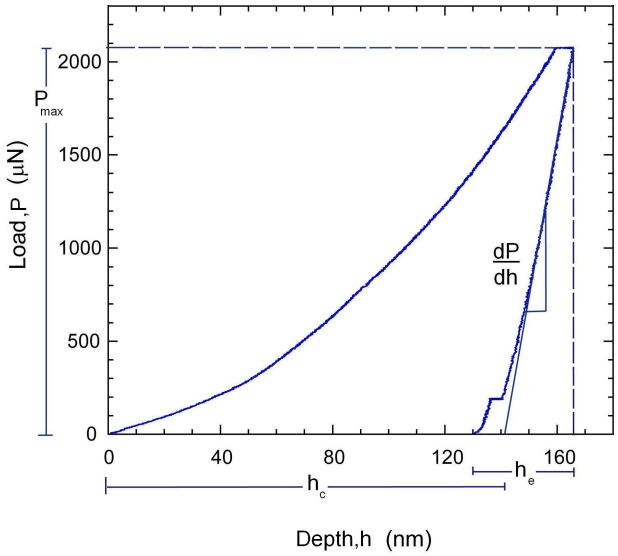

Figure 2.3: Load versus depth curve in nanoindentation.

measured experimentally. The measured stiffness correlates to the reduced elastic modulus (E_r) by Eqn. 2.1 where A is the projected area of elastic contact [64].

$$S = \frac{dP}{dh} = \frac{2}{\sqrt{\pi}} E_r \sqrt{A} \tag{2.1}$$

The projected area of elastic contact can be obtained by performing an optical measurement of the projected area. Oliver et. al. [64] proposed evaluating "A" by indenting on Al. The low hardness of Al allows for large indentations, simplifying measurement of mirror images. Although A in Eqn. 2.1 originated from a conical indenter, Bulychev et. al. [65] and Oliver et. al. [64] showed that the equation can also be applied to spherical, cylindrical and Berkovich indenters. The Berkovich 3-sided indenter was chosen based on the geometry of a Vickers indenter, as a common indenter used with a diamond tip with known properties. A conversion of Vickers (H_V) to nanoindentation hardness (H_N) was investigated by Mayo et. al. [66] based on height-to-area ratio, using Eqn. 2.2.

$$H_V = 0.927 H_N \tag{2.2}$$

Based on the indentations performed on Al, the area function for a Berkovich indenter can be obtained from the contact depth h_c (Eqn. 2.3),

$$A(h_c) = 24.5h_c^2 + C_1 h_c^1 + C_2 h_c^{1/2} + C_3 h_c^{1/4} + ... \tag{2.3}$$

where the constants C_1, C_2, C_3,... are based on the geometry of the indenter. The first term's coefficient is used to represent a perfect Berkovich indenter and the other coefficients are due to blunting of the tip and can be extrapolated by a graphical approach.

The contact depth h_c is the depth of the indenter when in full contact with the surface, as shown in Figure 2.4. By deriving the area of contact and measuring the stiffness, the reduced elastic

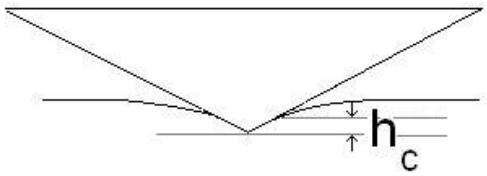

Figure 2.4: Schematic of indenter in "sinking in" position representing the h_c.

modulus can be obtained by Eqn. 2.1. By determining reduced elastic modulus, the elastic modulus can also be extracted by Eqn. 2.4,

$$\frac{1}{E_r} = \frac{1-\nu^2}{E} + \frac{1-\nu_i^2}{E_i} \tag{2.4}$$

where ν, E and E_r are Poisson's ratio, elastic modulus and reduced elastic modulus of the specimen, respectively, and ν_i and E_i are Poisson's ratio and elastic modulus of the indenter, respectively.

Mencik et. al. [67] compared five different functions to correspond to the elastic modulus obtained from the nanoindentation experiments. The functions were corresponded to linear, exponential, reciprocal exponential, the Gao's [68], and the Doerner-Nix's [69] function. Using 26 different specimens with nominal loads ranging from 1 mN to 1 N, and corresponding contact depths of 70 - 2530 nm, nanoindentation experiments were performed [67]. The films represented a wide variety of compositions, properties and geometries. The nominal load's range was divided into 6 - 28 intervals and averaged over 10 experiments. Gao's analytical function generally corresponded fairly well to the film/substrate behavior in nanoindentation experiments for the majority of composites. An exponential function approximates the results of experiments conducted on thin films and a linear function fit for small penetration depths in bulk films.

Additionally, the hardness of material can also be obtained by Eqn. 2.5,

$$H = \frac{P_{max}}{A} \tag{2.5}$$

where H is the hardness, P_{max} is the maximum load and A is the projected area of contact at the maximum load.

2.3 Tribological Performance

The surface topography and hardness of a material affects the tribological performance such as wear of the contact surfaces.

2.3.1 Surface Topography

Asperities and craters on the surface cause inhomogeneities in surface topography. Pruitt revealed that the surface roughness of thin metallic films depends on the substrate's material and roughness, the deposition method (sputtering, evaporation and electroplating) and the film thickness [17]. At the point of contact, an increase in stress causes cracks on the surface which leads to particle detachment from the surface or wear. The mechanical properties of the thin near surface layer has a very important role in the stress and wear analysis of the surface. The surface roughness of contacting bodies determines the distribution of nonuniform internal stresses in the near surface layer and eventually the type of fracture on the surface layer [70].

Recent investigations focused on changes in surface topography of contacts after high numbers of repeated cycles (above 10,000 cycles) which introduce material transfer [71–73] and distortion of surface asperities [74].

After a high number of cycles, both material transfer from one surface to another and compression of asperities regenerates the surface topography, and subsequently the contact area. The change in contact area alters the electrical properties, such as contact resistance, and adhesion of the contacts [71–73, 75–77].

While evolution of the contacts at the initial stages of repetitive contact has not been discussed widely, Doelling et. al. investigated the transformation of the surface topography during the initial stages of cycling empirically from change in contact resistance [3]. The results showed that asperity growth occurred in high power electrical contacts during the first 10 repeated cycles, by forming "nanospot welds" between the two attached contact surfaces. As the surfaces separated, the weld stretched, and eventually broke, developing a "spike like" surface which increased the overall roughness. The increase in roughness reduces the contact area, causing the contact resistance to increase.

Area of Contact

While two surfaces are in contact, the apparent contact area (A_a) may vary significantly from the actual contact area as shown in Figure 2.5. Assuming fully elastic behavior, the apparent contact area can be applied as an area of contact in the Hertzian model. Furthermore, modified models of the Hertz theory by Greenwood [78] and Williamson address surface roughness which is empirically obtained from applied loads and indirect observation of the contact area via contact resistance measurement and large displacements (due to plastic deformation) [7, 17]. The applied load and mechanical properties of the surfaces as well as the substrates significantly affect the area of contact and elastic-plastic behavior of contacts.

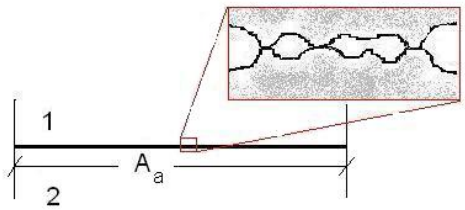

Figure 2.5: Schematic of the two bodies in contact. A_a represents the apparent contact area while the real contact area is the sum of the areas of the asperities in contact.

Pruitt et. al. presented the effect of contact displacement with respect to contact resistance and force in determining a more realistic contact area in Au films. Also, the main role of surface

topography in the contact resistance and electrical properties of electrical contacts was addressed [7].

2.3.2 Wear

Wear often occurs in contact surfaces. However, attempts can be made to control the severity. Reducing the surface roughness and increasing the hardness are a few approaches which can diminish wear [79].

Wear occurs when two surfaces are in contact and move relative to each other. Wear can be categorized as: abrasive wear, adhesive wear, fatigue wear and corrosive wear [79]. In adhesive wear, the adhesion between the two surfaces in contact causes some material to detach from the original surface as contacts are separated. In abrasive wear, usually the harder material cuts, fractures, or plastically deforms the softer material. Fatigue wear occurs when a crack initiates and propagates as contacts meet in a cyclic manner. Corrosive wear occurs as a result of reaction products, such as oxides being formed. By examination of worn surfaces, more than one wear mechanism may be seen on the surface. Fretting wear is also considered a wear mechanism though many debate the variables of the fretting process. Fretting wear or fretting fatigue is defined as a combined mechanical and chemical wear occurring in oscillating electrical contacts, when the normal force is large enough and an amplitude is small enough for fretting to take place without the displacement of debris [80, 81].

2.4 Electrical Properties

Resistivity is an electrical property of a material and another important factor for the selection of metallic layers used in a MEMS electrical contact. The resistivity is a measure of a material's ability to oppose electrical conduction. Resistivity, which is highly dependent on temperature, changes in a thin film compared to a bulk material. The divergence occurs as a result of many factors but predominantly from variation in the thin film thickness or size effect [82]. A common way to measure the resistivity of a material is by using the four point probe method. The four point probe method uses four similar, equally spaced probes in which two probes act as the current source and the others measure the voltage across. The linear arrangement of the four point probe is shown in Figure 2.6 [83]. The volume resistivity can be calculated using Eqn. 2.6,

$$\rho = \frac{\pi}{ln2} \times \frac{V}{I} \times t \times k \tag{2.6}$$

where ρ symbolizes the volume resistivity of a material (Ω-cm), V is the measured voltage (volts), I is the source current (amperes), t is the thickness of film (cm), and k is the geometry correction

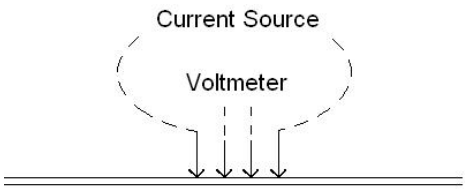

Figure 2.6: Schematic of four point probe

factor which is based on the ratio of probe spacing to the wafer diameter and ratio of the wafer thickness to the probe spacing [84].

The sheet resistance of material can also be obtained by using an Eqn. 2.7,

$$R_s = \frac{\rho}{t} \tag{2.7}$$

where R_s is the sheet resistance in Ω, and ρ and t are previously defined values.

Chapter 3

Experimental

The experimental approach taken in the present study was to first investigate the basic mechanical properties. Systematic studies were conducted to determine how the nanoscale surface and subsurface material structure affects the mechanical properties in atomic planar contacts.

3.1 Deposition Rate

The first study was made to investigate the effect of varying the deposition rate on the mechanical properties of Au thin films. A 700 nm polycrystalline Au was deposited by electron beam evaporation on a Si (100) wafer with different deposition rates of 1.5, 3, and 4.5 Å/s. To provide a diffusion barrier, 200 nm of SiO_2 was thermally grown on the Si. Prior to the deposition of Au, a 10 nm Ti film was deposited on the oxide layer to increase the adhesion of the Au to SiO_2. The Au films were deposited at MIT. The effect of the change in deposition rate on the surface topography, hardness and modulus of elasticity of these films was investigated using AFM and nanoindentation.

3.2 Adhesion Layer and Heat Treatment

In the second study, the effect of the underlying adhesion layer was investigated by depositing 20 nm Ti or Cr prior to deposition of the 700 nm Au film. Ti and Cr were used to increase the adhesion of the Au to SiO_2 by diffusion into the Au matrix [85]. A thermally grown 200 nm SiO_2 layer was deposited prior to the adhesion layer deposition to prevent the diffusion into the Si wafer.

In order to investigate the effect of heat treatment on the bonding of Au with SiO_2, the films were heat treated in N_2 for 1 h at 100° C and the change in mechanical properties resulting from

heat treatment was explored. Heat treatment could enhance the inter-diffusion of thin films and increase the adhesion of sublayers. These specimens were also provided by MIT.

3.3 The Modification of Polycrystalline Au Films by Mo Deposition

Au films were modified to possibly enhance the tribological performance and to decrease the effect of fretting and wear. A 20 nm Mo layer was deposited on a 700 nm electron beam evaporated Au film. The immiscible thin near-surface Mo on Au was chosen to possibly prevent the occurrence of Au-Au bonding during the repeated cycling of contacts. The effect of Mo/Au on the wear resistance properties as well as friction and mechanical properties were investigated. The preparation of the modified Mo/Au films was performed at LANL.

The nanoindentation experiments were performed, along with tribological experiments including microscratching and wear experiments. The shakedown investigation of mechanical properties and tribological performance on the modified Au films with Mo deposition did not, however, constitute the primary focus of the present study, and therefore the results obtained have been included as Appendix A.

3.3.1 Tribological Measurements: Microscratching and Wear Experiments

Microscratching and wear experiments were performed on Mo/Au and pure Au thin films to examine the tribological properties. A spherical diamond tip indenter and a two-dimensional transducer were used to perform the aforementioned experiments using a Hysitron Nanoindenter combined with an AFM system. While a single pass scratch with a gradual increase in load was utilized for the microscratch experiment performed on the surface, multipass scratch tests were carried out for the wear experiments. Similar experiments were performed using a Hysitron nanoindenter by Ott et. al. [86].

During the microscratching experiments, the surface topography of the films was obtained before and after the scratches were made by the indenter tip. Scratches 10 μm in length were made by increasing the load from 0 to 200, 500, and 1000 μN loads, respectively. The scratch depth and the formation of the material pile up along the sides were examined. The coefficient of friction was obtained by dividing the lateral force by the normal force.

Wear experiments were performed by using multiple scratches on the same surface. Ten multiple

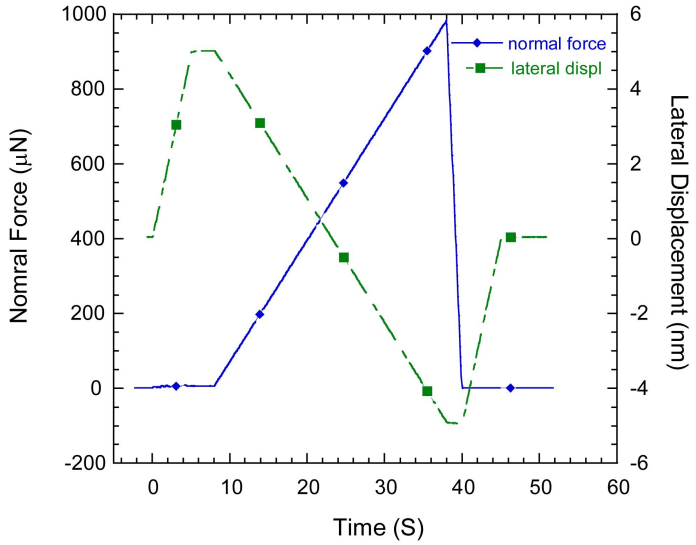

Figure 3.1: Microscratching Experiment Load function

passes, with an equal sustained load, were performed over a 4 μm scratch length to induce wear on the surface of the specimens. The wear experiments were carried out using 200, 500 and 1000 μN loads.

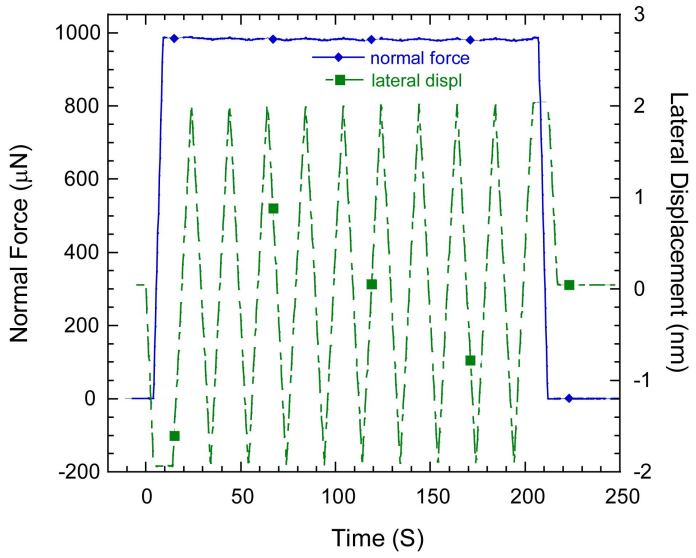

Figure 3.2: Wear experiment load function

3.4 The Modification of Polycrystalline Au Films by Co-evaporation with Ti

One approach to improve the hardness of the Au layer is by alloying with Ti. As discussed in Chapter 2, a small Ti content has been reported to increase the hardness of Au. The present study was aimed at investigating the mechanical properties of the modified Au films by homogeneous and coherent formation of solid solutions and an intermetallic compound in the thin near surface layer by co-evaporation with a small concentration of Ti. Alloying of Au with various atomic percentages of Ti upon heat treatment was investigated to determine the change in mechanical and electrical properties within a 0 - 20 at. % Ti range.

A 10 nm Ti adhesion layer was evaporated onto a single crystal Si wafer prior to co-deposition of Au and Ti. The fabrication of Au-Ti (purity of 99.999 % Au pellets) thin films were performed at room temperature at LANL. The substrate was neither heated nor cooled, however, the substrate temperature increased from about 25°C to about 55°C during deposition. The nanocomposite Au-Ti films were synthesized by simultaneous co-evaporation with different deposition rates (the combined deposition rate was 10 Å/sec) to provide the targeted ratios of 2, 8, and 20 at. % of Ti with Au in a 1 μm thick film. The electron beam co-evaporation process was performed by utilizing two identical Leybold-Heraeus SV6/UHV electron beam sources controlled with two identical Inficon XTC deposition controllers. Each composition with distinct physical and chemical characteristics was selected and studied.

The solid solution strengthening study was performed by co-evaporation of 2 at. % Ti and 8 at. % Ti. According to the phase diagram of Au-Ti, by melting Au and Ti at a specific composition to form a mixture of an alloy and solidify the alloy (as a cast) the following microstructures are expected. Whereas 2 at. % Ti is mainly a single phase α solid solution, 8 at. % Ti partially carries α precipitates within the α and Au_4Ti matrix (Figure 3.3). In the two selected alloys of 2 and 8 at. % Ti, a super saturated solid solution can theoretically be obtained upon proper heat treatment. The outcome could be achieved due to the full solubility of 10.5 at. % Ti in Au above the peritectic temperature, 1123°C [42]. Meanwhile attempts to form intermetallic compounds of Au_4Ti were conducted by co-evaporation of 20 at. % Ti with Au. According to the phase diagram in Figure 3.3, Au_4Ti should co-exist with α solid solution within 10.5 at. % Ti and 20 at. % Ti at room temperature.

Atomic force microscopy was performed to investigate the change in surface morphology and

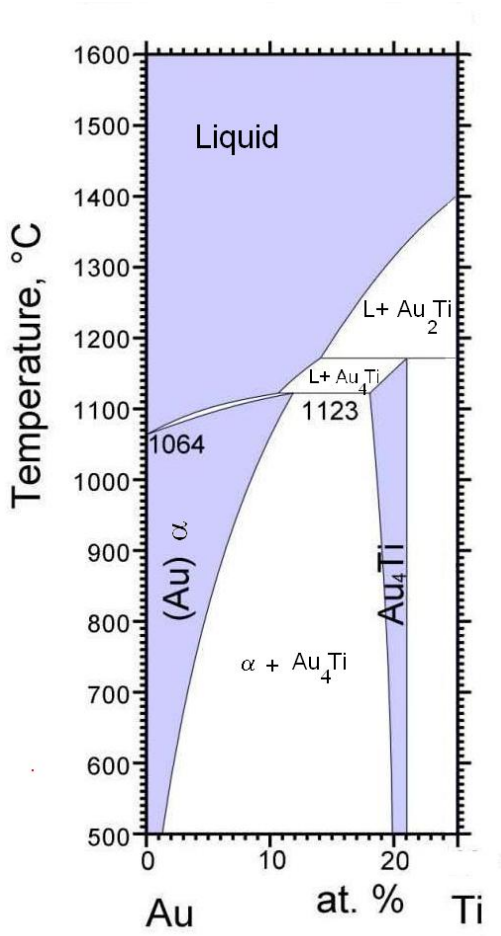

Figure 3.3: Au-Ti phase diagram modified by [56].

surface roughness by the addition of Ti in Au. Nanoindentation experiments were performed on the Au-Ti alloys to determine the change in mechanical properties of Au by the addition of Ti. The electrical resistivity of the films was determined using the four point probe method.

3.4.1 Elemental Analysis

The composition of the Au-Ti films was measured using Particle Induced X-ray Emission (PIXE). PIXE is a powerful technique to measure elemental concentration. While x-ray emission from PIXE and Energy Dispersive Spectroscopy using X-Ray (EDX or EDS) is the same process, PIXE has a higher sensitivity due to a higher signal-to-noise ratio [87]. Bombardment of ions with sufficient energy (0.3 - 10 MeV) can create an empty electron core by electron excitation. The empty core can be filled by the falling of an outer shell electron while the transition produces an x-ray with a characteristic wavelength. The intensities of the various wavelengths can identify and quantify

the elements that are present in the specimen [88]. PIXE is commonly used for thin film surfaces rather than bulk materials. For some materials with low Z elements (atomic number), PIXE has advantages over Rutherford Backscattering Spectrometry (RBS) [88].

3.4.2 Structural Analysis

X-Ray Diffraction (XRD) is a powerful technique commonly used for thin films to characterize the crystal phases and structural properties of these phases [88]. Structural properties, such as grain size, epitaxy, phase composition, preferred orientation and defect structure can be obtained with XRD. XRD is more sensitive to high Z elements due to larger intensities diffracted from these elements. In XRD measurements, the diffracted intensity is generally measured in terms of 2θ. Figure 3.4 illustrates the principles of XRD measurement, where 2θ is the angle between the incident and the diffracted x-rays and θ is the angle between the incident and atomic plane.

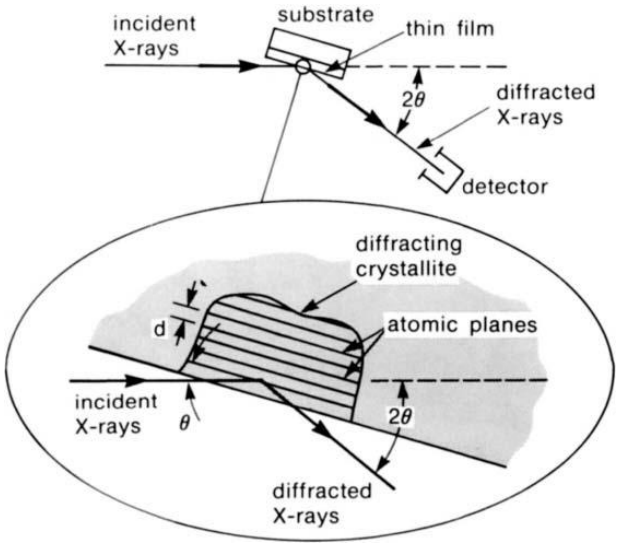

Figure 3.4: Principles of XRD measurement [88]

In a crystalline material, the atomic planes are separated by a spacing d, shown in Figure 3.4. If a portion of emitted x-rays is reflected from the plane (constructive interference) the x-ray wavelength is represented by Bragg's law in Eq. 3.1,

$$\lambda = 2\ d_{hkl}\ sin(\theta_{hkl}) \tag{3.1}$$

where λ is the x-ray wavelength, and h, k, and l are the Miller indices of the crystal plane. While the applicability of Bragg's law is a necessary condition for constructive interference, it is not sufficient for diffraction to occur.

In the diffractometer, the detector should be placed at an angle of 2θ, for diffraction to be observed. XRD measurements were used to determine the structural formation of the Au-Ti alloys and were undertaken at the OSU Chemistry Department using a Bruker D8 Advance x-ray powder diffractometer. The instrument was operated using a Cu-Kα x-ray source in the θ-2θ mode with a current and voltage of 30 mA and 40 KV, respectively.

The crystallite or grain size of the Au-Ti films was determined by measuring all the peaks on the obtained spectra using WIN-CRYSIZE software. As the broadening of the peaks could be influenced by the instrument effects and the lattice strain, it was necessary that they be subtracted using a pure Pb calibration. The grain size was thereby deduced from the broadening of the peak and processed from the utilized software [89].

3.5 Investigation of the Effect of Heat Treatment on Co-deposited Au-Ti Films

As mentioned previously, the age hardening behavior of cast Au-Ti alloys was reported in the literature [57]. The effect of age hardening (precipitate strengthening) on nominal Au-8 at. % Ti films was investigated by heat treating the as-deposited specimens to 550°C for 1, 5, 10, 30, 60, 100, 600, and 1000 min. It should be noted that Figure 3.3 ends at 500°C and the Ti solubility limit in Au would be much less at room temperature. The heat treatment temperature at 550°C is well above 0.5 of the melting temperature, so diffusion should ocurr readily. The heat treatment was performed using a Thermolyne Furnace Model # 62700. The specimens were then air quenched by placing on a room temperature Al plate. However, the cooling rate should not affect the microstruture substantially. To confirm the repeatability of the results and validate the insignificant effect of cooling, a second experimental trial was performed. The films were placed in air to cool slower at room temperature in the second sets of experiments. The initial step of the age-hardening procedure, solution heat treatment, was eliminated. The assumption was made that e-beam co-evaporated Au-Ti (Au and Ti evaporation temperatures $\approx$ 1132 and 1453 °C, respectively [14]) deposited on a cold Si wafer (from 25 - 55°C during deposition) would correspond to heat treating at a very high temperature and quenching subsequently (quench rate of about 10^{10}°C/sec [14]), which would form a single phase.

Surface topography was investigated using optical microscopy and AFM. Raman spectroscopy, combined with AFM, was also used to identify the surface elements. The confocal Raman spec-

troscopy was performed using a 532 nm wavelength Nd-YAG laser. The further procedure and specifications of the system are discussed elsewhere [90]. Nanoindentation was then performed to investigate the effect of precipitate strengthening on the hardness of the Au-Ti thin films.

3.6 Nanoindentation Experiments

Nanoindentation was performed using a load-controlled Hysitron commercial nanoindenter. A Berkovich diamond indenter, a three sided pyramid, and a transducer with a capability of maximum load and displacement of 10 mN and 5 μm, respectively, was used for all the nanoindentation experiments. The mechanical properties of reduced elastic modulus and hardness were obtained. The compliance and area function of the Berkovich indenter were obtained following the calibration procedure proposed by Oliver and Pharr [64], using Al and fused SiO_2. Before each set of experiments, the instrument and the sample were allowed to thermally equilibrate for 10 - 12 hours.

Prior to the indentation, the surfaces were scanned, using the indenter tip to verify the surface topography of the film. The instrument drift rate was checked before each indentations to verify a value of less than 0.1 nm/s averaged over a 5 s interval. A single loading indentation was then performed during a 30 s loading period with a 60 s holding time at the maximum load to account for creep effects, followed by a 10 s unloading and 60 s. holding interval at a 10 % maximum load to account for thermal drift [64]. All indentations were performed over an average of at least 5 experiments. The error bars in the experimental results show the maximum and minimum values in the 5 experiments performed at each load.

The hardness and reduced elastic modulus as a function of distance from the surface of the film were determined, from 10 times the surface roughness as a minimum in contact depth to a maximum contact depth of about 20 % of the film thickness. The minimum 10 - 20 times surface roughness is suggested to eliminate the effect of surface asperities [64].

The surface roughness of the films was obtained using the AFM prior to the nanoindentation experiments. The surfaces were scanned in Tapping Mode, using a RTESP5 probe, which has a single cantilever of (n)-doped Si with a maximum tip radius of about 12 nm.

3.7 Four Point Probe Experiments

The resistivity of the thin multilayer films was obtained at room temperature using the four point probe method. A Veeco FPP-5000 model was used to perform all the resistivity measurements. The

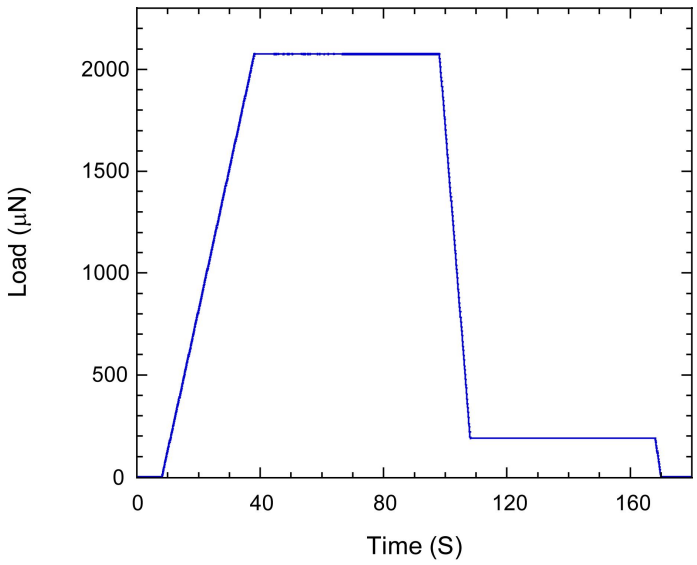

Figure 3.5: Load versus time graph of nanoindentation experiments.

FPP-5000 is a fully automated, simple device designed for measuring the resistivity of thin films. For each measurement, the input amplifier was automatically calibrated to vary the current from 5 mΩ to 5 kΩ and to ensure an accuracy of about ± 0.5 %. The test current minimized the current passing through to maximize the received voltage signal. The specimens were mounted on a clean wafer using adhesive tape and placed on the wafer holder facing the probes. By closing the FPP-5000 cover, a platten which the specimen was placed on traveled a constant distance. The probes penetrated into the film and the measurements were obtained after a few seconds of applying manual force. The FPP-5000 was designed to apply constant probe force independent of operator force. The geometrical correction factors of the specimens were adjusted depending on the specimen's size and shape [91]. By inputing the film thickness (1 μm), the resistivity was obtained in $\mu\Omega$-cm.

Chapter 4

Results and Discussion

The results presented are organized according to a systematic investigation of Au. The first three sections are the baseline studies of pure Au thin films, when varying the deposition rate, heat treatment and adhesion layer. The preparation of the pure Au films of this investigation was performed at MIT. The next section describes the investigation on the mechanical and electrical properties of co-evaporated Au-Ti films by structural analysis, which were synthesized at LANL. The final section discusses the investigation of the heat-treated Au-Ti films. The shakedown studies of the Au films modified by Mo deposition, are presented in Appendix A, since this did not constitute the major focus of the present work.

4.1 The Effect of Deposition Rate on Polycrystalline Au Thin Films

The first baseline study on the Au films was conducted to investigate the effect of deposition rate on the hardness and elastic modulus. Three deposition rates of 1.5, 3 and 4.5 Å/s were chosen. AFM was used to measure the surface topography of the films. E-beam evaporated Au typically deposits as a homogeneous nodular film [92], which was consistent with the observations in the present study as shown in Figure 4.1. The grains of the Au films could contain several nodules. The number of nodules within the grain could vary by heat treatment and modifications performed on the film. The surface roughness obtained was between 4 - 5 nm Ra over a 1 μm^2 scan area.

The effect of deposition rate on hardness and elastic modulus is shown in Figures 4.2 and 4.3. The results are shown with respect to the contact depth (h_c). The error bars show the maximum and minimum values for the 5 nanoindentations performed for each load. Prior investigations on

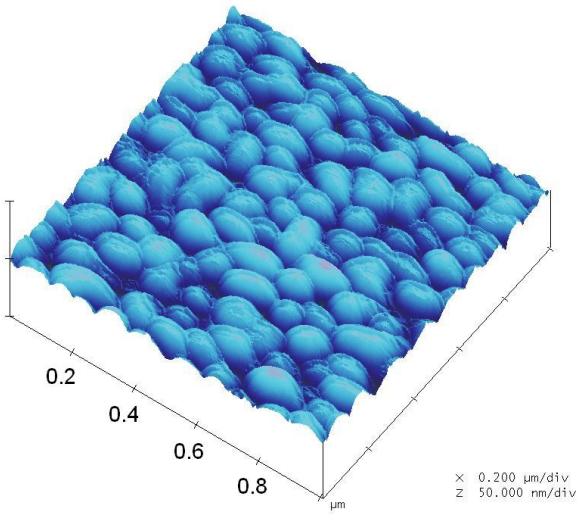

Figure 4.1: AFM surface topography of an evaporated Au film (Au/Ti/SiO_2/Si) showing nodules over a 1 μm^2 scan area.

effect of deposition rate on the mechanical properties of e-beam evaporated films were not found in the literature. However, different deposition techniques have been found to vary the mechanical properties of thin films by changing the deposition rate, i.e., magnetron sputtered films with higher deposition rate were characterized with higher residual stress and a denser structure, leading to a higher hardness [93].

An increase in hardness was observed for the lowest deposition rate (1.5 Å/s) at contact depths above 140 nm, $h_c \geq 140$ nm. Nevertheless, the hardness and elastic modulus over the range of deposition rates studied were nearly identical at h_c less than 140 nm. The hardness of the Au films was found to be between 1 - 1.5 GPa, which was consistent to the reported values of 1 - 2.3 GPa [7, 13, 92]. The hardness values, at contact depths greater than 140 nm, increased due to the substrate effect (the hardness of bulk Si has been reported to be about 8 GPa, $h_c \leq 30$ nm [94]). As contact depth increased, the elastic modulus approached the value of 160 GPa reported for the elastic modulus of single crystal bulk Si [94].

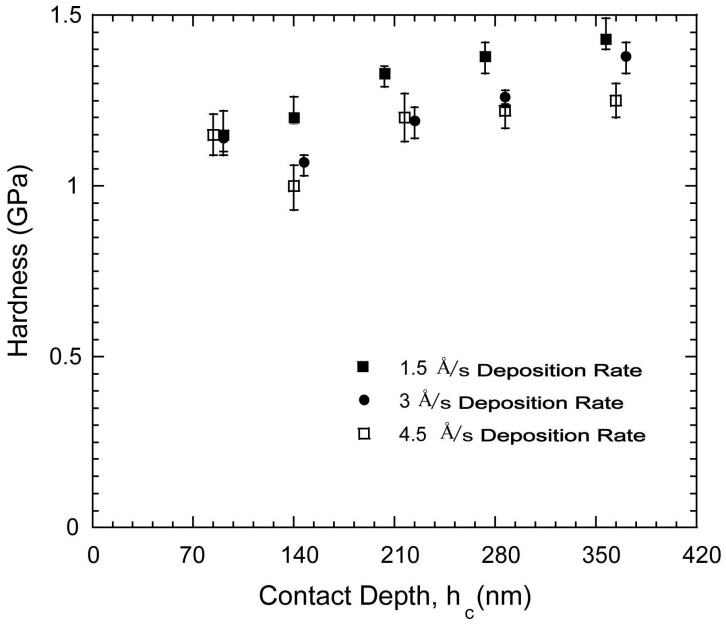

Figure 4.2: Effect of deposition rate on hardness of Au films.

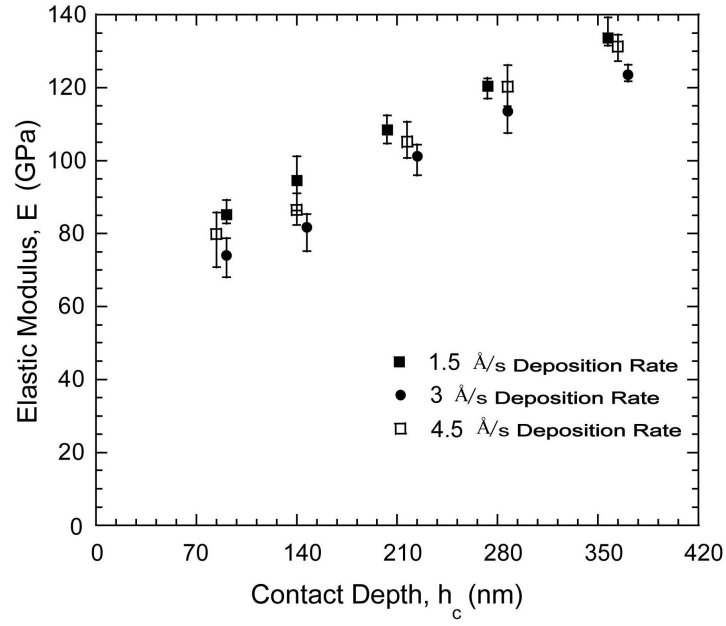

Figure 4.3: Effect of deposition rate on elastic modulus of Au films.

4.2 The Effect of Adhesion Layer and Heat Treatment on Polycrystalline Au Thin Films

The second investigation was undertaken to examine the effect of the underlying adhesion layer on the mechanical properties. The thin (20 nm) Cr or Ti adhesion layers were deposited prior to

the 700 nm Au film. To increase the adhesion of Au to SiO_2, the effect of heat treatment was also investigated. It was previously reported in the literature that heat treating the Au/Ti/Si (or Au/Cr/Si) films led to an increase in bonding of Au and Si due to the formation of $TiSi_2$ (or $CrSi_2$) at the interface [85]. The silicidation was reported to be required for eutectic formation of Au-Si, resulting in bonding between Au and Si [85]. The deficiency in silicidation could cause delamination of the films from the substrate. The surface topography of as-deposited and heat treated Au films with Cr and Ti adhesion layers was investigated by AFM. The measured surface roughnesses over a 1 μm^2 scan area were between 2.5 - 3.5 nm Ra. The e-beam evaporated films were subjected to heat treatment, and the resulting surface topography is shown in Figure 4.4. The as-deposited $Au/Cr/SiO_2/Si$ film had a similar surface topography as the heat treated $Au/Ti/SiO_2/Si$ film. The observed grain growth and the separation of the grains by distinct surface cracks was suggested to be a result of a volumetric reduction mechanism increasing tensile stress in the Au film [1].

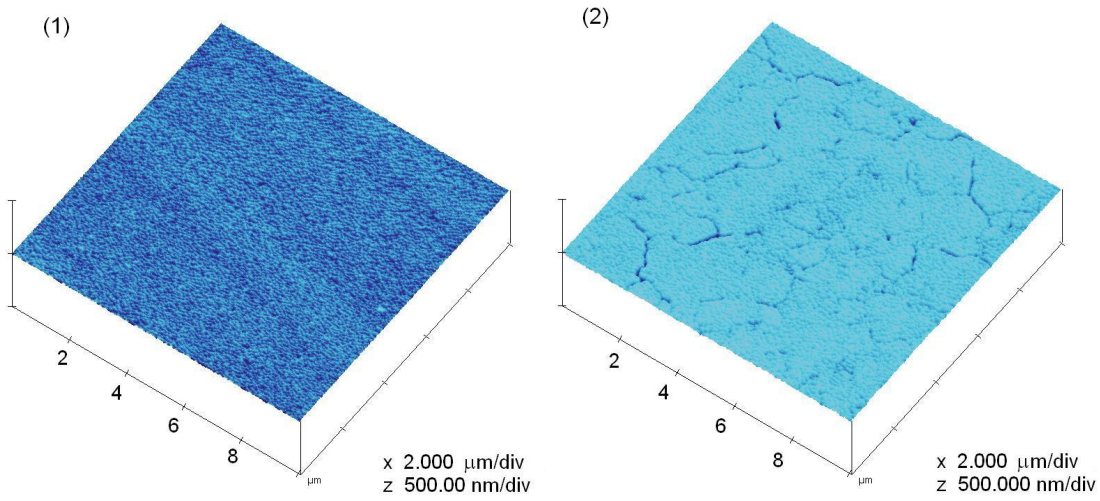

Figure 4.4: AFM images of (1) heat treated $Au/Ti/SiO_2/Si$, (2) heat treated $Au/Cr/SiO_2/Si$ specimens over a 100 μm^2 scan area.

The effect of heat treatment and the adhesion layer on the mechanical properties were investigated by nanoindentation. Figures 4.5 and 4.6 show the hardness and elastic modulus of the heat treated Au films with different adhesion layers. A decrease in hardness as the contact depth increased, up to about 140 nm, shows the "indentation size effect" [92, 95]. The effect showed a higher hardness at shallow depths in the thin films compared to the bulk material. The hardness of the thin films approaches the bulk value as the contact depth increases. The range of the nanoindentation size effect is submicrometer and is commonly explained by nucleation and interaction of dislocations [10, 92].

As the indentation depth increases, the increasing effect of the substrate causes the hardness to increase. The hardness and elastic modulus of the $Au/Cr/SiO_2/Si$ films were reported to be about 1.7 GPa and 88 GPa, respectively, [13, 92, 96], which corresponded to the obtained values shown in Figures 4.5 and 4.6. According to the inset images of Figures 4.5 and 4.6, no significant change due to the adhesion layers or heat treatment was seen in the mechanical properties of Au.

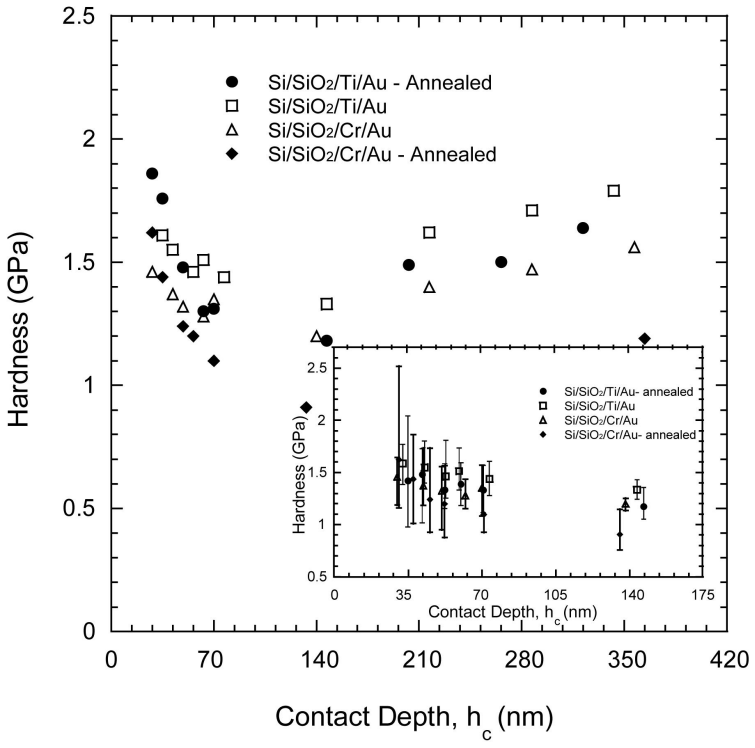

Figure 4.5: Effect of heat treatment and adhesion layer on hardness of Au films. The inset shows the data obtained up to 140 nm contact depth.

Four point probe measurements were conducted on the Au specimens with the Ti adhesion layers and the resistivity was found to be about 2.24 $\mu\Omega$-cm and 2.36 $\mu\Omega$-cm, respectively, for the heat treated and as-deposited films. The resistivity obtained for the Au films with Cr adhesion layers was higher, about 4.36 $\mu\Omega$-cm and 3.39 $\mu\Omega$-cm for the heat treated and as-deposited layers, respectively. The resistivity of Au thin films has been reported to change as deposition temperature, surface roughness, and temperature of the films change [97]. The resistivity of pure Au thin films at room temperature (68 F/293 K) has been reported in the literature to be about 3.1 - 3.9 $\mu\Omega$-cm [97, 98], consistent with the results obtained in the present study.

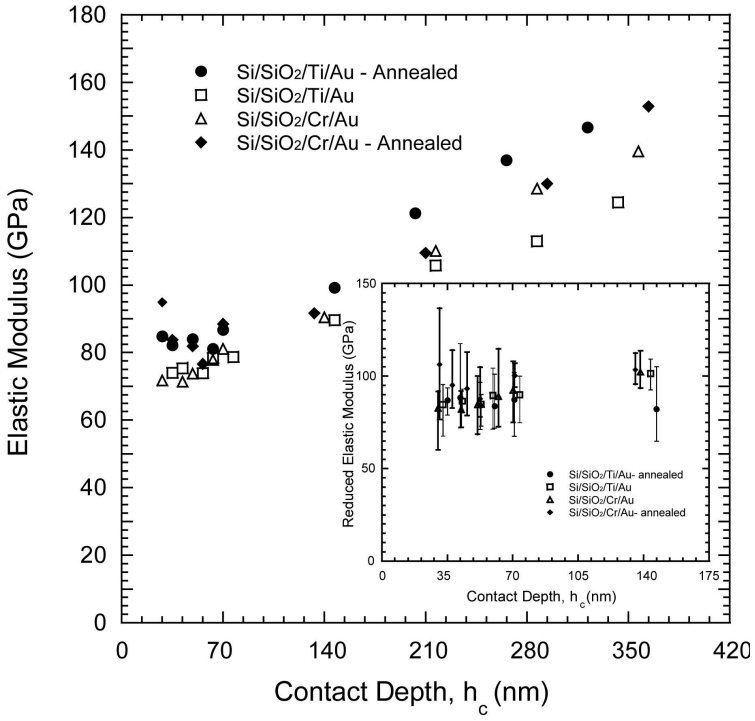

Figure 4.6: Effect of heat treatment and adhesion layer on elastic modulus of Au films. The inset shows the reduced elastic modulus obtained up to 140 nm contact depth.

4.3 The Modification of Au Films by Co-evaporation of Au and Ti

Co-evaporated Au-Ti films were prepared to obtain targeted compositions of 2, 8 and 20 at. % Ti with 98, 92 and 80 at. % Au, respectively. The highest atomic percentage (20 at. %) was aimed at obtaining compound formation of Au_4Ti. However, the amount of Ti deposited was found to be less than expected, and therefore more specimens were synthesized to achieve the initial goal of Au-20 at. % Ti. The new films provided a wider range within the Au-Ti phase diagram shown in Figure 4.7, in the combined region of solid solution and intermetallic compound.

4.3.1 Elemental Analysis by PIXE

PIXE was used to quantify the composition of the Au-Ti films. PIXE's detection limit is on the order of ppm [99]. PIXE results obtained on the Au-Ti films showed less Ti than expected. Table 4.1 shows the actual Ti amount in the co-evaporated Au-Ti films measured by PIXE. The position of the specimens according to the PIXE measurements are also indicated on the phase diagram in Figure

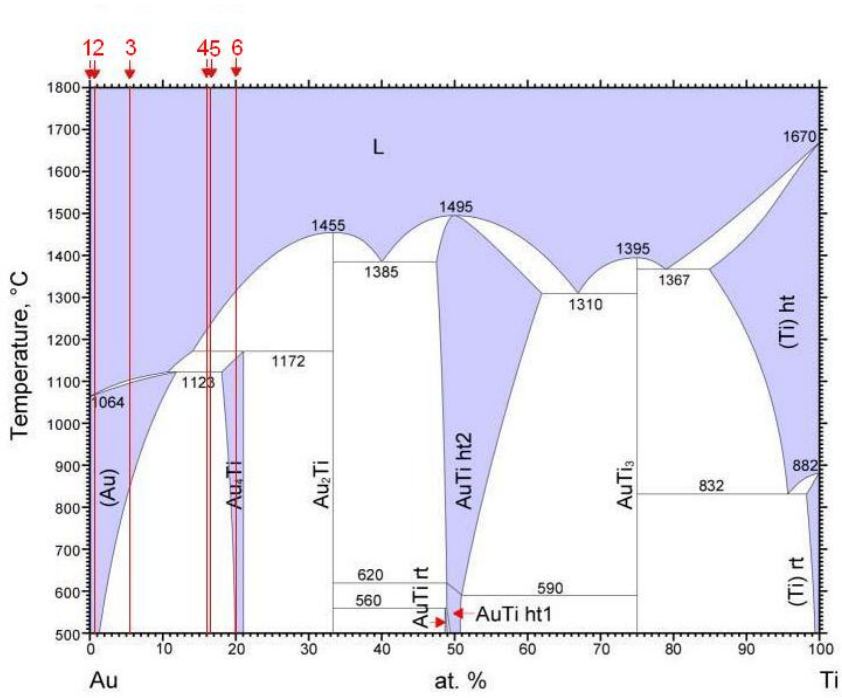

Figure 4.7: Phase diagram of Au-Ti indicating the composition of the co-evaporated Au-Ti films.

4.7.

Table 4.1: Co-evaporated Au-Ti films properties

Specimens (#)	Specimens (Nominal Values)	PIXE (% Ti)	Surface Roughness,Ra (nm)	Resistivity ($\mu\Omega$-cm)
1	Pure Au	—	3.2	3.3
2	Au-2 at. % Ti	0.7	4.4	11.6
3	Au-8 at. % Ti	5.6	1.9	96.4
4	Au-20 at. % Ti	16	1.1	212
5	Au-20 at. % Ti	16.4	4.2	220
6	Au-20 at. % Ti	19.8	0.6	266

4.3.2 Surface Topography

The surface topography of the Au-Ti films was obtained using AFM. Figure 4.8 shows the evolution in surface morphology by the addition of Ti for a 1 μm thick film. The surface roughness of the films was obtained over a 1 μm^2 area. Tabulated values shown in Table 4.1 are an average of 3 Ra measurements and AFM scans over different regions of the Au-Ti films. The AFM images show the evolution in surface topography and the downsizing of nodules with increasing Ti content. This could be explained by the reduction in grain size which was previously reported in the literature as grain refining in cast Au-Ti [37].

During the synthesis of the thin films, significant changes in temperature of the film and the substrate could have introduced strains into the film due to differences in thermal expansion coefficients, and thicknesses between the film and the substrate [100]. The strains could have led to increases in tensile or compressive residual stresses. These stresses can be relaxed by the formation of cracks induced by generating dislocations [101,102], dislocation glide [100], surface diffusion [103], and twin formation [104].

The thermal expansion coefficients of Au-6.3 at. % Ti (1.6 wt. %) and Si were reported to be about 14.4 $\pm$ 0.3 $\times$ $10^{-6}/^{\circ}$C [105] and 7.9 $\pm$ 0.24 $\times$ $10^{-6}/^{\circ}$C [106], respectively. While it was reported that a large mismatch between the thermal expansion coefficients of the film and the substrate increases the residual stress (tensile if the thermal expansion coefficient of the film is greater than the substrate), the thermal expansion coefficient of Au-Ti alloys with less than 10 at. % Ti was reported to decrease as the Ti amount increased [38]. Therefore, the evolution of the cracks observed in the specimens of 16, 16.4, and 19.8 at. % Ti in Figure 4.9 are most likely not due to this effect.

Moreover, despite that cracks were previously reported to appear by changing the thickness of the films compared to the substrate [107], the thickness of all the Au-Ti films were approximately constant. Therefore, the development of cracks in Au-(16 at. % and above) Ti alloys presumably did not depend on the thickness, but rather, by an increase in residual stress possibly due to an increase in the content of Au_4Ti precipitates [108].

In a study by Masahiro, surface diffusion of Au to Ti was reported in bilayer Au-Ti films [54]. In another study, diffusion of Au to Ti, as commonly seen in bulk materials, was denied and it was reported that Ti diffuses in Au in thin films [109]. In either case, as a result of the additional Ti, surface diffusion of Ti in Au or Au in Ti could increase and lead to the formation of crack-like grain boundary diffusion wedges on the surface, as explained by Gao et. al. and Nix et. al. [103, 110].

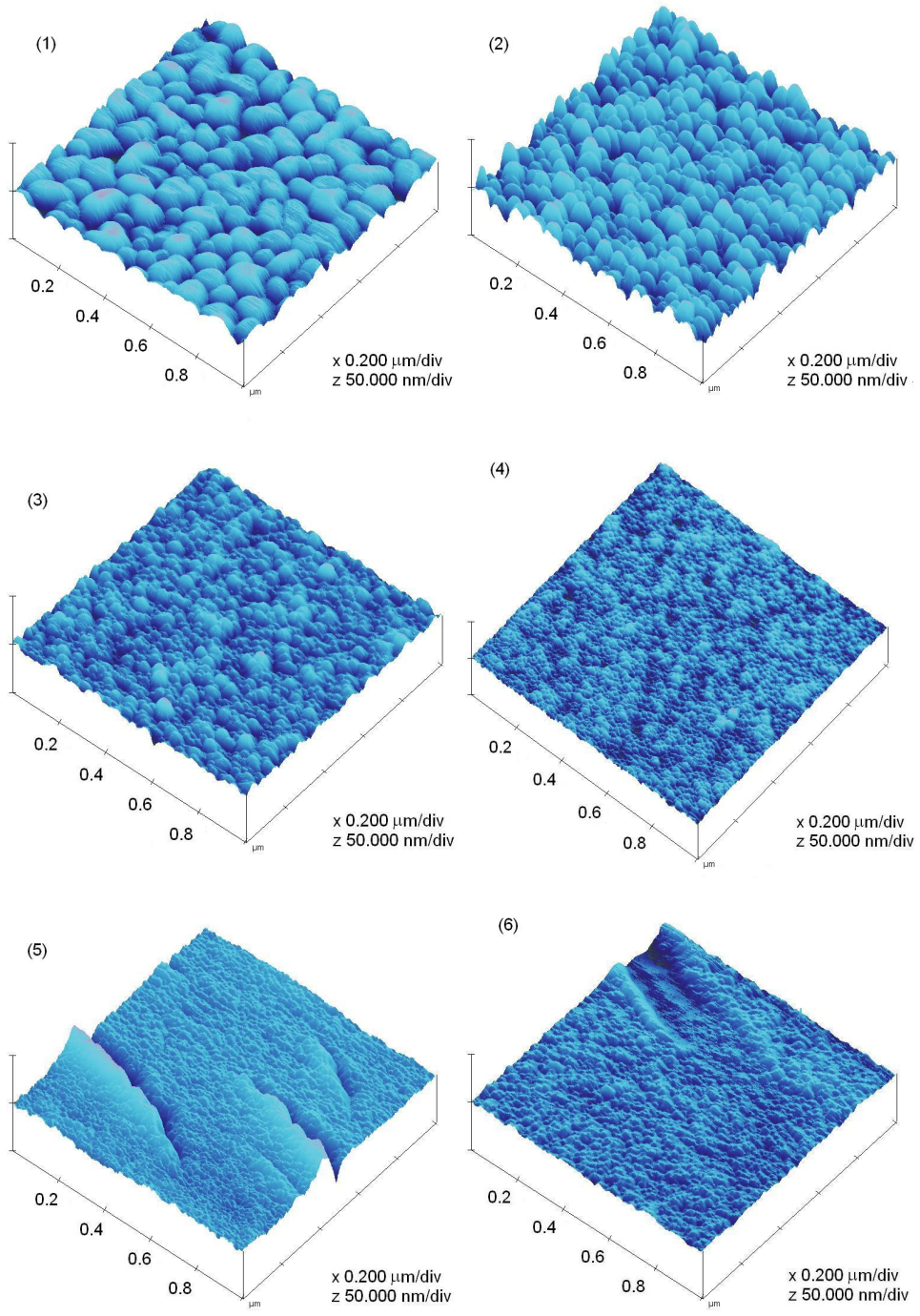

Figure 4.8: AFM scan over a 1 μm^2 area of (1) Pure Au, (2) Au-0.7 at. % Ti, (3) Au-5.6 at. % Ti, (4) Au-16 at. % Ti, (5) Au-16.4 at. % Ti, (6) Au-19.8 at. % Ti

Additionally, Poate et. al. reported the potential chemical sink of Ti atoms on the surface of thin films by formation of TiO_2 after heat treating in air [51]. The chemical sink could have also formed

during co-evaporation of Au and Ti in air. Furthermore, a high-resolution TEM (HRTEM) study by Van Heerden revealed the anti-parallel twin formation of Au_4Ti [47, 60]. The stress from twin formation of Au_4Ti could have also generated the cracks as the Ti concentration increased. Although the cracks on the surface could have resulted from stress relaxation from one or multiple reasons, the determination of the specific reason requires further investigation.

Surface cracks were not observed in the AFM or optical microscopy images in Au-Ti alloys of less than 11 at. % Ti, as predicted. The prediction of surface cracks from the bulk phase diagram by Burton et. al. was based on the distribution of liquid and solute in the solid/liquid equilibruim [111]. Refering to the phase diagram of Au-Ti (Figure 4.10), at a constant at. % Ti, (i.e., 5.6 at. % Ti), by decreasing the temperature from the evaporation temperature (Au and Ti e-beam evaporation temperatures of $\approx$ 1132 and 1453 °C, respectively [14]), the concentration of the constituents of solids, α (or Au_4Ti if above 11 at. % Ti), remains richer in solute than the liquid phase. Therefore, according to the analogy of Burton et. al. no surface cracks should have been observed. However, the proposed prediction was not consistent with the Au-Ti films with higher atomic percentages (16 and above). This could be as a result of the deposition technique used in the present study by co-evaporation of Au and Ti which solidifies Au and Ti simultanously without any interaction prior to deposition. Although the Au-16 at. % Ti, Au-16.4 at. % Ti and Au-20 at. % Ti exhibited cracks on the surface, no trend was observed in the broadening, spacing and deepening of cracks in the three aforementioned specimens (Figure 4.9).

4.3.3 Crystal Structural Analysis

X-ray diffraction measurements are shown in Figure 4.11. As a result of the similarity in diffraction patterns between Au_4Ti and the Au solid solution (α), the XRD measurement is not capable of detecting the formation of the Au_4Ti compound [42]. The 2θ diffraction results indicated Au(111) and Au(200) peaks, as denoted on the spectra [112]. The d-spacing of the peaks was calculated and identified assuming a Cu-kα source wavelength of 1.5406 Å. The absence of a Ti peak suggests that the deposited Ti in the Au-Ti films is not crystalline and the detection of the deposited Ti requires further experiments. X-Ray Photoelectron Spectroscopy (XPS) or TEM may possibly be able to determine whether Ti deposited in an amorphous phase or interacted with the Au. The interaction could be either by full solubility with the Au or transformation to an Au_4Ti compound. While crystal structure of deposited Ti was reported as α-Ti (HCP) or β-Ti (BCC), a FCC crystal structure of an e-beam evaporated Ti, in the Ti/6H-SiC interface was reported by HRTEM [113]. It

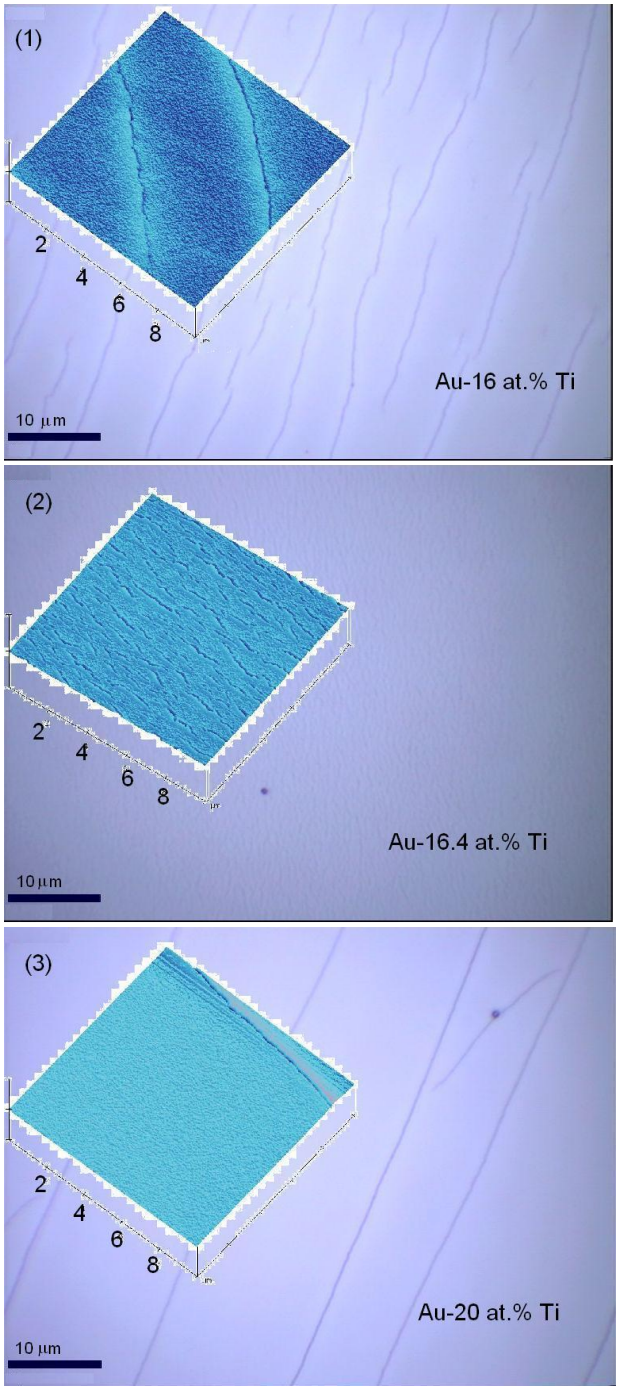

Figure 4.9: Optical and AFM images of Au-16 at. % Ti, Au-16.4 at. % Ti, and Au-19.8 at. % Ti. AFM was conducted over an area of 100 μm^2 with a 500 nm Z scale.

was reported the formation of FCC-Ti structure occurred to maximize the coherency at the interface.

As shown in Figures 4.11 - 4.14, the Au(200) and Au(111) peaks broadened as the Ti amount increased which generally indicates the reduction in grain or crystallite size and/or a non-uniformity

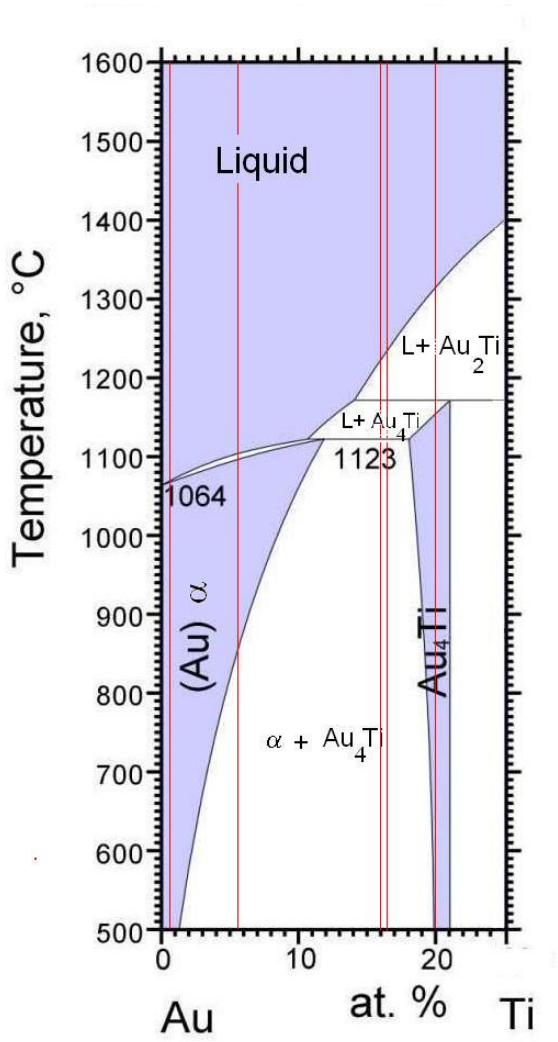

Figure 4.10: Phase diagram of Au-Ti, modified after [56]

of residual stresses within the lattice or lattice strain [114,115]. Both factors, the reduction in grain size and the increase in residual stress, indicated by the formation of cracks, are supported by the analysis of the surface topography in the previous section.

The average crystallite/grain size of the Au-Ti alloys was determined by measuring the broadening of the peaks using the modified Scherrer equation [115]. The average grain size decreased as Ti amount increased in the Au-Ti films from about 51 nm, for pure Au, to about 15 nm for Au-16.4 at. % Ti (Figure 4.15). The decrease in the grain size was consistent with the AFM images obtained of the surfaces. It should be noted that the grain size obtained was only determined for the Au peaks observed from the XRD data. Therefore, the possibility of the deposition of amorphous Ti was ignored and as a result accounting for the Ti presence in the calculation of grain size was as

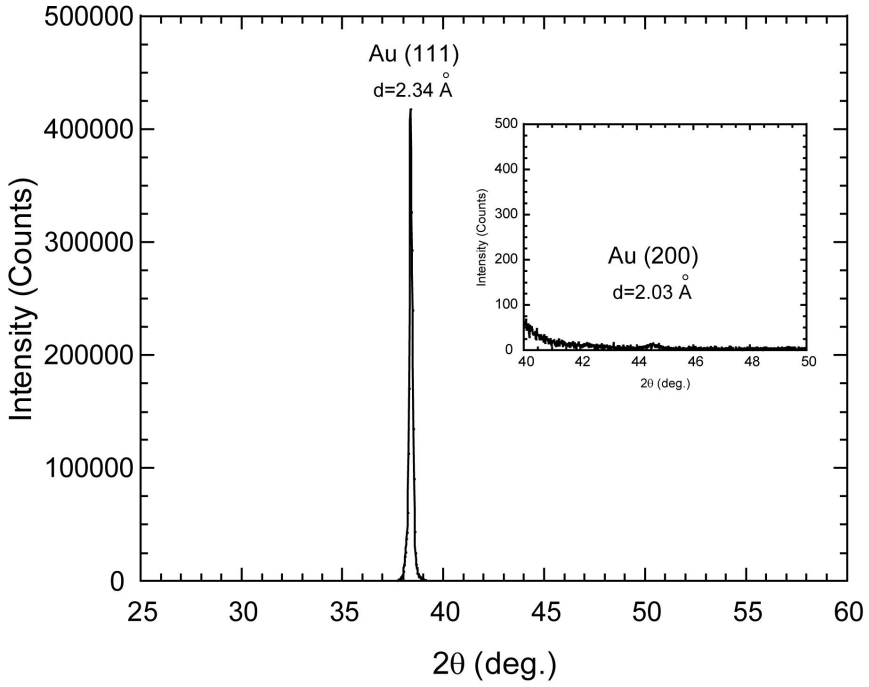

Figure 4.11: XRD measurement of pure Au film.

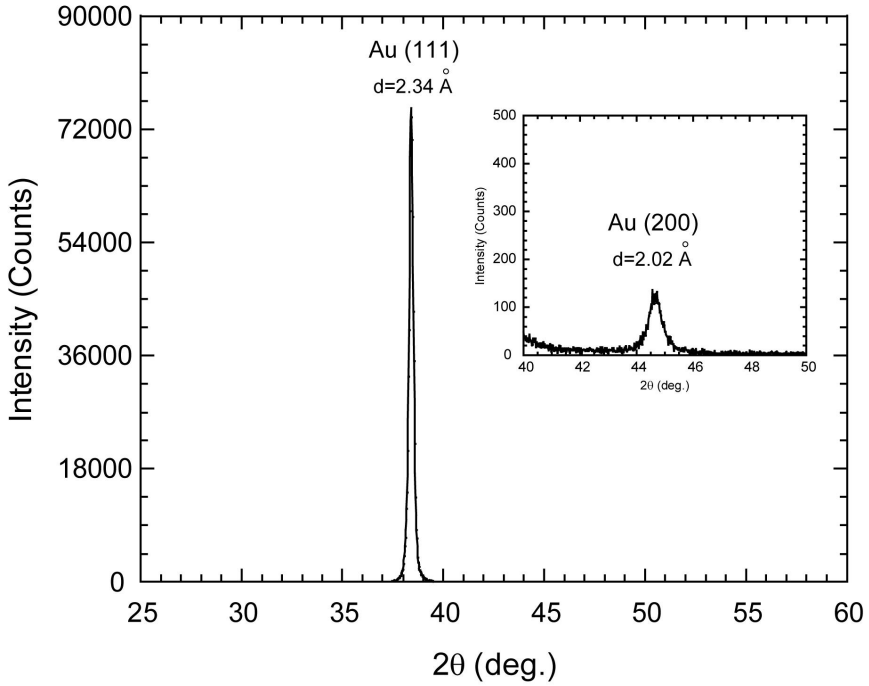

Figure 4.12: XRD measurement of Au-0.7 at. % Ti film.

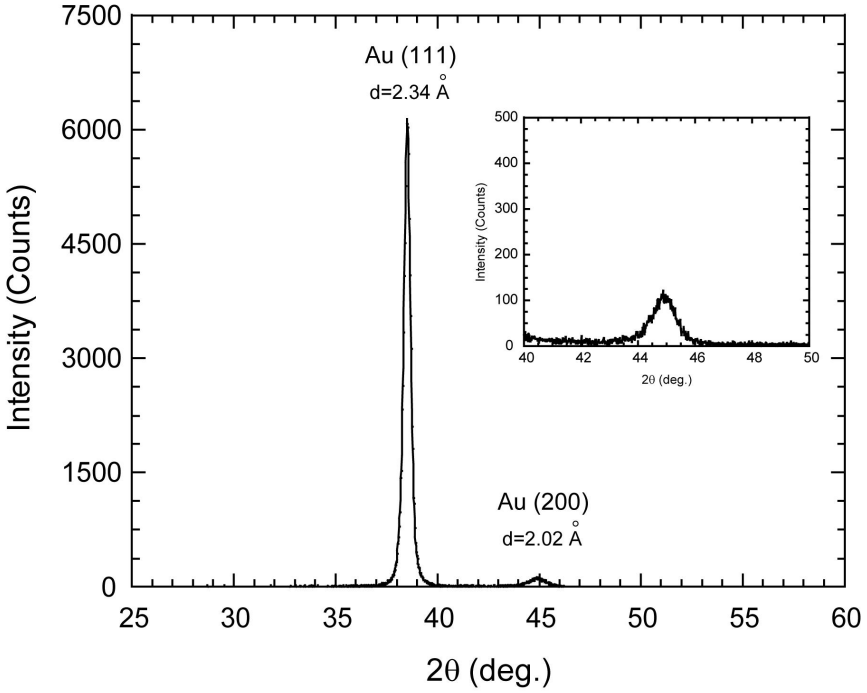

Figure 4.13: XRD measurement of Au-5.6 at. % Ti film.

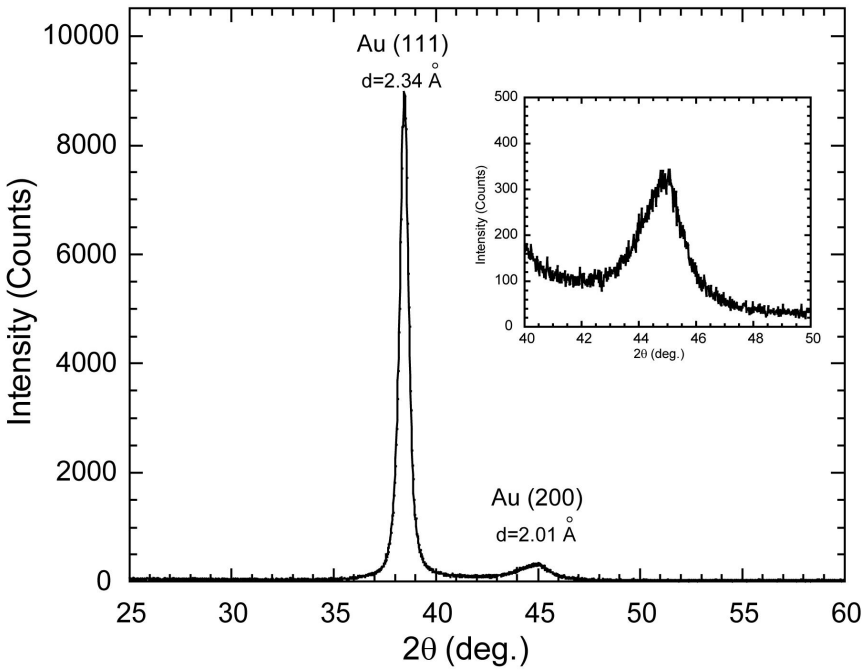

Figure 4.14: XRD measurement of Au-16.4 at. % Ti film.

well.

As seen in Figure 4.16, the intensity ratio of Au(111) to Au(200) decreases as the Ti amount

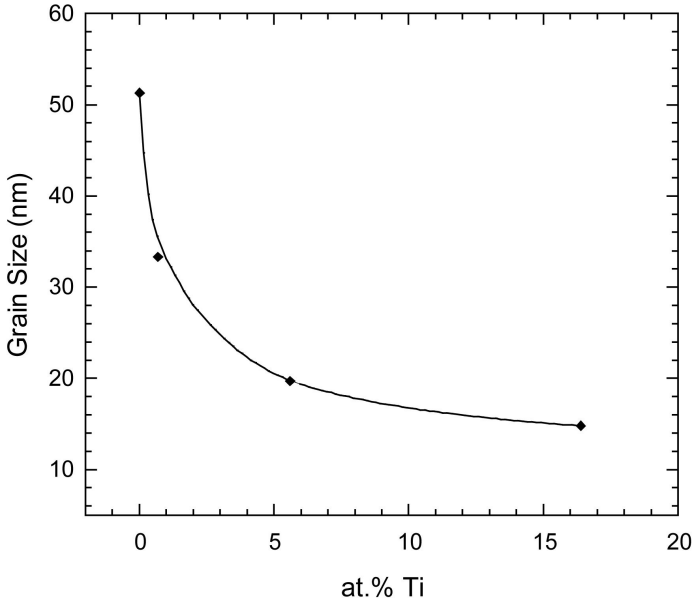

Figure 4.15: Grain size reduction with increasing Ti amount. The grain size was measured by XRD peak broadening. The uncertainty is on the order of 0.1 nm.

increases. Au thin films and other FCC metals are found to deposit preferentially in the (111) orientation [97]. It was also reported that the (111) orientation has the highest residual tensile stress [97]. However, the preferred orientation may be neglected if the strains are released, i.e., if the films are modified by heat treatment [97]. Extended modifications of the film may also introduce a residual compressive stress and invert the orientation to another preferred orientation, i.e., (200). While the shift in orientation was previously reported when the deposition and heat treatment temperature was changed, Figure 4.16 suggests the addition of Ti also increased the residual compressive stress and decrease in residual tensile stress within the film. The increase in residual compressive stress suggests the interaction of Au and Ti. Numerous reports on the interdiffusion of Au and Ti suggested an increase in solid solution and compound formation by the addition of Ti [53, 109]. Solid solution commonly reduces the lattice parameters (causing lattice strain) [116], which is consistent with the observed peak broadening in Figures 4.11 - 4.14. The decrease in lattice parameters could result in reduction in residual tensile stress in the film. It could also generate a volume reduction, resulting in surface cracks [1].

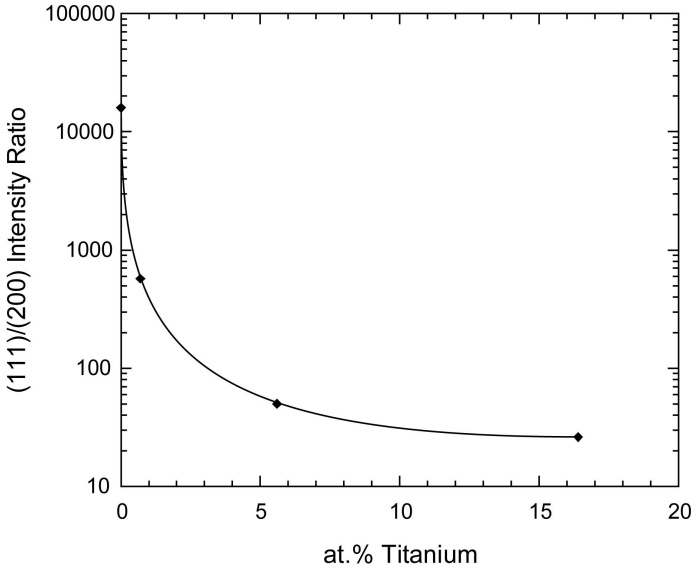

Figure 4.16: Intensity ratio of Au(111)/Au(200) as a function of Ti addition.

4.3.4 Mechanical Properties

The hardness and reduced elastic modulus of the co-evaporated Au-Ti films were obtained using nanoindentation with contact depths from about 20 times the surface roughness Ra, to about 20 % of the film thickness (Figures 4.17 and 4.18). A 125 % increase in hardness over pure Au was observed, from about 1.6 GPa to 3.6 GPa in the co-deposited Au-19.8 at. % Ti films at a contact depth h_c of 50 nm (Figure 4.17). Assuming a Poisson's ratio of about 0.33 for Au-19.8 at. % Ti [61], the calculated elastic modulus is within 2 % of the obtained reduced modulus, which is higher than the corresponding elastic modulus of cast Au-20 at. % Ti (106 GPa) reported by Kikuchi et. al. (Figure 4.19) [61]. The elastic modulus of sputtered Au-50 at. % Ti thin films was reported by Rodmacq et. al. to be about 115 ± 15 GPa, which is in the range of the obtained values [62].

A plausible explanation for the increase in hardness in the Au-Ti alloy films with Ti percentages higher than 16 at. % Ti may be given as follows. If Au and Ti did not form Au_4Ti and co-evaporated as separate elements, dispersion hardening can be proposed as a hardening mechanism [16]. According to this system, the hardness and elastic modulus can be written in terms of the rule of mixtures (ROM) equations as given in Equations 4.1 and 4.2,

$$H_{Au-Ti} = f_{Au}H_{Au} + f_{Ti}H_{Ti} \tag{4.1}$$

$$E_{Au-Ti} = f_{Au}E_{Au} + f_{Ti}E_{Ti} \tag{4.2}$$

where H and E are the hardness and elastic modulus, respectively, and f is the volume fraction.

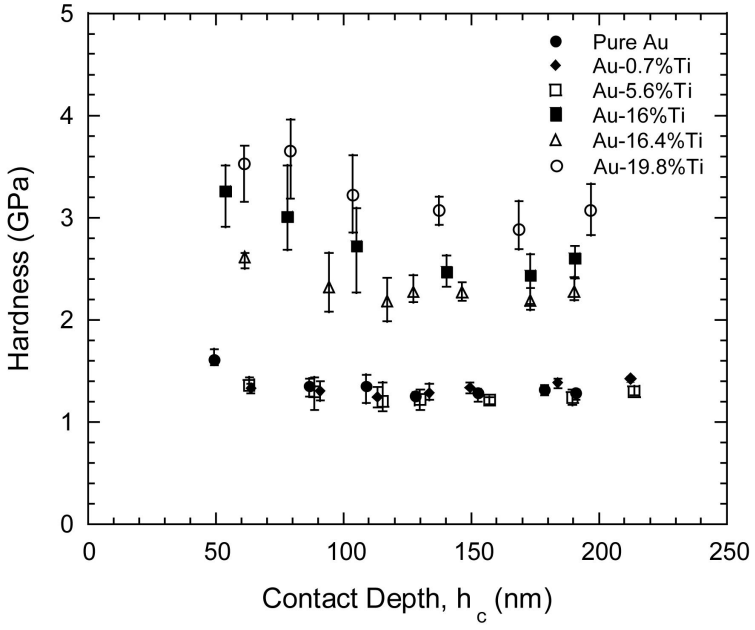

Figure 4.17: Effect of co-evaporation of Au-Ti on hardness.

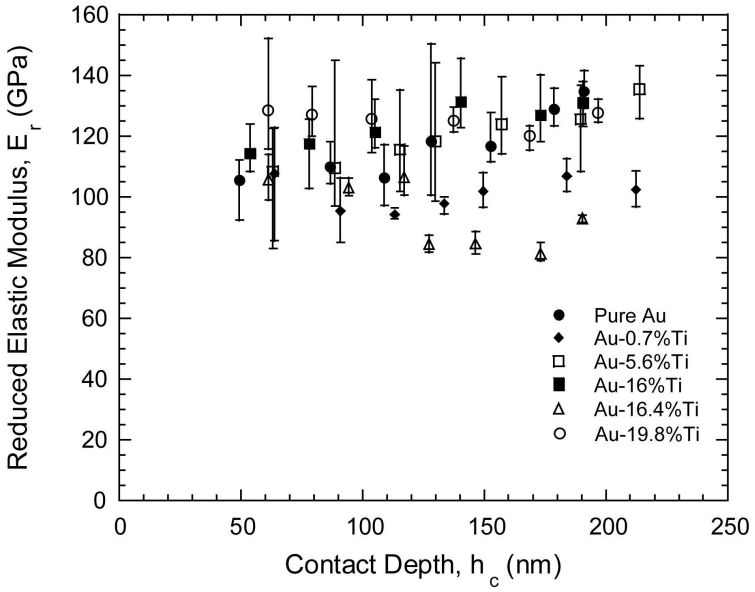

Figure 4.18: Effect of co-evaporation of Au-Ti on reduced elastic modulus.

Taking the elastic modulus and hardness of a pure Ti thin film to be about 116 GPa and 8 GPa, respectively [117], the ROM values for the hardness and elastic modulus of the Au-Ti films were calculated as shown in Figure 4.19 [16]. The elastic modulus and hardness of a pure Au thin film were estimated to be about 100 GPa and 1.5 GPa, respectively, in the ROM calculations.

The film's response under the same loading condition could follow an iso-stress (Reuss) or an iso-strain (Voigt) model [118]. Accordingly, the hardness and elasticity of the films could follow the aformentioned models, in which the iso-strain and iso-stress conditions represent the upper and lower bounds, respectively. The plotted values of ROM are the upper bound, from the iso-strain model (Voigt). Figure 4.19 shows no effect of Ti on the hardness of the Au-Ti films up to 5.6 at. % Ti. According to the phase diagram in Figure 4.10, 11 at. % Ti is fully soluble in Au above 1120°C (the evaporation temperature). The Au-Ti alloys have weak solid solution strengthening, as the product of the atomic weight ratio and the relative difference in atomic radii between Au and Ti is small [37]. While several reports have shown an increase in hardness from a small amount of Ti (less than 6 at. % Ti) [37, 38, 119] due to grain refining of Au [37, 58], the observed downsizing of the nodules and reduction in grain size in the co-evaporated Au-Ti films of less than 5.6 at. % Ti in the present study (Figure 4.15) did not result in an increase the hardness of the Au-Ti films.

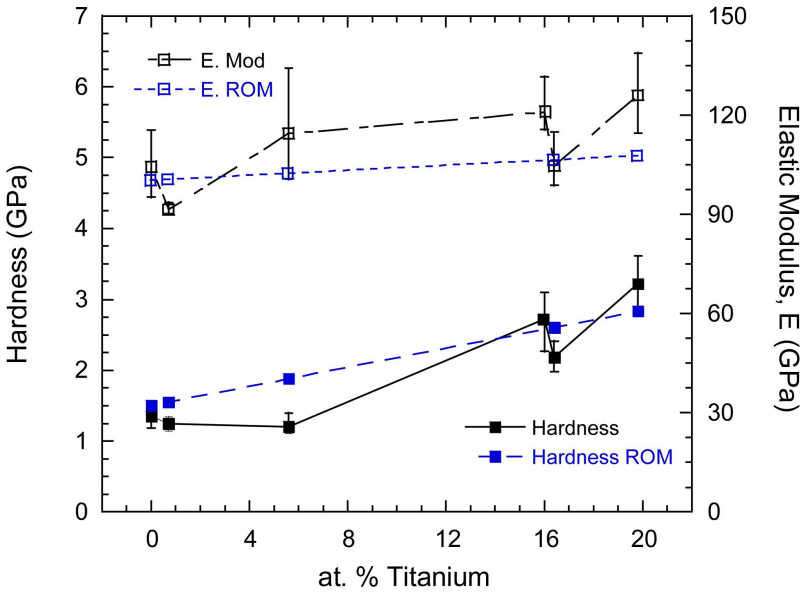

Figure 4.19: Effect of Ti concentration on the hardness and elastic modulus. The data shown in the graph was obtained at h_c of 100 nm.

For nanoindentation, if the material is considered to respond more closely to the iso-stress (Reuss) model (the lower bound of the ROM) [118], hardness and elastic modulus values obtained in the present study at or above the upper bound of the ROM, would indicate that other hardening mechanism(s) were involved, i.e., that the increased hardness was not simply due to the addition of Ti to Au and as a result of dispersion hardening of particles. The increase in elastic modulus and hardness measured for films at and above 16 at. % Ti suggests an increase in the amount and size

of the hard intermetallic compound precipitates.

To further investigate the possible formation of Au_4Ti, Mott and Nabarro strengthening, resulting from the lattice strain, was calculated [120]. The strengthening mechanism was reported to be the result of lattice mismatch between the particles (Au_4Ti precipitates) and the matrix (Au) [120], and its effect is given by Eqn. 4.3,

$$\Delta\sigma \approx 2G\epsilon f \tag{4.3}$$

where $\Delta\sigma$ is the increase in yield stress, G is the bulk modulus, ϵ is the strain field, and f is the volume fraction of the dispersed phase [16].

The assumption is made that the yield stress is approximately 1/3 of the hardness according to Tabor [121] and that the bulk modulus is related to the elastic modulus by the Eqn. 4.4.

$$G = \frac{E}{2(1+\nu)} \tag{4.4}$$

where ν is the Poisson's ratio of Au-Ti (≈ 0.33 [61]).

The product of lattice strain and volume fraction of the precipitates was then calculated and plotted in Figure 4.20.

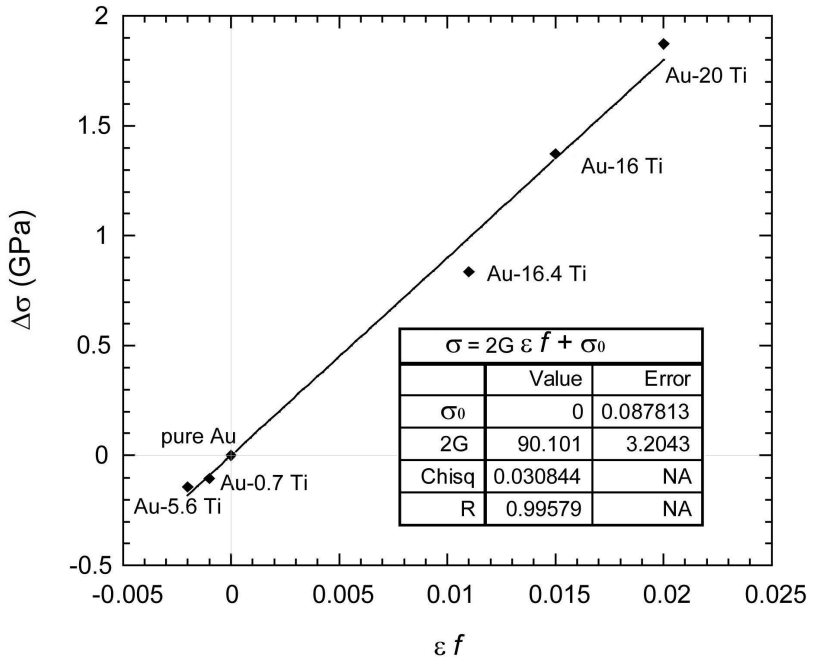

Figure 4.20: Lattice strain strengthening of Au-Ti alloys

As shown in Figure 4.20, ϵf is a linear function of yield stress, as expected. Since f is a positive number, its effect is solely on the slope of the line and not on the signs of the obtained values.

The direction of the lattice strain calculated from the present study could suggest the formation of the different phase structures by the addition of Ti content. As the Ti content increased within the solid solution region of less than 10.5 at. % Ti, the lattice strain became increasingly negative. The negative effect in the lattice strain suggests the reduction in lattice parameters. As it has been reported that the reduction in lattice parameters suggests solid solutioning [42, 116] and consistent to the Au-Ti films of 0.7 and 5.6 at. % Ti, solid solutioning could have developed which reduced the lattice parameters. The increase in the lattice strain, by increasing the Ti amount from 16 at. % Ti to 20 at. % Ti, suggests the increase in the precipitation of the intermetallic compound within the matrix, as described in Sec. 2.1.2.

4.3.5 Electrical Properties

The resistivity of the Au-Ti films are given in Table 4.1 and Figure 4.21. Resistivity increased as the amount of Ti increased. The resistivity of Au-0.22 at. % Ti and Au-1.06 at. % Ti alloys was reported in the literature to be about 2.66 $\mu\Omega$-cm and 12.94 $\mu\Omega$-cm, respectively [122]. From a linear interpolation of the two reported values [123], a resistivity of about 8.56 $\mu\Omega$-cm was expected, which is less than the obtained value of 11.6 $\mu\Omega$-cm for Au-0.7 at. % Ti (Figure 4.21). Also, according to Hahlbohm, an increase in resistivity for Au-Ti alloys was measured to be about 12.9 $\mu\Omega$-cm per at. % Ti [123], which is consistent with the values obtained from the present study shown in Figure 4.21.

The resistivity of bulk pure Ti is about 45 $\mu\Omega$-cm [124], as restated by Rodmacq et. al. [62], which is higher than resistivity of bulk pure Au (about 2.2 - 2.4 $\mu\Omega$-cm [62]) . The resistivity of Ti thin films was reported to be between 39 and 330 $\mu\Omega$-cm, varying based on film thickness and roughness [125]. Assuming the maximum reported resistivity of Ti ($\approx$ 330 $\mu\Omega$-cm), the ROM values for resistivity of the alloys were also calculated. The estimated resistivity measurements by the ROM were lower than the obtained values in the present study (Figure 4.21). It is feasible that difference between the ROM estimates and the measured resistivity is due to the formation of a solid solution and primarily intermetallic compound of Au_4Ti, which has different physical, chemical, and electrical characteristics than Au and Ti.

4.3.6 Investigation of Heat Treatment in Au-16.4 at. % Ti

Pietrokowsky [42] initially discovered the Au_4Ti phase by formation of striations in the grains, as this phase distinct characterizations in the metallographic studies. Pietrokowsky observed a change in the

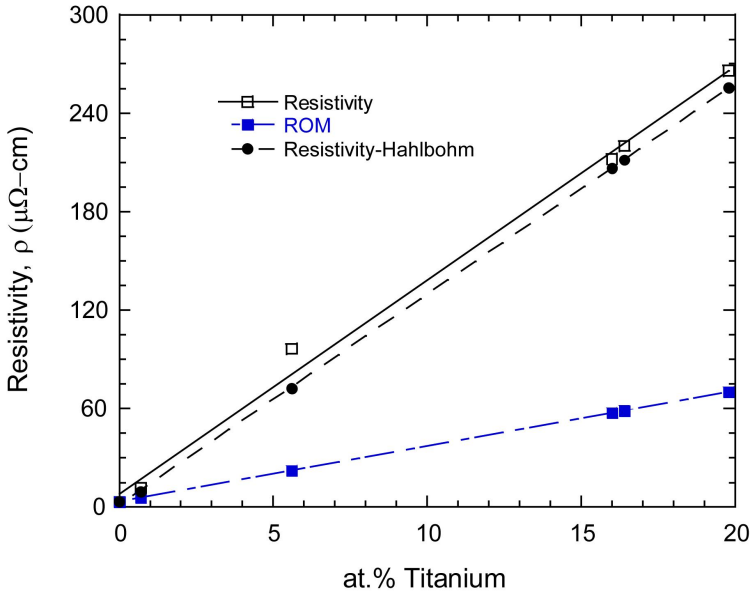

Figure 4.21: Linear increase in resistivity of the Au-Ti films compared to ROM predictions and values reported by Hahlbohm [123].

microstructure with temperature (from 1000°C to 1140°C) in Au-20 at. % Ti. The alloy displayed polyhedral grains after the heat treatment at 1000°C which changed to a rounded appearance by heat treating to 1140°C. Whereas no metallographic similarities were observed from what was previously reported in the literature and the co-evaporated Au-Ti films in the present study, the Au-16.4 at. % Ti was heat treated to increase the diffusion of Ti and Au. The heat treatment was performed for 24 hours at 500°C to increase the diffusion of Ti in Au and the subsequent interaction of the two metals. If the Au_4Ti did not form by co-evaporation, the heat treatment could possibly increase the driving force for development of this phase.

The Au-16.4 at. % Ti film was heat treated for about 24 hours at 500°C and cooled at room temperature. Considering the cooling rate of co-evaporated films is extraordinarily high, the Au and Ti could have deposited without interaction as separate elements. However, several papers have reported the interdiffusivity of sequentially deposited layers of Au and Ti at room temperature [51, 126]. Nevertheless, heat treating the films could increase the diffusion of Ti and Au and subsequently, the two elements would recrystalize to form Au_4Ti. The heat treatment altered the microstructures as shown in Figure 4.22. The change in microstructure is similar to the equilibrium phase in the system. The equilibrium phase in binary alloys could be obtained by over-aging the specimen, as described in Sec. 2.1.2. The over-aging leads to non-coherency of the precipitates and a decline in hardness. Van Heerden also demonstrated the non-coherency of Au-13 at. % Ti after 24 hrs at

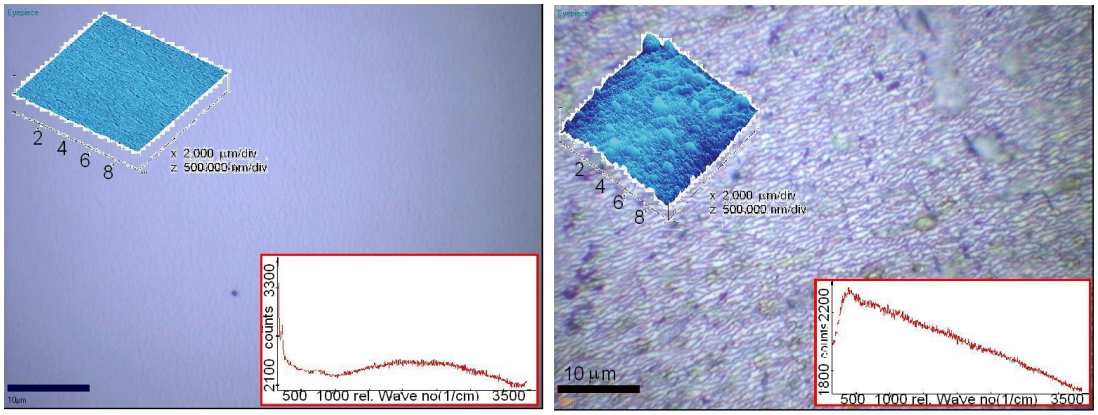

Figure 4.22: Optical, AFM images and Raman spectra of (1) as-deposited and (2) heat treated after 24 hrs of Au-16.4 at. % Ti.

500°C [60].

Raman scattering experiments were attempted to complement the structural characterization studies on the modified films. Whereas the Raman intensity peaks obtained on as-deposited and heat-treated Au-16.4 at. % Ti varied, no known peaks were observed in either films. The broad peak observed in the as-deposited Au-Ti film could be due to luminescence of Au-Ti. Meanwhile, the broad peak changed to a slide-like peak by heat treatment, which is currently unclear.

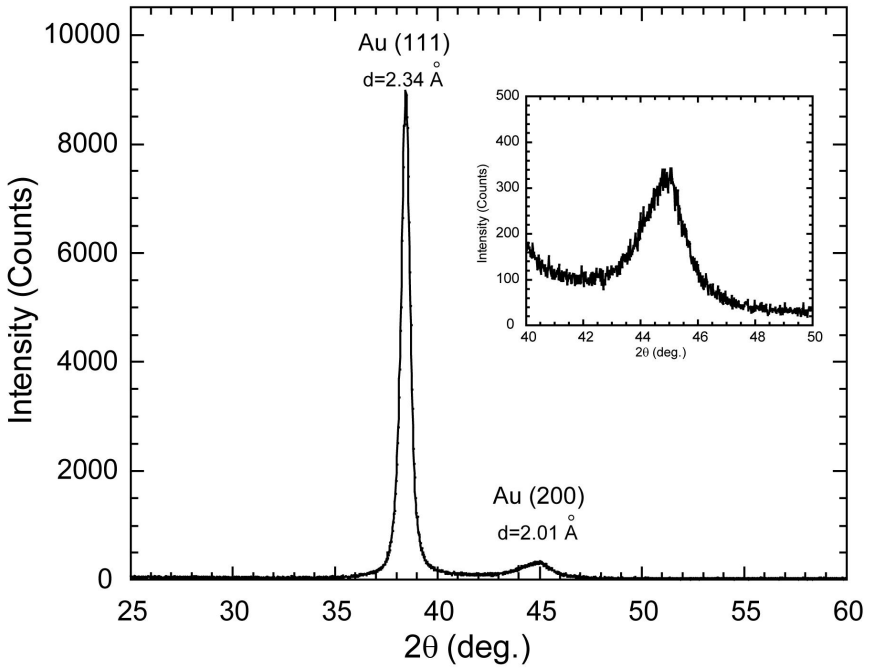

Figure 4.23: XRD spectra of the as deposited Au-16.4 at. % Ti film.

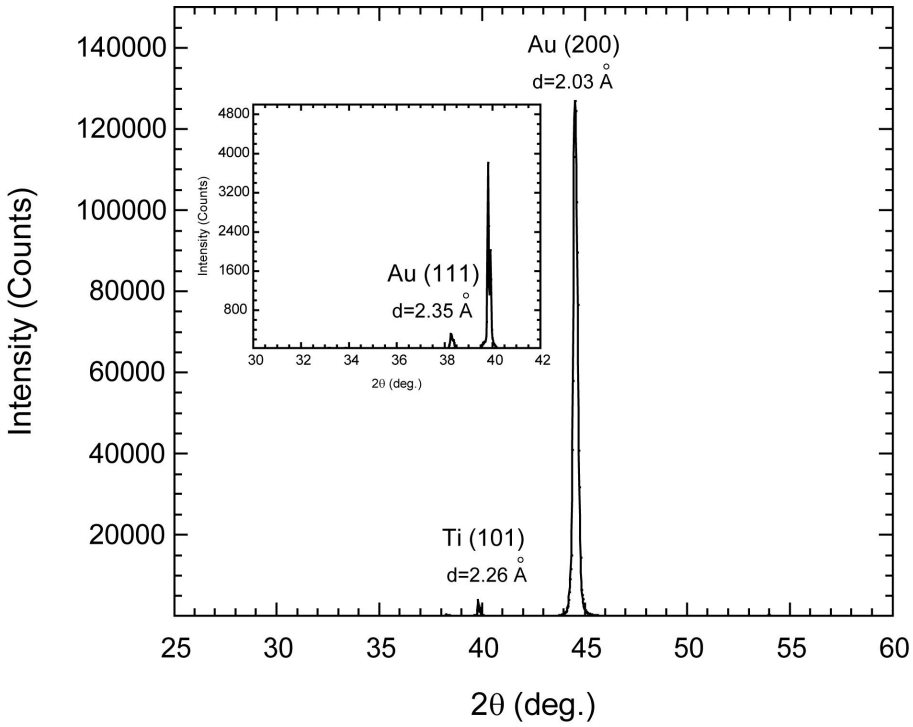

Figure 4.24: XRD spectra of the heat treated Au-16.4 at. % Ti film.

X-Ray diffraction measurements, shown in Figures 4.23 and 4.24, were obtained on the as-deposited and heat treated Au-16.4 at. % Ti films. As previously noted, the preferred (111) orientation of the as-deposited Au-Ti, suggesting a high residual tensile stress, shifted to the preferred (200) orientation, suggesting the presence of a residual compressive stress as the film was heat treated [97]. The change was accompanied by the appearance of a new peak at 39.9° which closely matched the (101) Ti peak. The development of the Ti peak signified Ti recrystalization after the progression of heat treatment.

The grain size measurements also indicated an increase in grain size by heat treatment, from about 15 nm (as-deposited Au-16.4 at. % Ti) to 37 nm (heat-treated Au-16.4 at. % Ti). Accordingly, the increase in grain size by heat treatment is consistent with the decrease in hardness. However, due to the uncertainty of the measured hardness, resulting from the large surface roughness of the heat-treated film (Ra $\approx$ 60 nm over a 1 μm^2 scan area) and pop-in from the oxide layer, the values are not presented.

4.4 Investigation of Precipitate Hardening on Au-5.6 at. % Ti Films

The negligible effect of Ti, at concentrations less than 5.6 at. %, on the hardness of Au could be increased through proper heat treatment [57–59]. Graham demonstrated an increase in hardness of Au-4 at. % Ti by a change in the microstructure through age hardening [57]. TEM images of Au-Ti alloys indicated that the maximum hardness in the age-hardened films coincided with the coherent precipitation of Au_4Ti in the super saturated matrix [57]. The Au_4Ti precipitates were found to coarsen with over-aging, causing the reduction in hardness. Based on the TEM measurements, Van Heerden reported the coherent precipitation of Au_4Ti by rapidly solidifying Au-7.5 at. % Ti and Au-11 at. % Ti [60].

In the present study, strengthening of the Au-Ti alloy films by age hardening was attempted according to the heat treatment specified in the previous chapters (chapter 2 and 3). Although the results of the present study and the reported literature suggests the diffusion of Au and Ti at room temperature and resulting in an increase in precipitation of Au_4Ti, heat treatment could increase the diffusion rate and subsequently the precipitation of the Au_4Ti. The precipitate strengthening (age hardening) effect of Au-5.6 at. % Ti films in the present study was compared to Au-6.3 at. % Ti (1.6 wt. %) cast alloy [58].

The evolution of surface topography with increasing heat treatment period, showed a trend in refinement of grains on the surface. Figure 4.25 shows optical microscopy images as well as AFM images. A similar trend was observed in the first trial as given in Appendix B. Grain growth can be seen in some of the Au-Ti films after heat treatment. Grain boundaries can be observed with the naked eye, which could be the result of the films being thermally etched. Surface roughnesses of the age hardened films were averaged from 3 AFM scans conducted over a 1 μm^2 area and are tabulated in Table 4.2. The evolution of the surface roughness with heat treatment time is not clearly understood.

The cuboidal microstructure observed in Figure 4.25(3) suggests precipitation of a transition phase, ω [42, 127]. In an alloy with high lattice mismatch, the ω's cuboidal structure reduces the elastic strain within the matrix. Similar formations were previously observed in solution treated Ti-Fe binary alloys, after quenching and subsequent aging [127]. However, formation of ω was previously observed at the nanometer scale using TEM despite the micrometer scale in the images obtained in Figure 4.26.

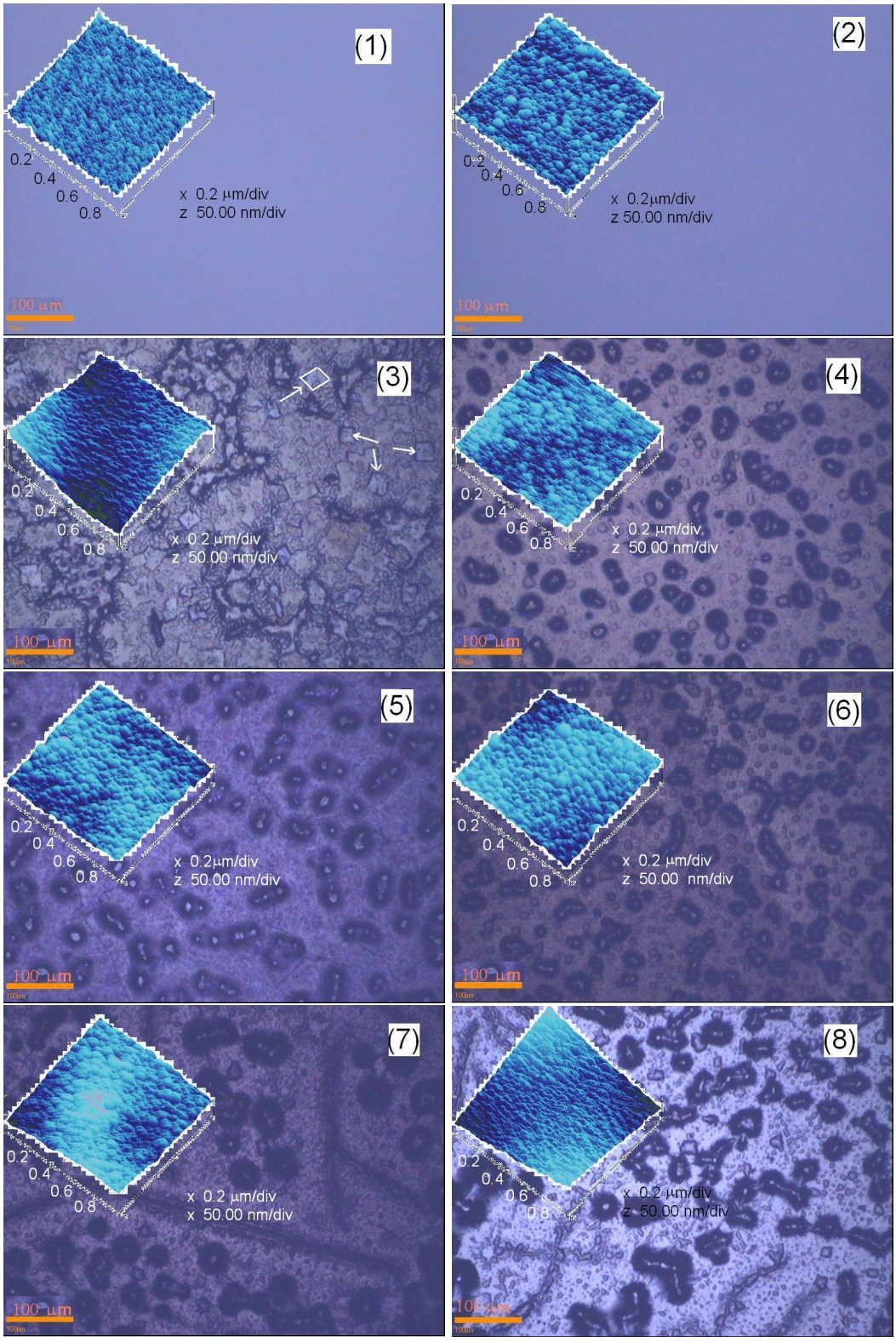

Figure 4.25: Optical and AFM images of Au-5.6 at. % Ti Aged at 550°C after (1) 1 min (2) 5 min (3) 10 min (4) 30 min (5) 60 min (6) 100 min (7) 600 min (8) 1000 min heat treatment followed by slow cooling.

Table 4.2: Surface roughness of age hardened Au-5.6 at. % Ti films

Heat treatment	Trial 1	Trial 2
Period (min)	Ra (nm)	Ra (nm)
0 min	1.9	1.9
1 min	2.0	2.8
5 min	2.5	2.8
10 min	6.8	8.8
30 min	4.0	3.0
60 min	2.70	3.9
100 min	4.0	4.5
600 min	3.3	7.4
1000 min	3.3	8.3

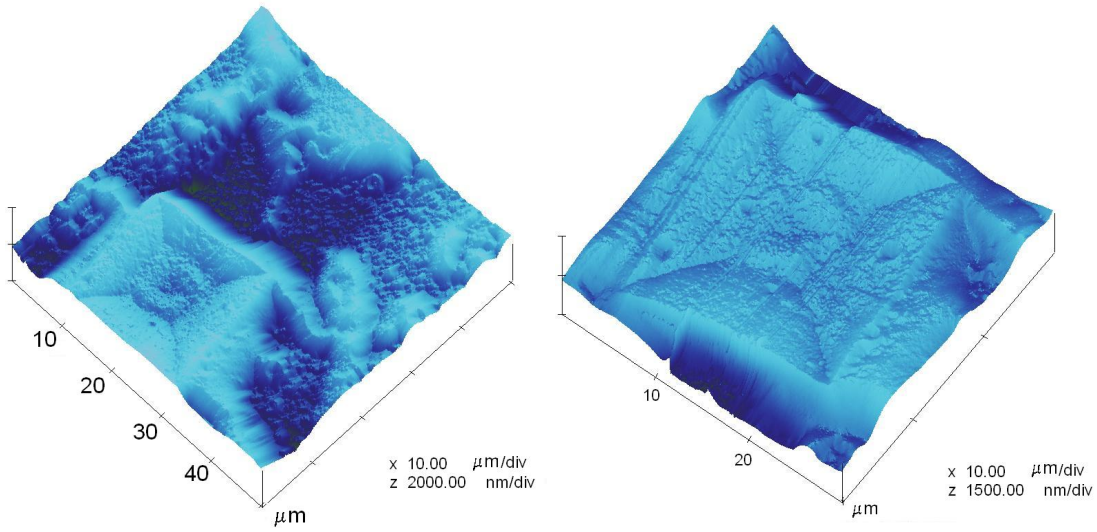

Figure 4.26: AFM images showing the cuboidal phase on the 10 min aged Au-5.6 at. % Ti film.

Formation of α (HCP) or β (BCC) Ti is dependent upon cooling rate and processing procedure [55]. In Ti alloys, β-Ti can be retained at room temperature with a proper cooling rate due to sufficient β stabilizer elements. The metastable β phase can be hardenable if α particles precipitate with the appropriate heat treatment [55]. While "rich" β-Ti (Figure 4.27) is stable enough that it does not undergo a transition of the ω phase, the "lean" β-Ti produces a metastable phase during

cooling or aging.

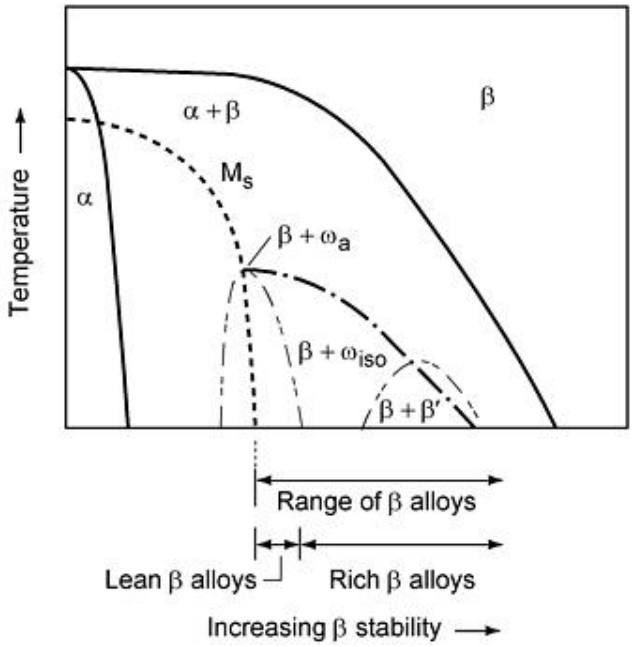

Figure 4.27: Phase diagram of α and β Ti [55]

Raman spectroscopy was performed on aged Au-6 at. % Ti in an attempt to identify the precipitates observed on the surface. Figure 4.28 is a magnification of Figure 4.25(6). The magnified image is representative of what was seen in a majority of other aged Au-5.6 at. % Ti films and shows clusters of black globules. The inset image in Figure 4.28 shows an integrated intensity map of the Raman spectrum for the boxed region. As shown in Figure 4.29, the bright regions correspond to a broadband signal that has not been identified and the dark regions correspond to the Raman spectrum of bulk crystalline Si [128].

spectra from locations within the black regions in Figure 4.29 show that the 520 cm^{-1} Si peak shifted to approximately 517 cm^{-1}. The negative shift suggests an increase in tensile stress within the film [129]. The formation of Si clusters on the surface of the Au-Ti alloy film after heat treatment suggests the Si substrate diffused through the 1 μm Au film.

Figure 4.30 shows the optical image of an age hardened film after 100 min. The linear-shaped ridge shown in Figure 4.30(2) is a magnification of the acicular (needle-like) structures of Figure 4.25(7, 8). The acicular structures are seen in all films. However, the aggregation of the precipitates are only notable in the films heat treated beyond 100 min. Two dimensional and three dimensional AFM images of the film show deep, sharp voids over the surface. It also shows the black acicular and globular precipitates formed on the surface in Figures 4.25 (4 - 8). Figure 4.30(3) shows the Raman

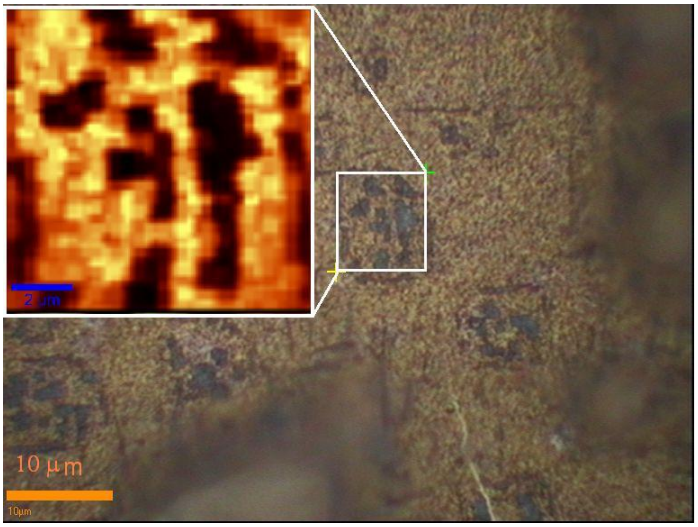

Figure 4.28: Optical image and Raman intensity map of Au-5.6 at. % Ti film aged for 100 min.

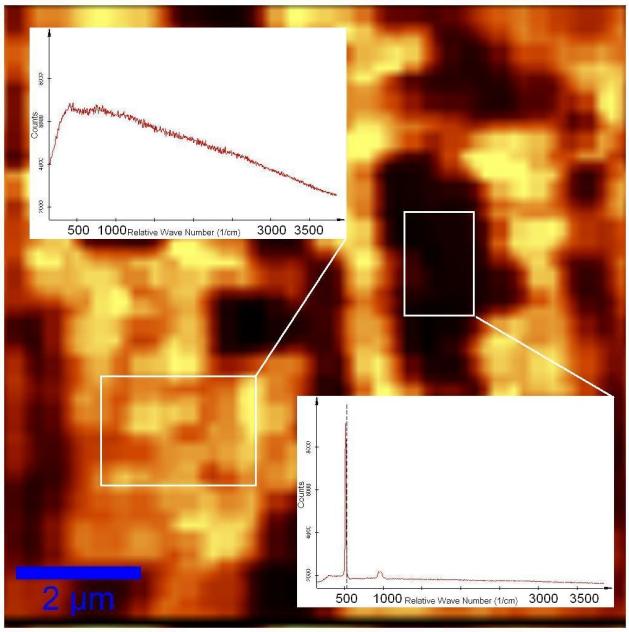

Figure 4.29: Raman map and spectroscopy of aged Au-5.6 at. % Ti. The bottom spectrum with multiple peaks shows bulk crystalline Si while the broad peak on the top spectrum is unknown. The boxed regions are not drawn to the scale.

intensity map of the 520 cm^{-1} crystalline Si peak over the same region. The bright regions show an intense crystalline Si peak near 520 cm^{-1}. The agglomeration of Si particles in groups is consistent with the congregation of acicular and globular precipitates observed in the optical images.

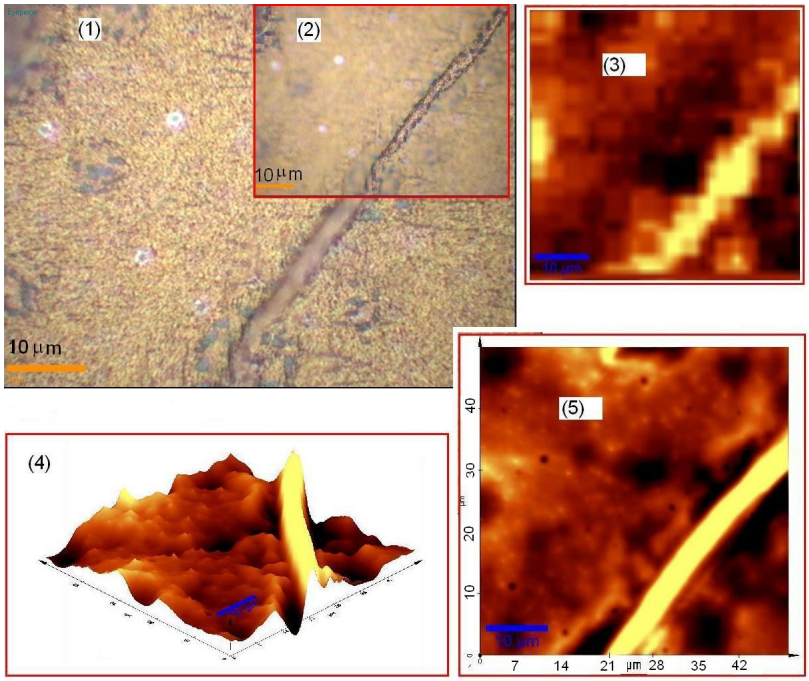

Figure 4.30: (1) Focused optical image, (2) over-focused optical image, (3) Raman crystalline Si map, (4) 3D AFM, and (4) 2D AFM image of Au-5.6 at. % Ti.

Nanoindentation results for age hardened Au-5.6 at. % Ti films show an increase in hardness compared with the as-received films. Figure 4.31 shows the average two trials performed on age hardened Au-5.6 at. % Ti films. Despite slight differences in the two age hardening trials of Au-5.6 at. % Ti, the hardness was repeatable. Although a similar trend was observed Kim et. al [58], due to existence of Si crystalline particles on the surface, precipitate hardening perhaps is not the principal hardening mechanism in the present system. The 83 % increase in hardness (from 1.2 to 2.7 GPa) by heat treating was obtained not only by precipitate hardening, but also by dispersion hardening as a result of diffusion of the Si substrate to the surface. The reported increase in hardness in Au-6.3 at. % Ti after the 100 min heat treatment by Kim et. al. was about 300 % (final hardness $\approx$ 1.96 GPa $H_V \approx$ 2.1 GPa H_N) [58].

The precipitate hardening of Au-Ti thin films could have occurred during the initial 10 min of the heat treatment. According to Figures 4.25 and 4.31, the hardness increased without changes in the surface topography for the first 5 min. However, the change in surface topography at 10 min is consistent with the large error bars in hardness measurements, suggesting the presence of other compounds or hardening mechanisms. To confirm the precipitate strengthening of Au-Ti before 10 min, further experiments are required within the first 10 min. aging time period. However, the

noticeable increase in hardness of the Au-Ti alloy films after 5 min. period of heat treatment was observed in the present study, was consistent to the previous report in the literature [59].

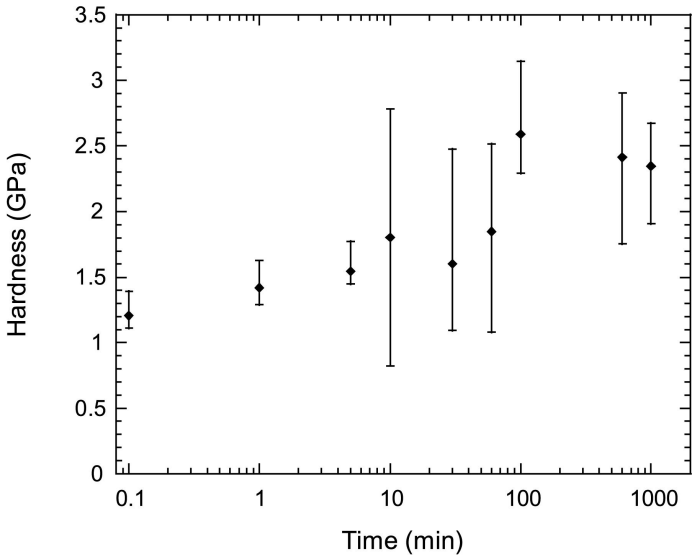

Figure 4.31: Change in hardness at contact depth of 100 nm, as the Au-5.6 at. % Ti aged at 550°C. The specimen with 0.1 min. heat treatment represents the as-deposited specimen.

"Pop-in" (displacement burst) was seen during the nanoindentation of heat treated Au-5.6 at. % Ti films (Figure 4.32), while the as-received films did not exhibit such behavior. Pop-in could be a result of indenter penetration into TiO_2 formed during heat treating in air [126]. The pop-in behavior of nanoindentation experiments after heat treatment in air suggests that the heat treatment should be carried out in vacuum to avoid growth of an oxide layer, and thus a change in surface topography.

The resistivity of these films has not been measured since the Au-Ti films were too small. However, Ashewell et. al. [126] reported an increase in resistivity of $Au/Ti/SiO_2$ thin films by increasing heat treatment period. The resistivity maximized, and finally decreased as heat treatment continued. An increase in resistivity of Au-Ti films as the temperature increases was also investigated by Hahlbohm [123].

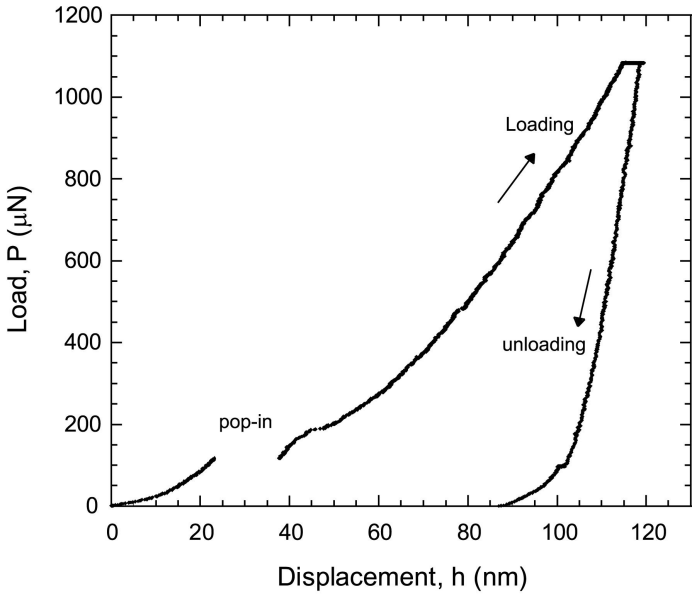

Figure 4.32: Load versus depth curve showing the pop-in during nanoindentation

Chapter 5

Conclusions and Future Work

5.1 Conclusions

Determination and control of the mechanical properties in micro electro mechanical systems (MEMS) is of critical importance for subsequent performance, reliability, and a long term stability of these systems. Motivated by the goal to create MEMS electrical contacts, systematic studies of Au thin films was performed. Due to fretting wear and failure in performance of pure Au, the films were modified in an attempt to improve the mechanical properties. One modification was performed by deposition of a thin near surface layer of Mo on Au. The modification was intended to inhibit Au-Au bonding in cyclic loading of surfaces by the presence of immiscible Mo. The second modification was performed by co-evaporation of Au and Ti. This modification was designed to increase the strength and hardness of Au by coherent formation of a surface alloy. The modified films were investigated by the change in mechanical and electrical properties to understand how the nanoscale surface and subsurface material structure affects the properties.

1. Investigation of the effect of change in deposition rate on Au thin films showed a small change in mechanical and electrical properties. At the lowest deposition rate, 1.5 Å/s, the hardness increased by about 14 % (1.05 - 1.2 GPa). The surface roughness of the Au films was nearly identical as the deposition rate was varied.

2. The effect of the Ti and Cr adhesion layers and heat treatment of Au films on the mechanical properties has also been investigated. A 20 nm Cr or Ti film was deposited prior to e-beam evaporation of the 700 nm thick Au film. The films were heat treated at 100°C in N_2 for one hour. The difference in surface roughness (Ra) resulting from heat treatment and change in

adhesion layer of Au films was found to be negligible. However, AFM images of the surface topography of the heat treated Au films with a Cr adhesion layer indicated grain boundary-like cracks. The adhesion layer and the heat treatment were found to have a negligible effect on the mechanical properties of the Au thin films.

3. A thin layer of Mo was deposited on Au in an attempt to improve the tribological performance of Au thin films by minimizing fretting wear. An immiscible near surface layer of Mo could prevent the Au-Au bonding in cyclic loading of electrical contacts. To investigate the change in mechanical properties and tribological performance of a thin Mo layer on Au, nanoindentation, microscratching and wear experiments were performed. A 92 % increase in hardness and an increase in the tribological performance were obtained by deposition of the 20 nm Mo film.

4. Co-deposited Au and Ti film with various concentrations were studied to investigate the change in mechanical and electrical properties. Au films with 0 - 19.8 at. % Ti showed a decrease in nodule size with increasing Ti concentration. These films also showed cracks at 16 at. % Ti to 19.8 at. % Ti. X-ray diffraction analysis performed on the system indicated the presence of Au(111) and Au(200) peaks and an absence of Ti peaks. A report on a reduction in intensisty ratio of the two (111)/(200) suggested an increase in residual compressive stress which was consistent with the results obatained in the present study as the Ti amount increased. Peak broadening of the XRD measurements by addition of Ti also suggested a decrease in the grain size causing lattice strain within the film.

   Up to 5.6 at. % Ti, did not effect the hardness of the Au films, despite a reduction in grain size. This result was not consistent with the reported increase in hardness for Au-3 at. % Ti jewelry alloys by grain refinement. The negative lattice strain according to Mott and Nabarro also suggested the solid solution formation of co-evaporated Au-0.7 and 5.6 at. % Ti films. However, upon further addition of Ti, the hardness increased from 1.6 GPa (pure Au) to 3.6 GPa (Au-20 at. % Ti), suggesting an increase in the number and size of Au_4Ti precipitates in the Au-16 up to 19.8 at. % Ti films. Overall, the reduced elastic modulus was found to increase by the addition of Ti. An increase in resistivity was observed as the Ti concentration was increased. The increaes in resistivity which was supported by previous reports in the literature in Au-Ti alloys also suggests the interaction of Ti and Au and formation of the intermetalic Au_4Ti phase which effects the resistivity of Au and Ti. The increase in resistivity also suggested that Au_4Ti has a higher resistivity than Ti (more than 330 $\mu\Omega$-cm) as the measured resistivity was higher than ROM values.

Whereas Ti could presumably be deposited as a separate element without any interaction with Au due to the deposition technique used in the present study, an increase in diffusion of Au and Ti was examined by heat treating the Au-16.4 at. % Ti film at 550°C for 24 hours. While the surface topography of the film changed, the XRD measurements indicated the change in orientation of the deposited Au crystal structure from the (111) to the (200) plane, suggesting an increase in residual compressive stress.

The effect of precipitate hardening (age hardening) on the Au-5.6 at. % Ti films was studied by heat treating the films for different time periods. The Au-Ti film exhibited an increase in hardness through the progression of heat treatment. However, due to the detection of bulk Si crystalline peaks on the surface of the heat-treated films in the Raman studies, precipitate hardening of Au_4Ti may not be the only hardening mechanism involved. This increase may have also been influenced by the dispersion hardening of Si within the Au-Ti matrix.

As a result of a parallel study of co-evaporated Au-Ti with co-evaporated Au-Si films [130], a metastable phase of Au-Si films were observed which disappeared over time suggesting the diffusion of Au and Si at room temperature. Therefore, interdiffusion of co-evaporated Au-Ti films is also expected, and as a result an increase in precipitation of Au_4Ti at room temperature. The result suggests that co-evaporation of Au-Ti thin films resulted in films with different properties than for a cast alloy with the same composition. It also suggests that co-evaporation results in a thin film with mechanical properties which change with time and temperature.

5.2 Future Work

- Identification of Au_4Ti

  In order to clarify the formation of Au_4Ti by co-evaporation, high resolution TEM (HRTEM) could prove useful. The identification of this phase was previously attempted by XRD, Raman, electrical resistivity, and chemical etching, however, no direct evidence of the formation of compound was observed. Calculation of the lattice parameters using HRTEM could verify the formation of an intermetallic compound.

- Heat treatment of Au-5.6 at. % Ti in vacuum

  Interdiffusion of Au-Ti and the change in microstructure by heat treatment was investigated by Poate et. al. [51]. It was found that heat treatment in air oxidizes the Ti in Au-Ti alloys and could possibly increase the resistivity. The increase in mechanical properties and the effect of

age hardening for Au-Ti films with less than 10.5 at. % Ti could be investigated by performing heat treatment in vacuum or N_2, which could reduce or eliminate the interaction of Ti with O_2.

- Au Contact Tester

  A pair of planar parallel contact surfaces designed and fabricated by MIT as a MEMS based contact tester could be investigated by study of the evolution in surface topography after cyclic loadings. A thin conductive Au film was patterned on Si(100) substrate in a Kelvin configuration, as shown in Figure 5.1. The compliant membrane was developed by anisotropic etching of Si. The two-piece tester enables the inspection of the progression of surface topography before, during, and after the establishment of contact between the two surfaces. The quasi-kinematic coupling provides the initial gap between the contact with the capability of being loaded repeatedly utilizing the nanoindenter available at OSU.

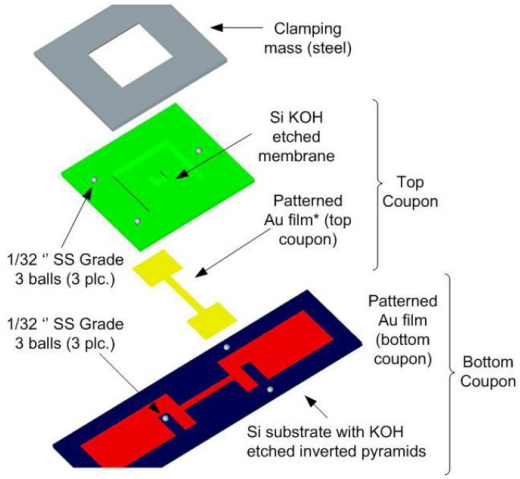

Figure 5.1: Spread out configuration of kinematic coupling from MIT. (Courtesy of MIT design)

The tester is designed to characterize the electrical properties (contact resistance), surface breakthrough, and mechanical properties of the contacts. By applying a known load, the surfaces are brought together into contact and the change in displacement versus force can be measured. The surfaces will undergo multiple contacts and the evolution of surface topography can be measured using AFM. The modified Au films, could then be deposited on the surfaces to determine the tribological performance of the films. While a majority of studies in the literature cover sphere on flat [2, 72, 73, 77, 131], sphere on sphere [76] and rod on flat contact [132], very

few studies exist which investigate flat on flat contact. The evolution of the contact surfaces in the initial stages of repetitive cycling would be the primary focus of the continuing study.

- Wear resistance properties of Au-Ti alloys could be further improved by ion-implantation of N. The change in wear behavior of Ti-6Al-4V and the improvement in wear resistance was reported to result from an increase in surface hardness [133, 134]. The increase in tribological performance of Ti-Cr films was also investigated by Wirz et. al. by incorporating N into these films and forming TiN [35]. The effect of ion-implantation of N in the Au-Ti films could also be investigated in future studies.

Bibliography

[1] D.C. Miller, C.F. Herrmann, H.J. Maier, S.M. George, C.R. Stoldt, and K. Gall. Intrinsic stress development and microstructure evolution of Au/Cr/Si multilayer thin films subject to annealing. *Scripta Materialia*, 52(9):873–879, 2005.

[2] S.T. Patton and J.S. Zabinski. Fundamental studies of Au contacts in MEMS RF switches. *Tribology Letters*, 18(2):215–230, 2004.

[3] C.M. Doelling, T.K. Vanderlick, J. Song, and D. Srolovitz. Nanospot welding and contact evolution during cycling of a model microswitch. *Journal of Applied Physics*, 101(12), 2007.

[4] P.A. Engel, E.Y. Hsue, and R.G. Bayer. Hardness, friction and wear of multiplated electrical contacts. *Wear*, 162-164:538–551, 1993.

[5] M. Martyniuk, J. Antoszewski, B.A. Walmsley, C.A. Musca, J.M. Dell, Jung Yeon-Gil, B.R. Lawn, Huang Han, and L. Faraone. Determination of mechanical properties of silicon nitride thin films using nanoindentation. volume 5798, pages 216–225, USA. SPIE-Int. Soc. Opt. Eng.

[6] R.A. Coutu, J.R. Reid, R. Cortez, R.E. Strawser, and P.E. Kladitis. Microswitches with sputtered Au, AuPd,Au-on-AuPt, and AuPtCu alloy electric contacts. *Components and Packaging Technologies, IEEE Transactions on*, 29(2):341–349, 2006.

[7] B.L. Pruitt, W.T. Park, and T.W. Kenny. Measurement system for low force and small displacement contacts. *Journal of Microelectromechanical Systems*, 13(2):220–229, 2004.

[8] R. Saha and W.D. Nix. Effects of the substrate on the determination of thin film mechanical properties by nanoindentation. *Acta Materialia*, 50(1):23–38, 2002.

[9] L. De Chiffre, H. Kunzmann, G.N. Peggs, and D.A. Lucca. Surfaces in precision engineering, microengineering and nanotechnology. *CIRP Annals - Manufacturing Technology*, 52(2):561–577, 2003.

[10] W.D. Nix and H. Gao. Indentation size effects in crystalline materials: A law for strain gradient plasticity. *Journal of the Mechanics and Physics of Solids*, 46(3):411–425, 1998.

[11] N.A. Fleck and J.W. Hutchinson. A phenomenological theory for strain gradient effects in plasticity. *Journal of the Mechanics and Physics of Solids*, 41(12):1825–1857, 1993.

[12] N.A. Fleck, G.M. Muller, M.F. Ashby, and J.W. Hutchinson. Strain gradient plasticity: Theory and experiment. *Acta Metallurgica et Materialia*, 42(2):475–487, 1994.

[13] Y. Cao, D.D. Nankivil, S. Allameh, and W.O. Soboyejo. Mechanical properties of Au films on silicon substrates. *Materials and Manufacturing Processes*, 22(2):187 – 194, 2007.

[14] M. Ohring. *The Materials Science of Thin Films*, volume 1. Academic Press Limited, San Diego, United Kingdom edition, 1992.

[15] P.H. Mayrhofer, C. Mitterer, L. Hultman, and H. Clemens. Microstructural design of hard coatings. *Progress in Materials Science*, 51(8):1032–1114, 2006.

[16] G.E. Dieter. *Mechanical Metallurgy*, volume 1 of *Material Science and Metallurgy*. McGraw-Hill, London, SI metric edition, 1928.

[17] B.L. Pruitt. *Piezoresistive Cantilevers For Characterizing Thin-Film Gold Electrical Contacts*. Dissertation, Stanford, 2002.

[18] M.J. Cordill, D.M. Hallman, N.R. Moody, D.P. Adams, and W.W. Gerberich. Thickness effects on the plasticity of gold films. *Metallurgical and Materials Transactions A-Physical Metallurgy and Materials Science*, 38A:2154–2159, 2007.

[19] M.M. Biener, J. Biener, R. Schalek, and C.M. Friend. Surface alloying of immiscible metals: Mo on Au(111) studied by STM. *Surface Science*, 594(1-3):221–230, 2005.

[20] S.Y. Quek, M.M. Biener, J. Biener, C.M. Friend, and E. Kaxiras. Tuning electronic properties of novel metal oxide nanocrystals using interface interactions: MoO_3 monolayers on Au(111). *Surface Science*, 577(2-3):L71–L77, 2005.

[21] Z. Song, T.H. Cai, J.A. Rodriguez, J. Hrbek, A.S.Y. Chan, and C.M. Friend. A novel growth mode of Mo on Au (111) from a Mo(CO)(6) precursor: An STM study. *Journal of Physical Chemistry B*, 107(4):1036–1043, 2003.

[22] S.C. Tung and Y.T. Cheng. Microstructures and tribological characteristics of electron-beam co-deposited Ag/Mo thin film coatings. *Wear*, 162:763–772, 1993.

[23] Z. Lee, C. Ophus, L.M. Fischer, N. Nelson-Fitzpatrick, K.L. Westra, S. Evoy, V. Radmilovic, U. Dahmen, and D. Mitlin. Metallic NEMS components fabricated from nanocomposite Al-Mo films. *Nanotechnology*, 17(12):3063–3070, 2006.

[24] J.R. Williams and D.R. Clarke. Strengthening gold thin films with zirconia nanoparticles for MEMS electrical contacts. *Acta Materialia*, 56(8):1813–1819, 2008.

[25] A.A. Voevodin, J.J. Hu, T.A. Fitz, and J.S. Zabinski. Tribological properties of adaptive nanocomposite coatings made of yttria stabilized zirconia and gold. *Surface & Coatings Technology*, 146:351–356, 2001.

[26] U. Buran, H.C. Mader, M. Morsbach, and B.A. Newman. Plasma-sprayed coatings for piston rings - state of development and application potential. In *ASM Int. Conference*, Surface Modification and Coatings, pages 8512–024, Toronto, Canada, 1985.

[27] K.B. Yoder, A.A. Elmustafa, J.C. Lin, R.A. Hoffman, and D.S. Stone. Activation analysis of deformation in evaporated molybdenum thin films. *Journal of Physics D-Applied Physics*, 36(7):884–895, 2003.

[28] T.C. Chou, T.G. Nieh, S.D. McAdams, G.M. Pharr, and W.C. Oliver. Mechanical-properties and microstructures of metal ceramic microlaminates .2. a Mo/Al_2O_3 system. *Journal of Materials Research*, 7(10):2774–2784, 1992.

[29] R.A. Higgins. *Engineering Metallurgy- Applied Physical Metallurgy.* Elsevier, 6th edition, 1993.

[30] W.D. Callister Jr. *Materials Science And Engineering: An Introduction*, volume 1. John Wiley & Sons, Inc., New York, 6th edition, 2003.

[31] A. Guinier. Structure of age-hardened aluminium-copper alloys. *Nature*, 142:569, 1938.

[32] G.P. Preston. Structure of age-hardened aluminium-copper alloys. *Nature*, 142:570, 1938.

[33] J.C. Fisher, E.W. Hart, and R.H. Pry. The hardening of metal crystals by precipitate particles. *Acta Metallurgica*, 1(3):336–339, 1953.

[34] H.O. Pierson. *Chemical Vapor Deposition of Semiconductor Materials, Surface Engineering*, volume 5, pages 510–516. ASM International, 1994.

[35] C. Wirz, A. Blatter, and R. Hauert. Properties of films prepared by thermal coevaporation of Cr and Ti in nitrogen. *Thin Solid Films*, 214(1):63–67, 1992.

[36] M. Sasaki, I. Nakamura, I. Takano, and Y. Sawada. Vacuum pressure dependence of the tribological properties of Ti, TiO2, and TiN thin films. *Electrical Engineering in Japan*, 149(3):1–7, 2004.

[37] Q.Q. Yang, W.H. Xiong, and H. Zhang. Study on strengthening mechanism of Au990-Ti jewelry alloys. *Rare Metal Materials and Engineering*, 35(12):1904–1907, 2006.

[38] J. Fischer. Mechanical, thermal, and chemical analyses of the binary system Au-Ti in the development of a dental alloy. *Journal of Biomedical Materials Research*, 52(4):678–686, 2000.

[39] R.A. Coutu, P.E. Kladitis, K.D. Leedy, and R.L. Crane. Selecting metal alloy electric contact materials for MEMS switches. *Journal of Micromechanics and Microengineering*, 14(8):1157–1164, 2004.

[40] S.K. Wu and C.M. Wayman. Martensitic transformations and the shape memory effect in Ti50Ni10Au40 and Ti50Au50 alloys. *Metallography*, 20(3):359–376, 1987.

[41] T. Kawamura, R. Tachi, T. Inamura, H. Hosoda, K. Wakashima, K. Hamada, and S. Miyazaki. Effects of ternary additions on martensitic transformation of TiAu. *Materials Science and Engineering A-Structural Materials Properties Microstructure and Processing*, 438:383–386, 2006.

[42] Pietrokowsky. The partial constitutional diagram $TiAu_2$-Au: lattice parameters of the Alpha solid solutions and the intermediate phase $TiAu_4$. *Journal of the Institute of Metals*, 90(11):434–438, 1961-62.

[43] P. Pietrokowsky, A. Frink, and P. Duwez. Investigation of partial constitution diagram Ti-$TiAu_2$. *Journal of Metals*, 206(8):930–935, 1956.

[44] H.C. Donkersloot and J.H.N. Van Vucht. Martensitic transformations in gold-titanium, palladium-titanium and platinum-titanium alloys near the equiatomic composition. *Journal of the Less Common Metals*, 20(2):83–91, 1970.

[45] W. Luo, Z. Jin, H. Liu, and T. Wang. Thermodynamic assessment of the Au-Ti system. *Calphad*, 25(1):19–26, 2001.

[46] R. Kurt, S. Dabritz, W. Hauffe, D. Bergner, and K. Richter. Characterization of multiphase diffusion zones by means of lattice source interferences. *Defect and Diffusion Forum*, 143:609–614, 1997.

[47] D.P. Van Heerden, M.P. Shaw, and D. Shechtman. The evolution of structural order in rapidly solidified Au-Ti alloys. *Philosophical Magazine B-Physics of Condensed Matter Statistical Mechanics Electronic Optical and Magnetic Properties*, 66(3):361–378, 1992.

[48] H. Yahagi, K. Yano, H. Itoga, A. Chaki, T. Ukai, and N. Mori. On the magnetism of Au_4Ti, Au_4V, Au_4Cr, Au_4Mn, Au_8TiCr, AND Au_8VMn. *Journal of Applied Physics*, 69(8):4651–4653, 1991.

[49] C.Y. Kim, S.W. Kim, C.H. Hong, D.W. Kim, H.K. Baik, and C.N. Whang. Effects of titanium silicide on AuSiTi/n-GaN ohmic contact systems. *Journal of Crystal Growth*, 190:720–724, 1998.

[50] M. Takahashi, M. Kikuchi, Y. Takada, O. Okuno, and T. Okabe. Corrosion behavior and microstructures of experimental Ti-Au alloys. *Dental Materials Journal*, 23(2):109–116, 2004.

[51] J.M. Poate, P.A. Turner, W.J. Debonte, and J. Yahalom. Thin-film interdiffusion .1. Au-Pd, Pd-Au, Ti-Pd, Ti-Au, Ti-Au, Ti-Pd-Au, and Ti-Au-Pd. *Journal of Applied Physics*, 46(10):4275–4283, 1975.

[52] O. Taguchi, T. Watanobe, Y. Yamazaki, and Y. Iijima. Reaction diffusion in the Au-Ti system between 1110K and 1150K. *Diffusions in Materials: Dimat2000, Pts 1 & 2*, 194-1:1569–1574, 2001.

[53] K. Richter, K. Keiter, D. Bergner, A. Muller, C.J. Raub, and D. Ott. Applicability of a Au(50 at%) Ti(50 at%)-alloy for diffusion measurements in the Au-Ti system. *Mikrochimica Acta*, 125(1-4):115–120, 1997.

[54] K. Masahiro and S. Noboru. Effects of temperature, thickness, and atmosphere on mixing in Au-Ti bilayer thin films. *Journal of Materials Science*, 28(18):5088–5091, 1993.

[55] R. Caron and J. Staley. *ASM Handbooks Online*, chapter Effects of Composition, Processing, and Structure on Properties of Nonferrous Alloys. ASM International, May 2002.

[56] *ASM Handbook Online*. ASM International, 2006.

[57] M. Graham. Precipitation hardening in gold-titanium alloys. In *31st Annual Electron Microscopy Society of America Meeting*, Annual EMSA Meeting, pages 148–149, 1972.

[58] H.I. Kim, H.J. Seol, D.H. Bae, J.Y. Shim, Y. Takada, and O. Okuno. Isothermal age-hardening behaviour in a Au-1.6 wt% Ti alloy. *Dent Mater J*, 18(1):32–41, 1999.

[59] D. Heger, K. Jenkner, P. Klimanek, D. Bergner, and C.J. Raub. The behavior of oxidation and precipitation hardening of very gold rich gold-titanium alloys. *Materialwissenschaft und Werkstofftechnik*, 26(9):507–518, 1995.

[60] D.P. Van Heerden, T. Aboud, D. Shechtman, and M.P. Shaw. Precipitation in rapidly solidified Au-Ti alloys. *Materials Letters*, 10(9-10):425–430, 1991.

[61] M. Kikuchi, M. Takahashi, and O. Okuno. Elastic moduli of cast Ti-Au, Ti-Ag, and Ti-Cu alloys. *Dental Materials*, 22(7):641–646, 2006.

[62] B. Rodmacq, V. Pelosin, J. Hillairet, and A. Chamberod. Elastic properties and structural evolution of AuTi superlattices. *Materials Science and Engineering A-Structural Materials Properties Microstructure and Processing*, 147(1):93–100, 1991.

[63] A.C. Fischer-Cripps. Critical review of analysis and interpretation of nanoindentation test data. *Surface and Coatings Technology*, 200(14-15):4153–4165, 2006.

[64] W.C. Oliver and G.M. Pharr. An improved technique for determining hardness and elastic-modulus using load and displacement sensing indentation expeirments. *Journal of Materials Research*, 7(6):1564–1583, 1992.

[65] S.I. Bulychev, V.P. Alekhin, M.K. Shorshorov, A.P. Ternovskii, and G.D. Shnyrev. Determination of youngs modulus according to indentation diagram. *Zavodskaya Laboratoriya*, 41(9):1137–1140, 1975.

[66] M.J. Mayo, R.W. Siegel, A. Narayanasamy, and W.D. Nix. Mechanical-properties of nanophase TiO_2 as determined by nanoindentation. *Journal of Materials Research*, 5(5):1073–1082, 1990.

[67] J. Mencik, D. Munz, E. Quandt, E.R. Weppelmann, and M.V. Swain. Determination of elastic modulus of thin layers using nanoindentation. *Journal of Materials Research*, 12(9):2475–2484, 1997.

[68] H. J. Gao, C. H. Chiu, and J. Lee. Elastic contact versus indentation modeling of multilayered materials. *International Journal of Solids and Structures*, 29(20):2471–2492, 1992.

[69] M.F. Doerner and W.D. Nix. A method for interpreting the data from depth-sensing indentation instruments. *Journal of Materials Research*, 1(4):601–609, 1986.

[70] I.G Goryacheva. *Contact Mechanics in Tribology*. Springer - Verlag, 1998.

[71] D.S. Liu, M.K. Shih, and W.H. Huang. Measurement and analysis of contact resistance in wafer probe testing. *Microelectronics Reliability*, 47(7):1086–1094, 2007.

[72] J.W. Tringe, T.A. Uhlman, A.C. Oliver, and J.E. Houston. A single asperity study of Au/Au electrical contacts. *Journal of Applied Physics*, 95(4):2196–2196, 2004.

[73] Z. Chen and K. Sawa. The investigation of surface charecteristics and contact resistance of DC relay contacts. *IEEE Transactions On Components, Hybrids, And Manufacturing Technology*, 16(2):211–219, 1993.

[74] J. Song and D.J. Srolovitz. Adhesion effects in material transfer in mechanical contacts. *Acta Materialia*, 54(19):5305–5312, 2006.

[75] L. Kogut and K. Komvopoulos. Analysis of interfacial adhesion based on electrical contact resistance measurements. *Journal of Applied Physics*, 94(10):6386–6390, 2003.

[76] A. Lumbantobing, L. Kogut, and K. Komvopoulos. Electrical contact resistance as a diagnostic tool for MEMS contact interfaces. *Journal of Microelectromechanical Systems*, 13(6):977–987, 2004.

[77] G. Gregori and D.R. Clarke. The interrelation between adhesion, contact creep, and roughness on the life of gold contacts in radio-frequency microswitches. *Journal of Applied Physics*, 100(9), 2006.

[78] J.A. Greenwood. Constriction resistance and real area of contact. *British Journal of Applied Physics*, 17(12):1621, 1966.

[79] R.G. Bayer. *Wear Behavior*, volume 20. ASM materials information, 2002.

[80] R.B. Waterhouse. Fretting wear. *Wear*, 100(1-3):107–118, 1984.

[81] M. Kutz. *Mechanical Engineers' Handbook - Materials and Mechanical Design*, volume 1. John Wiley & Sons, 3rd edition, 2006.

[82] K. Chopra. *Thin Film Phenomena*. New York, McGraw-Hill, 1969.

[83] J.R. McCormick, J.R. Kitchin, M.A. Barteau, and J.G. Chen. A four-point probe correlation of oxygen sensitivity to changes in surface resistivity of TiO_2 (001) and Pd-modified TiO_2 (001). *Surface Science*, 545(1-2):L741–L746, 2003.

[84] Keithley Instrument Inc. *Precision DC Current, Voltage and Resistance Measurements*. Low Level Measurements Handbook. Keithley, 1993.

[85] R.F. Wolffenbuttel. Low-temperature intermediate Au-Si wafer bonding; eutectic or silicide bond. *Sensors and Actuators A-Physical*, 62(1-3):680–686, 1997.

[86] R.D. Ott, C. Ruby, F. Huang, M.L. Weaver, and J.A. Barnard. Nanotribology and surface chemistry of reactively sputtered Ti-B-N hard coatings. *Thin Solid Films*, 377:602–606, 2000.

[87] S.A.E. Johansson, K.G. Malmqvist, and J.L. Campbell. *Particle Induced X-ray Emission spectrometry PIXE*. Wiley, 1995.

[88] C.R. Brundle, C.A. Jr. Evans, and S. Wilson. Encyclopedia of materials characterization - surfaces, interfaces, thin films, Aug 5 1992.

[89] R.G. Handschin and W.B. Stern. X-ray diffraction studies on the lattice perfection of human bone apatite (Crista Iliaca). *Bone*, 16(4, Supplement 1):S355–S363, 1995.

[90] T. Harriman. *Effect of Lanthanoid Ion Implantation on the Photoluminescence Response of Nanocrystals*. —mboxM.S. thesis, Oklahoma State University, 2008.

[91] H. Topsoe. *Geometric Factors in Four Point Resistivity Measurement*. 2nd edition, 1968. [Online:http://www.four-point-probes.com/haldor.html; accessed 25-May-2008].

[92] D.C. Miller, M.J. Talmage, and K. Gall. Incipient yielding behavior during indentation for gold thin films before and after annealing. *Journal of Materials Research*, 21(10):2480–2492, 2006.

[93] S. PalDey and S.C. Deevi. Single layer and multilayer wear resistant coatings of (Ti,Al)N: a review. *Materials Science and Engineering A-Structural Materials Properties Microstructure and Processing*, 342(1-2):58–79, 2003.

[94] B. Bhushan, B.K. Gupta, and M.H. Azarian. Nanoindentation, microscratch, friction and wear studies of coatings for contact recording applications. *Wear*, 181-183(Part 2):743–758, 1995.

[95] S.M. Han, R. Shah, R. Banerjee, G.B. Viswanathan, B.M. Clemens, and W.D. Nix. Combinatorial studies of mechanical properties of Ti-Al thin films using nanoindentation. *Acta Materialia*, 53(7):2059–2067, 2005.

[96] W.S. Lee and T.Y. Liu. The effect of annealing temperature on the microstructure of nanoindented Au/Cr/Si thin films. *Nanotechnology*, 18(33), 2007.

[97] W. Tang, K. Xu, P. Wang, and X. Li. Surface roughness and resistivity of Au film on Si-(111) substrate. *Microelectronic Engineering*, 66(1-4):445–450, 2003.

[98] K.L. Zhang, S.K. Chou, and S.S. Ang. Fabrication, modeling and testing of a thin film Au/Ti microheater. *International Journal of Thermal Sciences*, 46(6):580–588, 2007.

[99] M.F. Guerra, T. Calligaro, M. Radtke, I. Reiche, and H. Riesemeier. Fingerprinting ancient gold by measuring Pt with spatially resolved high energy Sy-XRF. *Nuclear Instruments & Methods in Physics Research Section B-Beam Interactions with Materials and Atoms*, 240(1-2):505–511, 2005.

[100] J.M. Zhang, K.W. Xu, and Vincent Ji. Dependence of stresses on grain orientations in thin polycrystalline films on substrates: an explanation of the relationship between preferred orientations and stresses. *Applied Surface Science*, 180(1-2):1–5, 2001.

[101] D.M. Hwang, S.A. Schwarz, T.S. Ravi, R. Bhat, and C.Y. Chen. Strained-layer relaxation in FCC structures via the generation of partial dislocations. *Physical Review Letters*, 66(6):739–742, 1991.

[102] J.W. Matthews and A.E. Blakeslee. Defects in epitaxial multilayers .1. misfit dislocations. *Journal of Crystal Growth*, 27:118–125, 1974.

[103] H. Gao, L. Zhang, W.D. Nix, C.V. Thompson, and E. Arzt. Crack-like grain-boundary diffusion wedges in thin metal films. *Acta Materialia*, 47(10):2865–2878, 1999.

[104] K. Mizuno, P. Mock, B.K. Tanner, G. Lacey, C.R. Whitehouse, G.W. Smith, and A.M. Keir. Partial strain relaxation in (In,Ga)as epilayers on GaAs by means of twin formation. *Journal of Crystal Growth*, 199:1146–1150, 1999.

[105] M. Ito, M. Kikuchi, O. Okuno, and K. Kimura. Ceramic bonding strength of Au-1.6 wt%Ti alloy. *Dental Materials Journal*, 24(2):268–274, 2005.

[106] J.H. Chae, J.Y. Lee, and S.W. Kang. Measurement of thermal expansion coefficient of poly-Si using microgauge sensors. *Sensors and Actuators A-Physical*, 75(3):222–229, 1999.

[107] T. Ye, Z. Suo, and A.G. Evans. Thin film cracking and the roles of substrate and interface. *International Journal of Solids and Structures*, 29(21):2639–2648, 1992.

[108] K. Chu, P.W. Shum, and Y.G. Shen. Substrate bias effects on mechanical and tribological properties of substitutional solid solution (Ti, Al)N films prepared by reactive magnetron sputtering. *Materials Science and Engineering B-Solid State Materials for Advanced Technology*, 131(1-3):62–71, 2006.

[109] T.C. Tisone and J. Drobek. Diffusion in thin-film Ti-Au, Ti-Pd, and Ti-Pt couples. *Journal of Vacuum Science & Technology*, 9(1):271–&, 1972.

[110] W.D. Nix and B.M. Clemens. Crystallite coalescence: A mechanism for intrinsic tensile stresses in thin films. *Journal of Materials Research*, 14(8):3467–3473, 1999.

[111] J.J. Burton and E.S. Machlin. Prediction of segregation to alloy surfaces from bulk phase-diagrams. *Physical Review Letters*, 37(21):1433–1436, 1976.

[112] G. Chen and P. Hui. Thermal conductivities of evaporated gold films on silicon and glass. *Applied Physics Letters*, 74(20):2942–2944, 1999.

[113] Y. Sugawara, N. Shibata, S. Hara, and Y. Ikuhara. Interface structure of face-centered-cubic-Ti thin film grown on 6H-SiC substrate. *Journal of Materials Research*, 15(10):2121–2124, 2000.

[114] D. Zhong, A.O. Kunrath, B. Mishra, K.H. Kim, A.A. Voevodin, E.A. Levashov, and J.J. Moore. Nanostructured Ti-B-C-N thin films produced from composite targets using unbalanced magnetron sputtering. In Society of Vacuum Coaters, editor, *SVC - 48th Annual Technical Conference Proceedings*, 2005.

[115] C. Suryanrayana and M.G. Norton. *X-Ray Diffraction A Practical Approach*, volume 1. Plenum Press, New York, 1998.

[116] S.S. Lau and R.C. Sun. Internal stresses and interdiffusion of Ti-Pd-Au films studied by x-ray diffraction techniques. *Thin Solid Films*, 10(2):273–282, 1972.

[117] S. Labdi, A. Jellad, and O. Maciejak. Loading rate effect on lateral force measurements on nanostructured Ti and TiN thin films. *Surface & Coatings Technology*, 201(1-2):113–119, 2006.

[118] H.S. Kim. On the rule of mixtures for the hardness of particle reinforced composites. *Materials Science and Engineering A-Structural Materials Properties Microstructure and Processing*, 289(1-2):30–33, 2000.

[119] Y. Matsuki, T. Inamura, K. Wakashima, and H. Hosoda. Effects of aging on phase constitution, lattice parameter and mechanical properties of Ti-4 mol%Au near-eutectoid alloy. *Materials Transactions*, 48(3):385–389, 2007.

[120] N.F. Mott and F.R.N. Nabarro. An attempt to estimate the degree of precipitation hardening, with a simple model. *Proceedings of the Physical Society*, 52:86–89, 1940.

[121] D. Tabor. *The Hardness of Materials*. Claredon Press, Oxford, UK, 1951.

[122] R.J. White. Weak resistance minimum in AuTi. *Journal of Physics F-Metal Physics*, 2(3):503–&, 1972.

[123] H.D. Hahlbohm. Elektrisches, magnetisches und galvanomagnetisches verhalten von kuffer-titan und gold-titan-mischkristallen. *Zeitschrift fur Metallkunde*, 54(9):515–518, 1963.

[124] J.H. Mooij. Electrical conduction in concentrated disordered transition metal alloys. *Physica Status Solidi (a)*, 17(2):521–530, 1973.

[125] H. Savaloni, K. Khojier, and M.S. Alaee. Characteristics of nanostructure and electrical properties of Ti thin films as a function of substrate temperature and film thickness. *Journal of Materials Science*, 42(8):2603–2611, 2007.

[126] G.W.B. Ashwell and R. Heckingbottom. Inter-diffusion of titanium and gold - A comparison of thin films deposited in technical vacuum and ultrahigh-vacuum. *Journal of the Electrochemical Society*, 128(3):649–654, 1981.

[127] L.M. Gammon, R.D. Briggs, J.M. Packard, K.W. Batson, R. Boyer, and C.W. Domby. *ASM Handbooks Online*, volume 9, chapter Metallography and Microstructures of Titanium and Its Alloys, pages 899–917. ASM International, 2004.

[128] T. Shimizuiwayama, K. Fujita, S. Nakao, K. Saitoh, T. Fujita, and N. Itoh. Visible photoluminescence in Si+-implanted silica glass. *Journal of Applied Physics*, 75(12):7779–7783, 1994.

[129] I. DeWolf. Micro-raman spectroscopy to study local mechanical stress in silicon integrated circuits. *Semiconductor Science and Technology*, 11(2):139–154, 1996.

[130] B. Dvorak. *Investigation of the Near Surface Mechanical Properties of Au-Si Thin Films*. M.S. thesis, Oklahoma State University, 2008.

[131] D. Hyman and M. Mehregany. Contact physics of gold microcontacts for MEMS switches. *Transactions on Components and Packaging Technology*, 22(3):357–364, 1999.

[132] G. Norberg, S. Dejanovic, and H. Hesselbom. Contact resistance of thin metal film contacts. *Components and Packaging Technologies, IEEE Transactions*, 29(2):371–378, 2006.

[133] J.E. Elder, R. Thamburaj, and P.C. Patnaik. Optimizing ion-implantation conditions for improving wear, fatigue, and fretting fatigue of Ti-6Al-4V. *International Materials Reviews*, 33(6):289–313, 1988.

[134] A. Bloyce, P.H. Morton, and T. Bell. Surface engineering of titanium and titanium alloys, 2002.

[135] ISO 14577-4: Test method for metallic and non-metallic coatings. International Organization for Standardization. Technical report, 2004.

[136] D.S. Stone and K.B. Yoder. Division of the hardness of molybdenum into rate-dependent and rate-independent components. *Journal of Materials Research*, 9(10):2524–2533, 1994.

[137] J.A. Shields Jr. and J.M. Dahl. *Molybdenum and Tungsten Annealing Practice*, volume 4. ASM International, 2007.

Appendix A

The Modification of Au Films by Mo Deposition

The preliminary results on Mo/Au and pure Au films are shown in the present Appendix.

A.1 Surface Topography

A 20 nm layer of Mo was deposited onto a 700 nm thick Au film by electron beam evaporation. The surface topography was measured using AFM and an optical image of the surface was also obtained which showed asperities and craters on the surface. These were found to be the result of a problem with the e-beam evaporation.

An ultrasonic bath (28X, NEY ULTRAsonik cleaner) with a nominal power of 145 W was employed to remove the possible contamination embedded in the Mo surface. The specimen was fully immersed in deionized water for about 2 min. Figure A.1(c) and (d) show the optical images of the surface before and after ultrasonic cleaning. No significant change in surface topography was observed after ultrasonic cleaning.

SEM analysis of the Mo/Au film was performed and Energy Dispersive Spectroscopy (EDS) was used in an attempt to understand the formation of the asperities and craters on the surface. Figure A.2(a) shows the SEM image of the Mo/Au surface and an EDS map over a 74 μm $\times$ 74 μm area. The EDS spectrum shown in Figure A.2(c) indicated the existence of Au, Mo and Ti on the surface. An unknown peak at about 1.7 keV approximately matched Kr, however, Kr was not used during the electron beam deposition. Au was detected over the entire surface of the scanned area, as shown in the Figure A.2(b)(1). Figure A.2(b)(2), mapped the existence of Mo on the same area. Dark

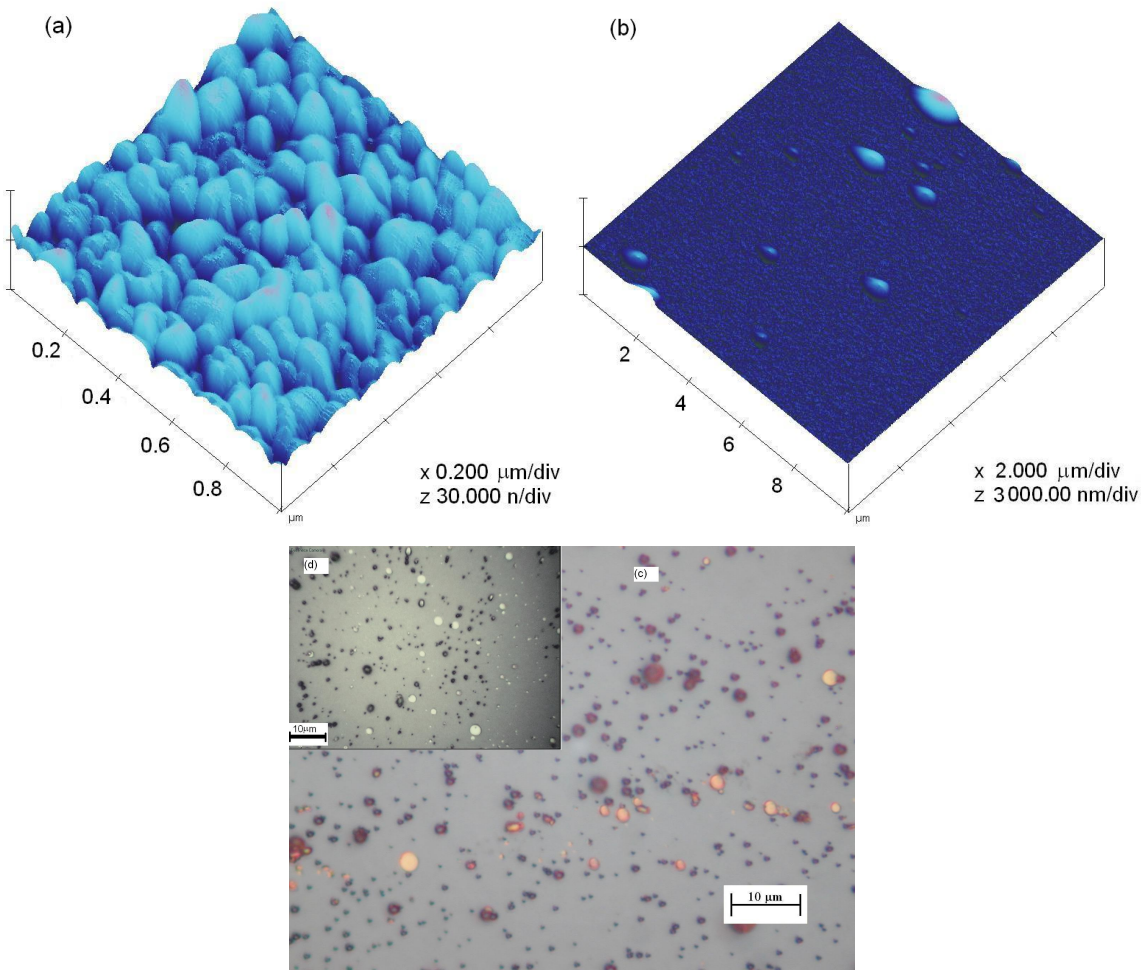

Figure A.1: AFM images of the Mo/Au film over (a) a 1 μm^2 and (b) a 100 μm^2 scan area. Optical images of the Mo/Au specimen (c) before and (d) after ultrasonic cleaning. The bright circles on the surface are craters and the darker, dull spots are the asperities on the surface.

circles on this image suggest the absence of Mo on the surface and correspond to the craters seen on the SEM image. Figure A.2(b)(3) is a combination of the previous images and the SEM image. A small shift in the combined image resulted from a short delay between the SEM measurement and the EDS surface map. The surface contamination was later found to have originated from a graphite crucible, used during the deposition procedure, and was corrected.

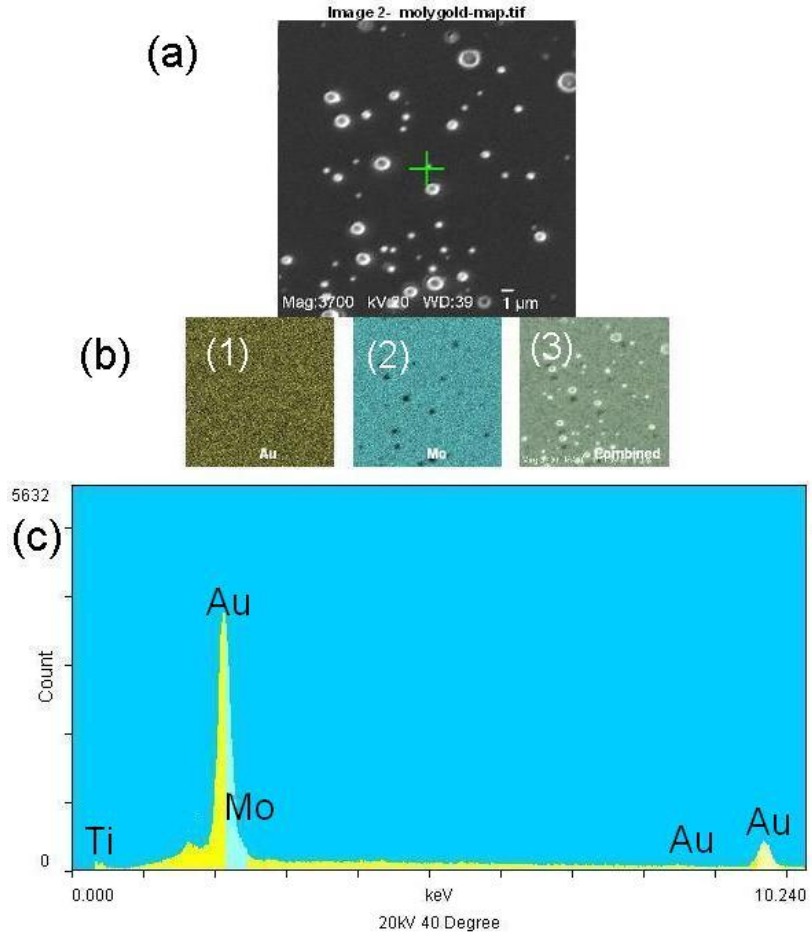

Figure A.2: (a) SEM image of the Mo/Au film. (b): (1) Au EDS map of the surface showing the presence of Au through the entire surface, (2) Mo EDS map of the surface. The dark spots indicate the absence of Mo in the craters on the surface; (3) combined Au and Mo EDS map projected on the SEM image. (c): EDS spectrum showing the Mo and Au regions (9.7 keV) chosen for the EDS mapping.

A.2 Mechanical Properties

The hardness and reduced elastic modulus were obtained using nanoindentation and the results are shown in Figures A.3 and A.4. Hardness increased by 92 % from about 1.2 GPa for the pure Au film to about 2.3 GPa for Mo/Au specimen as shown in Figure A.3. The data was extrapolated according to standards ISO 14577-4 given for very thin films [135]. The hardness of the pure Au film is consistent with the results obtained by Cao et. al. who found hardnesses of about 1 - 1.5 GPa for a 1 μm thick Au film for a contact depth of less than 40 nm [13]. The hardness of e-beam evaporated and steered arc evaporated Mo films (0.36 - 1.5 μm Mo on Si substrate) was found in

the literature to vary between 5 - 12 GPa [27, 28] and between 2 - 4 GPa for bulk Mo [136].

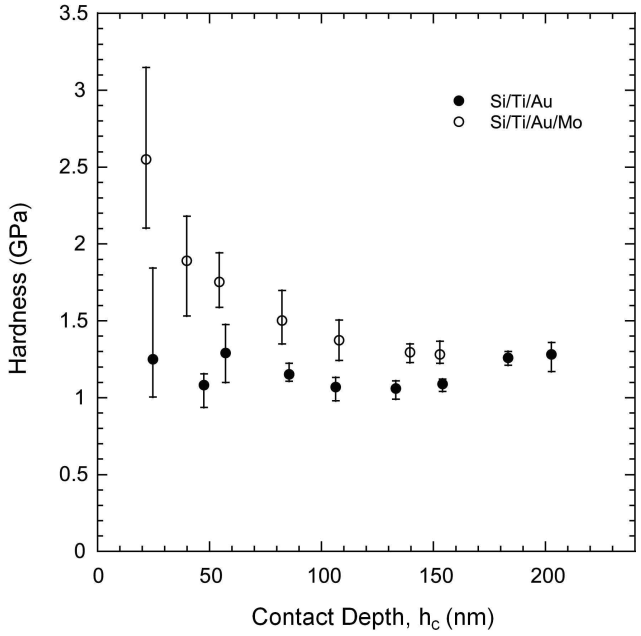

Figure A.3: Hardness of Mo/Au and pure Au (1 μm thick) films. The film hardness increased by about 92 % at the surface after deposition of Mo on pure Au film.

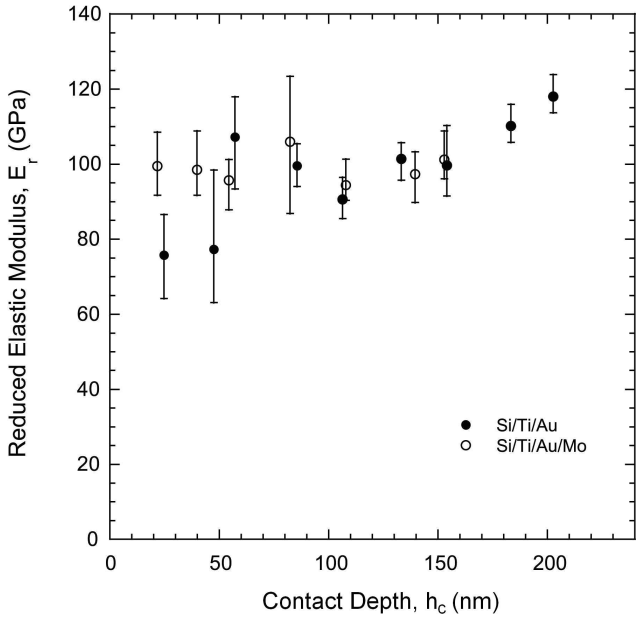

Figure A.4: Reduced elastic modulus of Mo/Au and pure Au (1 μm thick) films.

A.2.1 Tribological Performance: Microscratching

As shown in Figure A.5, it was found that as the applied load increased, the depth of scratches made on the surface also increased. However, an equal load applied to both films produced a deeper scratch on the Au contact surfaces in comparison to the Mo/Au, suggesting the improved effect of a thin Mo surface layer on the tribological performance of the Au film.

Figure A.6 shows the scratches made on Au and Mo/Au films by applying 200, 500, and 1000 μN maximum loads. The 200 μN load induced a scratch on the surface of the pure Au film and not the Mo/Au film.

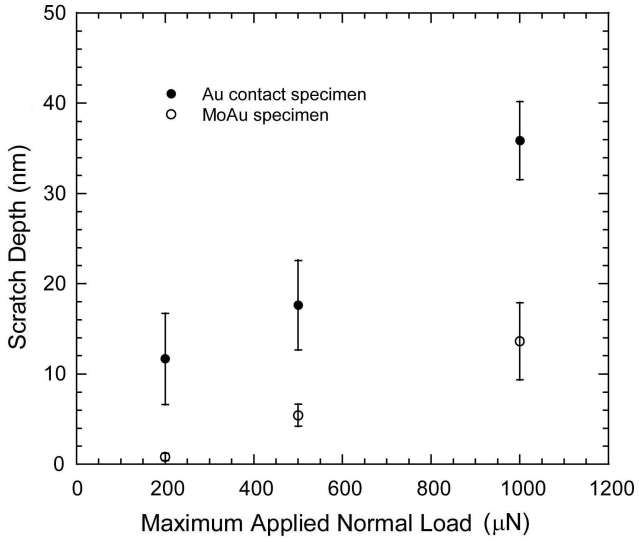

Figure A.5: The scratch depth versus the maximum applied normal load for Mo/Au and Au films. The error bars represent the standard deviation of two experiments performed at each load.

A.3 Tribological Measurements: Wear Experiments

The wear tracks created in the Mo/Au and Au films were similar. In both (Mo/Au and pure Au) films under a low load, small amounts of removed material was observed, while at higher loads, a pile up associated with plastic deformation was observed along the wear tracks. Additionally, an increase in normal displacement during the wear experiments was observed compared to a single scratch.

The coefficient of friction as a function of material properties was also investigated. While the

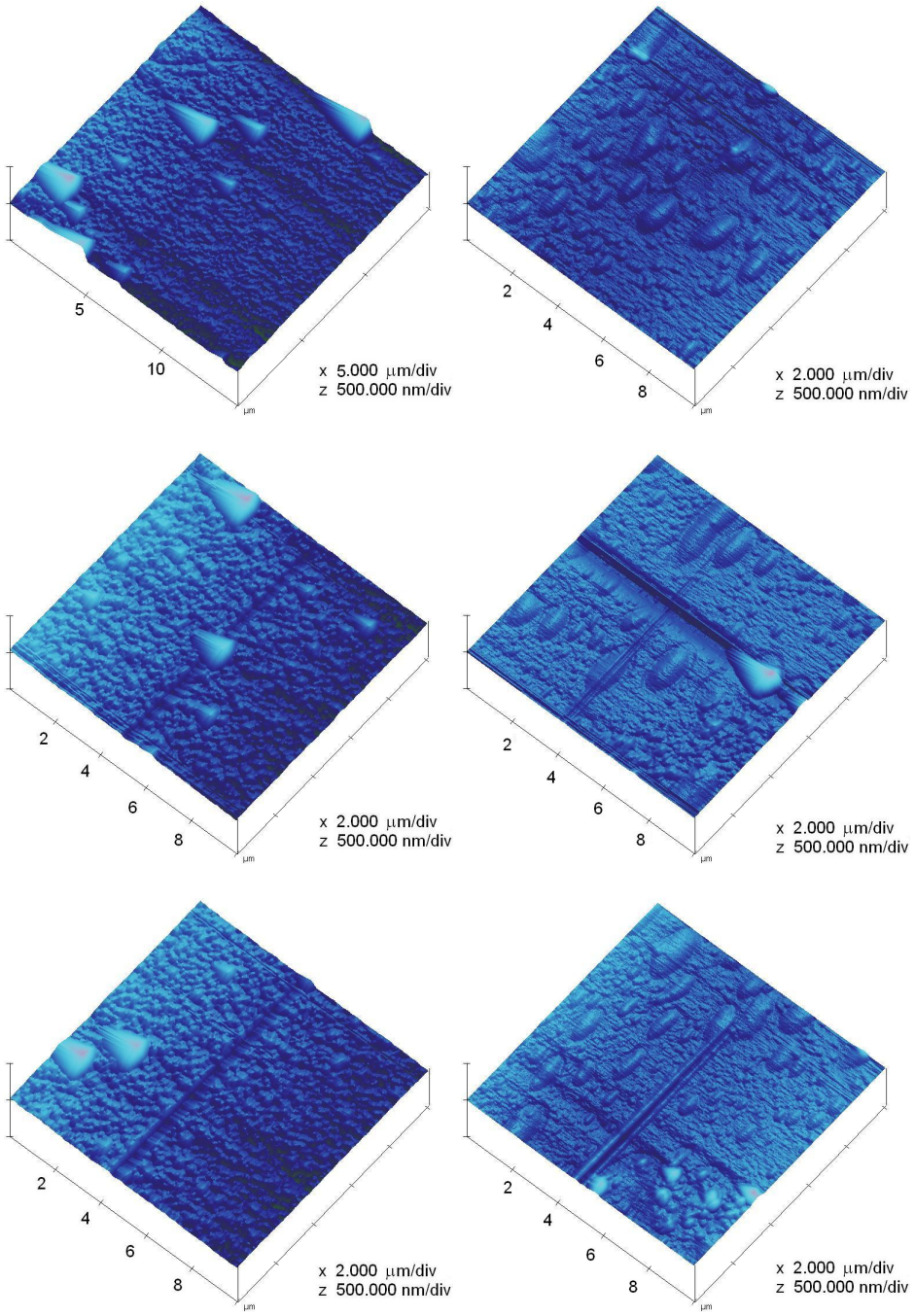

Figure A.6: AFM images of scratches made by (1) 200 μN, (2) 500 μN, (3) 1000 μN loads on (Left) Au and (Right) Mo/Au films. The direction of scratch is from the bottom left corner to the top right corner of each scan.

friction did not change significantly after increasing the load on the Mo/Au specimen from 200 μN to 1000 μN, it was found to increase for the Au specimen over the same load range (Figure A.7).

However, comparing the films under the same load conditions (500 μN), the Au specimen had a higher coefficient of friction compared to the Mo/Au specimen (Figure A.8).

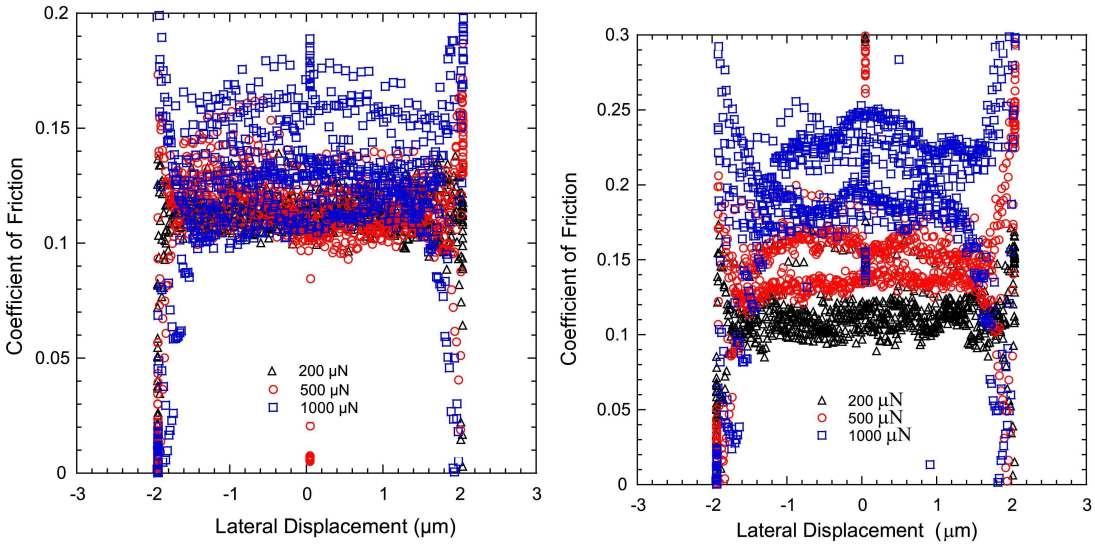

Figure A.7: Friction measurements obtained during the 4 μm scratch on (Left) Mo/Au and (Right) Au films using 200 μN, 500 μN, and 1000 μN loads.

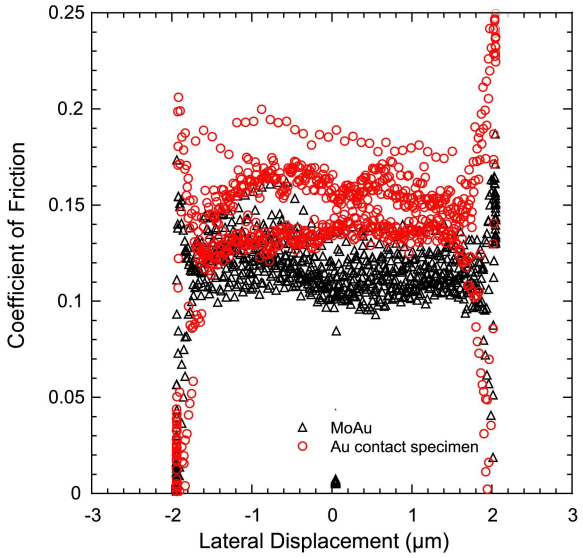

Figure A.8: Comparison of the coefficient of friction for Mo/Au and Au films applying a 500 μN load.

A.4 Limitations of Mo Modification

In an attempt to increase the tribological performance of Au electrical contacts, Mo was chosen as a thin surface layer. Being immiscible in Au the Mo layer could possibly prevent Au-Au bonding during cyclic operation of the contacts. However, Mo oxidizes at high temperatures (above 500°C), therefore, the deposition of Mo on Au for use in high power electrical contacts may be problematic since the oxidized layer could possibly reduce the contact resistance and conductivity of the contacts [137]. Furthermore, evaporation of the volatile Mo oxide makes it less desirable for operation at high temperatures. The evaporation of the volatile Mo oxide could lead to weight loss on the surface and subsequently generate surfaces with increased roughness [137]. In electrical contact applications, where the temperatures would not exceed 500° C, the Mo modified Au films could be a possible choice.

Appendix B

Images of Heat-Treated Au-Ti Films

In order to investigate the effect of precipitation or age hardening of Au-Ti alloy films, the Au-5.6 at. % Ti specimen was heat treated for various time periods. Figure B.1 displays the trend observed in the optical and AFM images of the first trial which was cooled on a room temperature Al piece to simulate quenching.

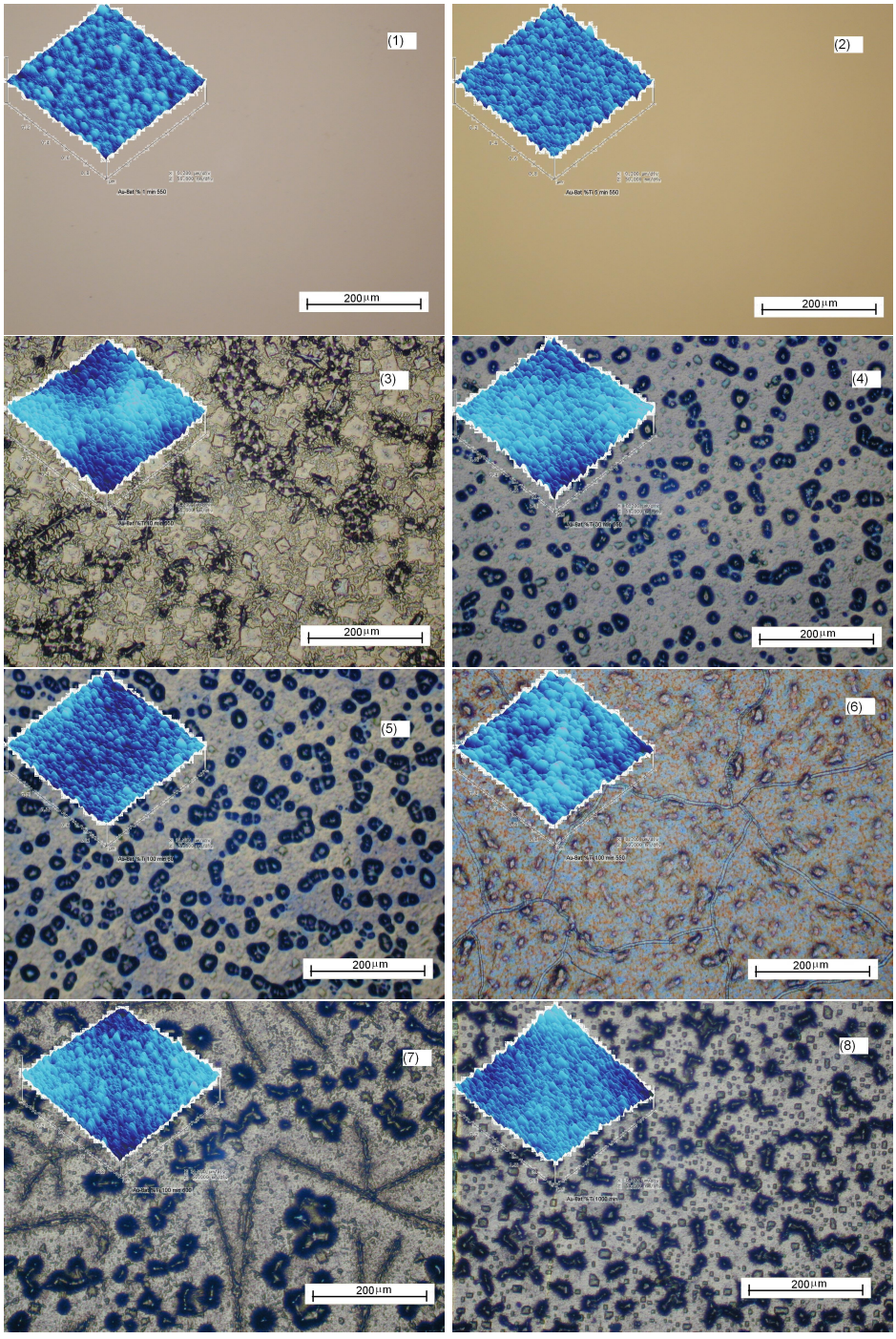

Figure B.1: First age hardening trial of the Au-5.6 at. % Ti specimen at 550°C after (1) 1 min. (2) 5 min. (3) 10 min. (4) 30 min. (5) 60 min. (6) 100 min. (7) 600 min. (8) 1000 min. heat treatment followed by quenching.

VITA

Golnaz Bassiri Jahromi

Candidate for the Degree of

Master of Science

Thesis: INVESTIGATION OF THE NEAR SURFACE MECHANICAL PROPERTIES OF Au-Ti THIN FILMS

Major Field: Mechanical Engineering

Biographical:

Personal Data: Born in Shiraz, Iran on July 25, 1983. A daughter of Mohammad Reza Bassiri Jahromi and Masoomeh Rana Mohammadi and sister to Sohrab Bassiri Jahromi. Received high school diploma in 2001.

Education:

Received the B.S. degree from Oklahoma State University, Tulsa, Oklahoma, U.S., 2005, in Mechanical Engineering.

Completed the requirements for the degree of Master of Science with a major in Mechanical Engineering, Oklahoma State University in July, 2008.

Experience:

Employed by Oklahoma State University, Department of Mechanical and Aerospace Engineering as a graduate research assistant and teaching assistant in Material Science; Oklahoma State University, 2006 to present. Employed by Oklahoma State University, Department of Mechanical and Aerospace Engineering as an undergraduate research assistant; OSU Tulsa, 2005.

Professional Memberships: American Society of Mechanical Engineering; American Physical Society; Honor Society of Phi Theta Kappa.

Name: Golnaz Bassiri Date of Degree: July, 2008

Institution: Oklahoma State University Location: Stillwater, Oklahoma

Title of Study: INVESTIGATION OF THE NEAR SURFACE MECHANICAL PROPERTIES OF Au-Ti THIN FILMS

Pages in Study: 82 Candidate for the Degree of Master of Science

Major Field: Mechanical Engineering

Gold is a common metal chosen for MEMS electrical contacts because of its high conductivity, ductility, inertness, and low resistivity, contact resistance and susceptibility to oxidation. However, due to the low hardness of gold, adhesion failure is prone in cycling conditions which reduces the reliability of the contacts.

Motivated by the goal to create high performance electrical contacts, a systematic study on the development of modified Au films was undertaken to examine how surface and subsurface material structure affects mechanical behavior. As a baseline study, the effect of deposition rate, adhesion sublayer, and heat treatment on e-beam evaporated Au films was investigated. The co-evaporation of Au and Ti was then undertaken, due to the prominent tribological performance of Ti alloys. Various amounts of Ti, ranging from 0.7 to 20 at. % Ti, were co-deposited with Au to investigate the changes in properties caused by the formation of a solid solution or intermetallic compound.

The increase in Ti content downsized the Au nodules on the surface of the films. In the Au-Ti films of 16 and above at. % Ti surface cracks were observed, indicative of increases in residual stresses. An increase in hardness was observed in the films with 16 and above at. % Ti. This increase in hardness is attributed to the formation of an intermetallic compound. Solid solution strengthening and grain refining did not affect the hardness of Au-Ti films of 0.7 - 5.6 at. % Ti. The resistivity of the Au-Ti films linearly increased by the addition of Ti. The heat treatment of Au-16.4 at. % Ti was performed to increase the diffusivity and recrystalize the intermetallic compound. The altered microstructure in the heat treated Au-16.4 at. % Ti film was accompanied by a shift from Au(111) to Au(200) consistent with a change from residual tensile to compressive stress reported in the literature. To investigate the precipitate hardening of Au_4Ti, the Au-5.6 at. % Ti films were heat treated for various times. An increase in hardness was measured suggesting the effect of precipitate hardening and dispersion hardening within the matrix.

ADVISOR'S APPROVAL: _____